Title	High-Pressure Synthesis, Crystal Structure and Physical Properties of Layered Manganese and Zinc Oxyhalides
Author(s)	蘇, 玉
Citation	北海道大学. 博士(理学) 甲第12917号
Issue Date	2017-09-25
DOI	10.14943/doctoral.k12917
Doc URL	http://hdl.handle.net/2115/67433
Type	theses (doctoral)
File Information	Yu_Su.pdf

High-Pressure Synthesis, Crystal Structure and Physical Properties of Layered Manganese and Zinc Oxyhalides

A Thesis

Submitted by

Yu SU

In fulfillment for the award of the degree of

Doctor of Science

Graduate School of Chemical Sciences and Engineering

Hokkaido University

2017

Abstract

Over the past few decades, mixed anion compounds have drawn great attention because incorporation of two or more different anions with specific electronegativity, polarizability, ionic radius, and oxidation state offers opportunity to effectively cause chemical and physical properties that the pure oxides cannot possess. Among many mixed anion systems, $A_2B(O, X)_4$, a subgroup of the A_2BO_4-based oxide perovskites with the K_2NiF_4-type structure possesses different anion sites (i.e. equatorial and apical sites), leading to anion-site order in the anion sublattices. This situation is much different from that in the regular perovskite structure $AB(O, X)_3$ which tends to disorder the anion sites. It is very important that accessibility to anion-site ordered states provides good advantage of understanding the role played by each anion in the structural, physical and chemical properties. Another aspect of anion lattice modification with hetero anions is that the electronic structures are changed in a way different from conventional cation substitution: anions are intimately bonded to cations, and thus anion substitution can effectively affect the coordination geometry or environment around the metal centers, which are closely correlated with the electronic structures of the compounds.

In this thesis, we used a high pressure technique to synthesize new complex transition metal oxyhalides with the K_2NiF_4-type structure and studied their crystal structures and properties.

Another member of layered oxyfluoride family, Sr_2MnO_3F was synthesized successfully with the high-pressure synthesis at 6 GPa and 1800 °C. It crystallizes into a simple body-centered tetragonal cell in the space group $I4/mmm$, with lattice parameters $a = 3.79009(1)$ Å and $c = 13.28974(6)$ Å. The manganese oxyfluoride exhibits unique structural features that have never been observed in any other related layered oxyhalides: the coexistence of anion disorder between O and F at the apical sites and the octahedral coordination subject to the 1st order Jahn-Teller effect. The MnO_2 planes separated by non-magnetic Sr(O/F) rock-salt layers

result in low-dimensional magnetic correlations with T_N = 133 K, which is totally different from paramagnetic behaviors observed in known related layered manganese oxyfluorides.

A new layered perovskite zinc oxychloride, $Sr_2ZnO_2Cl_2$, with an infinite ZnO_2 square planar sheet has been successfully synthesized by high pressure method. For Zn coordination environment, this square planar is quite unique and rare. $Sr_2ZnO_2Cl_2$ isostructural with $Sr_2CuO_2Cl_2$, a well-known parent material of high-T_c superconducting cuprates. The lattice constants of the zinc oxycloride are $a = 4.06981(2)$ Å and $c = 15.20076(8)$ Å at room teperature. The UV-vis-NIR absorption spectroscopy revealed an indirect band gap of $E_g = 3.66$ eV. The first principles calculation demonstrated that the origin of the indirect band gap was correlated with the square planar geometry for Zn: a transition between the top of the valence band comprising the anti-bonding state between Zn $3d_{x^2-y^2}$ and O $2p$ orbitals and the bottom of the conduction band derived from Zn $4s$ orbitals.

A possible ideal two-dimensional square-lattice antiferromagnet $Sr_2MnO_2Cl_2$ was successfully synthesized by high pressure method at 6 GPa and 1500 °C. It adopts a simple body-centered tetragonal cell in the space group $I4/mmm$. From the magnetic susceptibility measurement, the manganese ion was found to have a high spin state of $S = 5/2$. The susceptibility curve also showed a broad maximum at T_{max} = 42K, which is typical behavior of the low dimensional antiferromagnets. No anomaly associated with a long-range magnetic order was observed down to 2 K, which was consistent with the result of the heat capacity measurement with a broad curve centered at 40 K. Neutron powder diffraction study demonstrated that a short-range magnetic correlation developed below 100 K but not to a long-range magnetic order down to 2 K. This is the first experimental observation of no long-range magnetic ordered state in square lattice antiferromagnets.

Keywords:

Oxyhalide, High-pressure synthesis, Crystal structure, Magnetic property.

List of Abbreviations

MPMS	Magnetic property measurement system
PPMS	Physical property measurement system
XRD	X-ray diffraction
Spring-8	Super Photon ring-8 GeV
SXRD	Synchrotron X-ray diffraction
FC	Field cooling
ZFC	Zero field cooling
T_C	Curie temperature
T_N	Neel temperature
FIM	Ferrimagnetic
DOS	Density of states
AF	Antiferromagnetic
FM	Ferromagnetic
NN	Nearest neighbor
t	Tolerance factor
$\prod_c$	Coulombic energy
θ	Weiss temperature
C	Curie constant
μ_eff	Effective magnetic moment
μ_S	Spin only magnetic moment
$\mu_\mathrm{S+L}$	Magnetic moment from full spin and orbital motion
BVS	Bond valance sum
ΔS_m	magnetic entropy

C_p	Heat capacity
C_phonon	Heat capacity of lattice contribution
NIMS	National Institute for Materials Science
SO	Spin-orbit
E_F	Fermi energy
J	Exchange constant
λ	Spin-orbit coupling constant
2D	Two-dimensional
χ	Magnetic susceptibility
ANSTO	Australian Nuclear Science and Technology Organizations
HRPT	High-Resolution Powder Diffractometer for Thermal Neutrons
PSI	Paul Scherrer Institute
OPAL	Open Pool Australian Lightwater reactor
VBM	Valence band maximum
CBM	Conduction band minimum

High-Pressure Synthesis, Crystal Structure and Physical Properties of Layered Oxyhalides

Contents

Chapter 1 Introduction

1.1 Perovskite structure

Perovskite-related materials have attracted great attention since their discoveries. Because of the unique properties, such as ferroelectricity[1], colossal magnetoresistance (CMR)[2], superconductivity[3], they can be applied in many areas, such as electronic conductors, capacitors, superconducting cables, thermoelectric devices and battery materials[4-8]. The general formula of perovskites is ABO_3, in which A is a large electropositive cation(for example, Sr^{2+}, La^{3+}, K^{+}), B is a small transition metal or main group ion(Cu^{2+}, Fe^{3+}, Co^{2+}, etc.)[9]. The ideal structure of perovskite is cubic with space group of $Pm\bar{3}m$, as shown in **Figure 1.1**. It can be described as a frame of corner sharing BO_6 octahedra[10]. To form the ideal perovskite structure, the radii of A and B should satisfy equation $(r_A + r_O) = \sqrt{2}(r_B + r_O)$, where r_A, r_B and r_O are effective ionic radii. In fact, the ideal cubic perovskite structure only exists in minor matters, and in major cases the bond lengths of (A-O) and (B-O) are geometrically incompatible, resulting in structure distortions and lowering of structure symmetry[11]. The tolerance factor is defined to describe the distortion of the octahedra: $t = \dfrac{R_A + R_O}{\sqrt{2}(R_B + R_O)}$. When A ion is too big or B ion is too small, t becomes larger than 1, and as a result, the crystal structure is altered to hexagonal or tetragonal, $BaNiO_3$ is an example. When A and B ions have ideal size, t falls in the range of 0.9-1, thus the structure is cubic, just like the perovskite. When A ion is too small to be accommodated into B ion interstices, t is 0.71-0.9, several possible structures exist, i.e. orthorhombic or rhombohedral, such as the Orthorhombic $GdFeO_3$. When A and B ions have similar ionic radii, t will be smaller than 0.71, and possible close-packed structures exist, corundum structure (disordered arrangement of cations), ilmenite structure (ordered arrangement within sheets), $KNbO_3$ structure (sheetwise ordered arrangement).

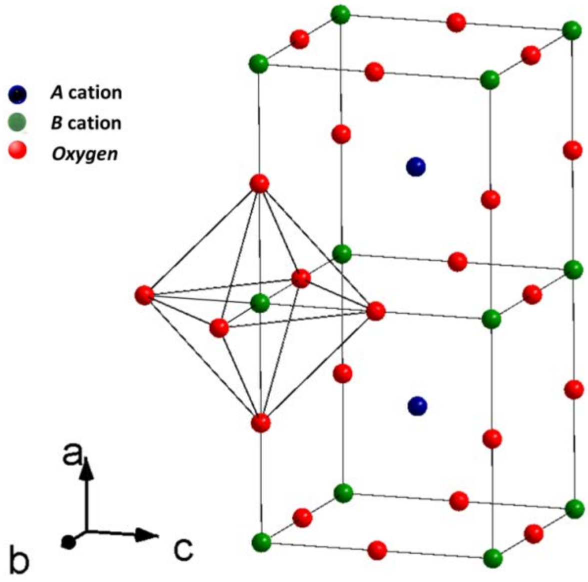

Figure 1.1 *AB*O_3 ideal perovskite structure[10].

1.2 Ruddlesden-Popper phases

In 1958, Ruddlesden and Popper reported the synthesis and characterization of the novel layered mixed metal oxide $Sr_3Ti_2O_7$[12]. The crystal structure of $Sr_3Ti_2O_7$ was determined to be the space group *I4/mmm* consisting of double perovskite layers of corner linked TiO_6 octahedra interwoven with layers of rock salt SrO. Ruddlesden and Popper also proposed the existence of related compounds and simultaneously reported the discovery of one such phase, $Sr_4Ti_3O_{10}$, which has a similar structure, but with tripple perovskite layers[13]. $Sr_3Ti_2O_7$ and $Sr_4Ti_3O_{10}$ represent two examples of a series of related layered perovskite intergrowth materials known as the Ruddlesden-Popper family, abbreviated as RP phase or RP structure. The general formula for $A_{n+1}B_nX_{3n+1}$ with n layers of BX_6 octahedra separated by layers of AX adopting the rock salt structure. The end member phase with $n = \infty$ has an infinite number of layers of BX_6 octahedra and corresponds to the simple perovskite structure ABX_3. The crystal structures are shown in **Figure 1.2**.

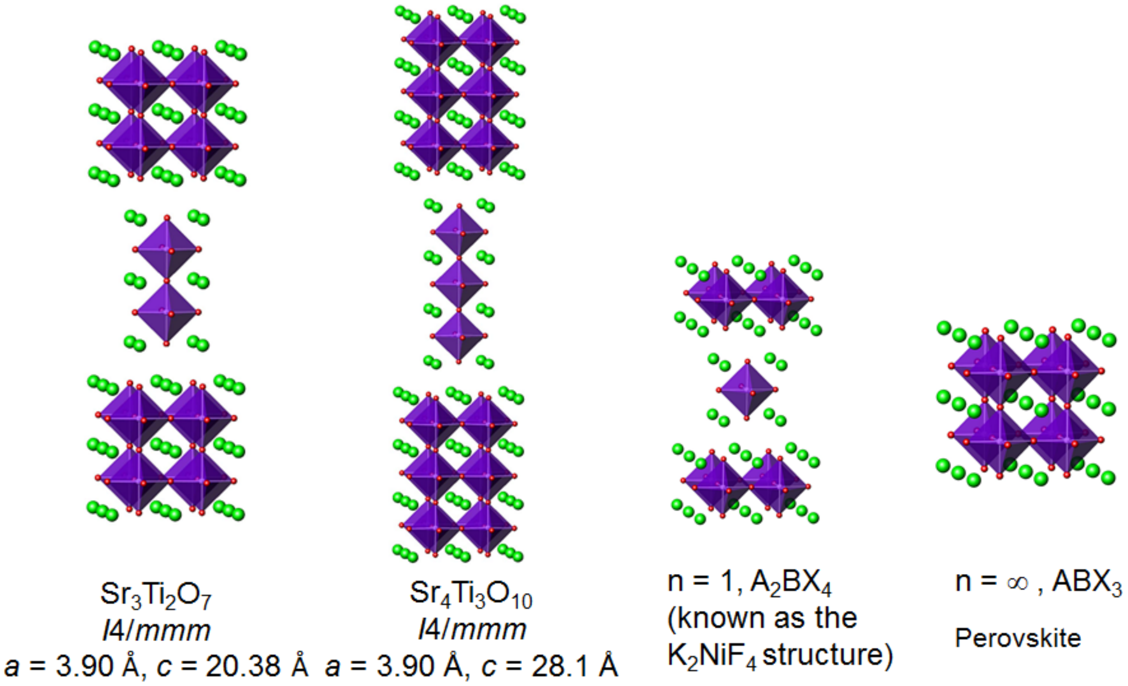

Figure 1.2 Crystal structure of $A_{n+1}B_nX_{3n+1}$ Ruddlesden-Popper phases

1.3 Physical Properties of RP Phase

RP type materials exhibit rich variety of intriguing properties. In recent years, the discovery of new properties has generated a wealth of research interest, and these areas will be discussed below.

1.3.1 Low Dimensional Magnetism

The research of low dimensional magnetism can be dated back to 1925, when the one-dimensional (1D) Ising model was first proposed[14]. Some decades of theoretical researches followed[14-16]. Onsager gave an exact solution of the 2D Ising model for the existing of long range order in 1949[17], while Mermin and Wagner stated the absence of long range order in 1D and 2D magnetic models with a continuous symmetry at any finite temperature in 1966, which is known as in their famous Mermin-Wagner theorem[18]. Around 1970, magnets in restricted dimensions started to be investigated experimentally when real bulk crystals were synthesized successfully with magnetic coupling much stronger in one or two spatial directions than in the remaining ones.

A_2BX_4 is among the typical objects of the 2D magnetism. The magnetic ions sit on a square lattice in two-dimensions. Because of the intervention of the rock salt layer, the interlayer interaction becomes very weak and can be neglected. K_2NiF_4 is the first well studied material and often these systems are said to have the K_2NiF_4 structure[19, 20]. The Mermin-Wagner theorem does not say anything about the $T = 0$ ground state. Coincidentally evidence shows that for 2D Heisenberg antiferromagnets, long range magnetic order does occur at $T = 0$. The K_2NiF_4 structure is of considerable interest because 2D Heisenberg models appear to be important in understanding the high-T_c cuprate superconductors which will be discussed in the following part.[21]

1.3.2 Superconductivity

Superconductivity was first discovered by Kamerlingh-Onnes during his study into the resistivity of solid mercury at low temperatures whereby a dramatic fall in the resistance appeared at just over 4.2K[22]. In subsequent decades, efforts were made to find other superconductive materials. In 1913, lead was found to be superconductive at 7 K, and in 1941 niobium nitride was found at 16 K[23, 24]. In 1953 vanadium-silicon displayed superconductive properties at 17.5 K[25]. Typical temperature dependence of the electrical resistivity and the magnetic susceptibility of a superconductor are shown in **Figure 1.3**. Exactly zero electrical resistance and expulsion of magnetic flux fields are the main characteristics of superconductors.

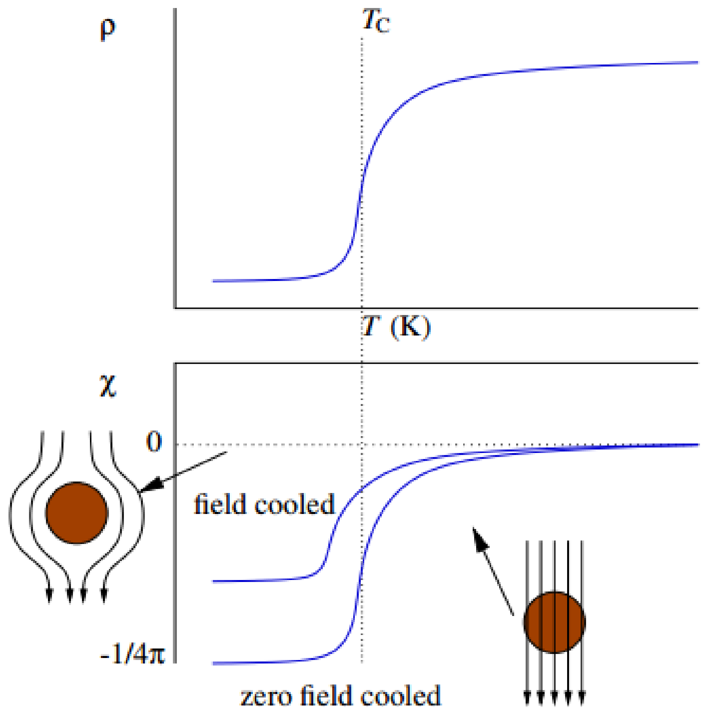

Figure 1.3 The physical properties of superconducors

The first widely-accepted theoretical understanding of superconductivity was advanced in 1957 by American physicists, John Bardeen, Leon Cooper, and John Schrieffer[26]. Their theories of superconductivity became known as the BCS theory and won them a Nobel prize in 1972. The basis of the theory was that the electrons with opposite spin and momentum can be combined into pairs to form "Cooper pair". Cooper pairs can move in the lattice without loss of energy thus forming the superconductive current. The BCS theory explained superconductivity at temperatures close to absolute zero for elements and simple alloys. However, at higher temperatures and with different superconductor systems, the BCS theory has subsequently become inadequate to fully explain how superconductivity is occurring.[27-29]

Cuprates tend to be high-T_c superconductors, especially within the K_2NiF_4 structure. For example, doping 20% La^{3+} with Sr^{2+} in La_2CuO_4 structure ends up with high temperature superconductivity at around 40 K, while the pure La_2CuO_4 is an antiferromagnetic insulator[30-

[32]. However, by replacing Cu^{2+}(S = 1/2) with Ni^{2+}(S = 1), these do not become superconducting even when doped[33]. One acceptable reason is that local magnetic fields due to magnetic ions act as pair-breakers, splitting up the Cooper pairs.

$Ca_2CuO_2Cl_2$, an analogue with La_2CuO_4 structure but with Cl substitution the apical sites of CuO4 octahedral, is another intensive studied superconductor. With hole doping by Na, superconductivity was found at Tc = 26 K in $(Ca,Na)_2CuO_2Cl_2$. Two functional blocks constitute the structure, i.e., the charge reservoir layer and CuO2 conducting layer[34, 35]. $Sr_2CuO_2F_{2+\delta}$, another analogue with La_2CuO_4 structure[36], also shows a superconductive transition at Tc 46 K. These results show that when the apical anions are replaced by halogen ion, the cuprates can give high T_c superconductivity.

1.4 Chemical Environments

1.4.1 Crystal Fields

The crystal field is an electric field derived from neighboring atoms in the crystal. The crystal field in perovskite related materials arises mainly from electrostatic repulsion from the negatively charged electrons in the oxygen orbitals[37].

When the *d* orbitals of a transition metal ion in a perovskite structure where the metal center is surrounded by six oxygen ions O^{2-}, the O^{2-} ligands give rise to the crystal field potential and affect the free diffusion of the electrons and quench the orbital angular momentum by splitting of the *d* orbitals because of the introducing of the crystal field[38]. *d* orbitals are split to two groups. The $d_{x^2-y^2}$ and d_{z^2} orbitals, which point to *p* orbitals of the surrounding oxygen ions, are raised in energy. The d_{zx}, d_{yz}, and d_{xy} orbitals, which point diagonally between the *p* orbitals, are relatively unaffected by the field. The former $d_{x^2-y^2}$ and d_{z^2} orbitals are called e_g orbitals, whereas the latter, d_{zx}, d_{yz}, and d_{xy} orbitals are called t_{2g} orbitals, as shown in **Figure 1.4**. The resulting energy difference is identified as Δo.

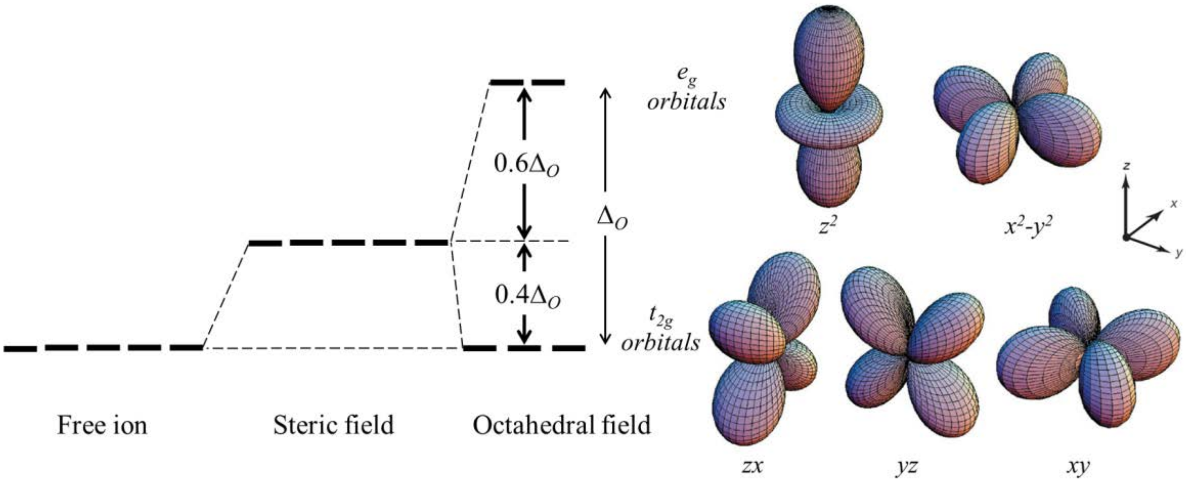

Figure 1.4 The *d* orbital splitting in octahedral field conditions[38].

For the given metal center, the energy difference changes with the ligands. When the ligands orbitals strongly interact with the metal orbitals, the splitting between the t_{2g} and e_g orbitals is large (Δo is large), and the corresponding ligands are called strong-field ligands[39]. Ligands with weak interactions with the metal orbitals are called weak-field ligands, and the split is small (Δ_O is small). The orbital configuration of the electron depends on the competition between the crystal field energy and the Coulombic energy ($\prod_c$) cost of putting two electrons in the same orbital, which is known as pairing energy[40-42]. For each of d^0 to d^3 and d^8 to d^{10} ions, only one configuration is possible, but for d^4 to d^7 ions, strong crystal fields lead to low-spin state and weak crystal fields lead to high-spin state, as in strong crystal field, electrons tend to firstly occupy each orbital before any orbital becomes doubly occupied, and vice versa. An example is shown in **Figure 1.5**[39, 43-45]**.**

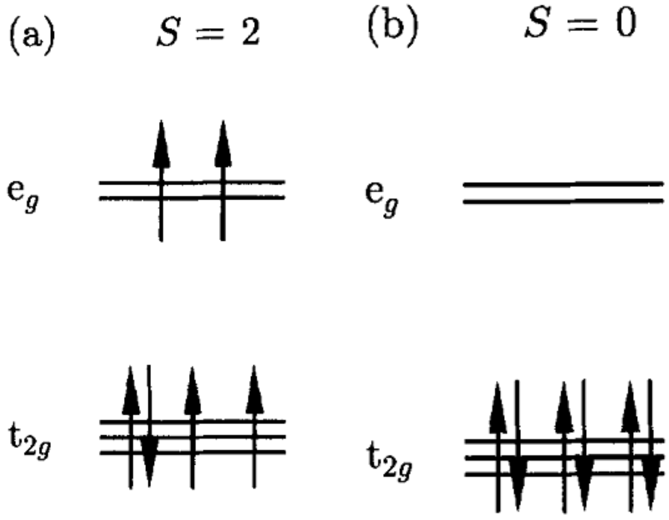

Figure 1.5 Electronic configuration for the **(a)** high-spin (weak-field) and **(b)** low-spin (strong-field) cases for a 3d^6 ion, e.g. Fe^{2+}.

1.4.2 The Jahn-Teller effect

The Jahn–Teller effect, sometimes also known as Jahn–Teller distortion, describes the geometrical distortion of molecules and ions that is associated with certain electron configurations[46]. The molecular distortion associated with symmetry-breaking would break the electronic degeneracy by the stabilization (lowering in energy) of the *d* orbitals with a *z* component, while the orbitals without a *z* component are destabilized (higher in energy), as shown in **Figure 1.6**. Examples of significant Jahn-Teller effects are found in complexes of Cr^{2+} (d^4), high-spin Mn^{3+} (d^4), and Cu^{2+} (d^9)[47-50]. For example, octahedral Cu^{2+}, a d^9 ion, would have three electrons in the two e_g levels without the Jahn-Teller effect. The Jahn-Teller effect elongates the CuO_6 octahedra along *z*-axis. The effect of elongation on *d* orbital energies is shown in the right of **Figure 1.6**[37]. The half filled $d_{x^2-y^2}$ orbital of Cu^{2+} carries a spin S=1/2 aligning within the *ab*-planes, which may result in two-dimensional antiferromagnetic behavior as shown in **Figure 1.6b**[51].

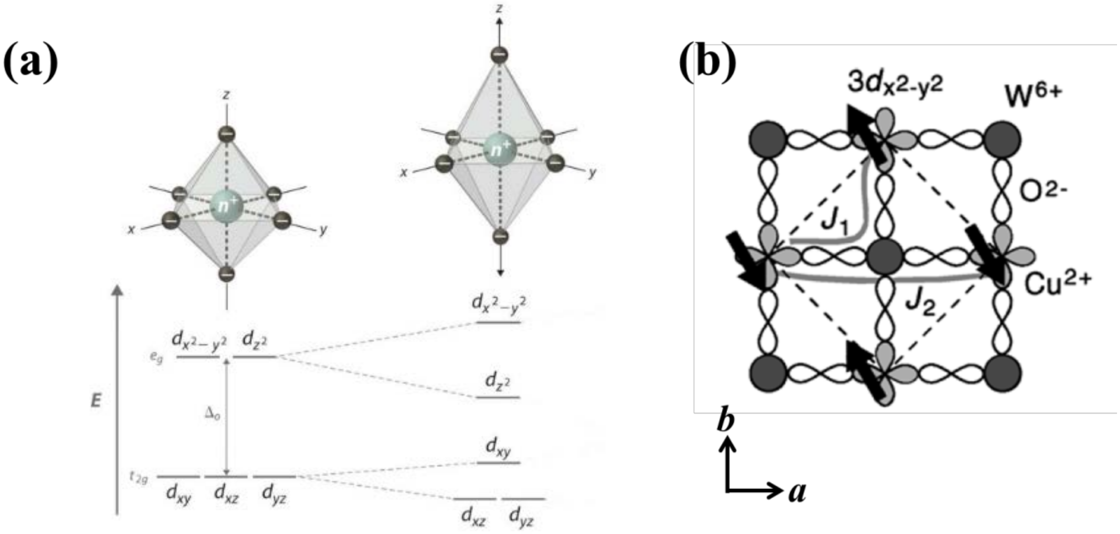

Figure 1.6(a) Diagram of electronic structures of Cu^{2+} with Jahn-Teller interaction[37]; **(b)** Magnetic structure of Ba_2CuWO_6[51].

1.5 Magnetism

1.5.1 Origin of magnetism

Magnetism is a property of matters that respond to an applied magnetic field. Magnetism originates from the electrons of atoms, especially unpaired electrons. Two aspects of electrons determine the magnetic properties collaboratively. Firstly, the spinning of electron on its axis produces a magnetic moment. Secondly, orbital motions of an electron will also produce a magnetic moment according to the pre-wave-mechanical picture of an atom. The magnetic properties of any individual atom or ion will result from some combinations of these two contributions, which are the inherent spin moments of the electrons and the orbital moments resulting from the motion of the electrons around the nucleus, respectively[52]. The magnetic moment generated from the orbital or spin motion of a single electron is called Bohr magnetron, μ_B , which is the smallest unit of magnetic moment of substance[53].

The magnetic moment due to the electron spins alone is $\mu_s = g\sqrt{S(S+1)}$ (unit is μ_B,), in which S is the sum of the spin quantum numbers and g is the gyromagnetic ratio, also known as the "g factor". For free electrons, g = 2.00023. The calculated magnetic moment μ_s due to spins of the electron alone is called "spin-only" moment. If the orbital motion were considered, and when it makes its full contribution to the magnetic moments, the magnetic moment will be given by $\mu_{S+L} = \sqrt{4S(S+1) + L(L+1)}$, in which L represents the angular momentum quantum number for the ion[44, 52]. In general, most of the 3*d* transition metal ions do possess orbital angular momentum. However from **Table 1.1** the observed values of μ_{eff} are close to or larger than μ_S, but much smaller than μ_{S+L}. It is because the crystal field surrounding the metal ions restricts the orbital movement of the electrons, therefore the orbital angular momentums are "*quenched*"[52] wholly or partially.

Table 1.1. Effective moments and spin-orbit coupling constant associated with first series transition-metal ions[54]

	Ti^{3+}	V^{3+}	Cr^{3+}	Mn^{3+}	Mn^{2+}, Fe^{3+}	Fe^{2+}	Co^{2+}	Ni^{2+}	Cu^{2+}
μ_S	1.73	2.83	3.87	4.0	5.92	4.90	3.87	2.83	1.73
μ_{eff} (exp.)	~1.80	~2.80	~3.80	~4.9	~5.90	~5.40	~4.80	~3.20	~1.90
μ_{S+L}	3.00	4.47	5.20	5.48	5.92	5.48	5.20	4.47	3.00
λ [cm^{-1}]	154	105	91	88	-	-	-	-	-

1.5.2 Types of magnetic behaviors

There are several types of magnetic states, as shown for a schematic 1D crystal in **Figure 1.7**. The unpaired electron spins may be oriented at random directions on the different atoms, in which case the material is paramagnetic (a), or they may interact with each other resulting in cooperative magnetic phenomena. The spins may be aligned parallel, in which case the material is ferromagnetic (b), or they may be aligned antiparallel, resulting in zero overall magnetic moment and the material has antiferromagnetic property (c). Another case for the antiparallel alignment is that they possess unequal numbers in the two orientations, thus there is a net magnetic moment and the behavior is called ferrimagnetic (d). Spin glass behavior occurs in certain cases where the dominating ordering tendency is antiferromagnetic but complete antiferromagnetic order is not able to propagate through the structure; instead, it is disrupted by ferromagnetic order (e). In helimagnetic behavior, spins are not limited to arrange in simple parallel or antiparallel way but show a gradual angular rotation between adjacent spins, leading to a helical magnetic structure (f)[55].

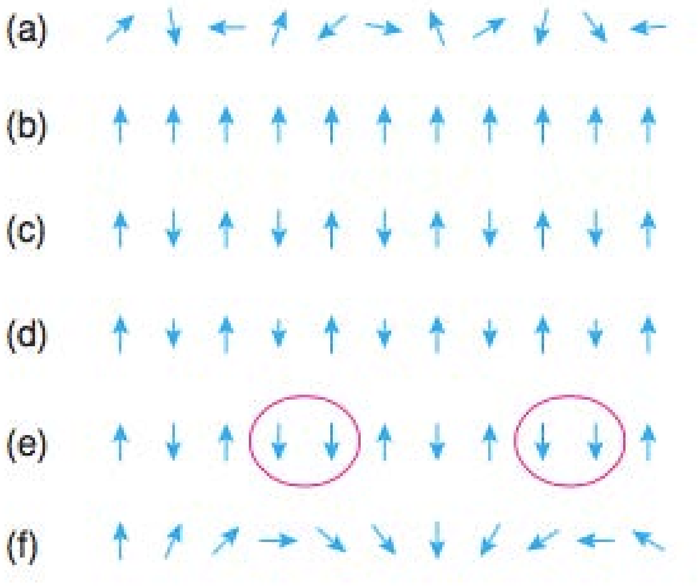

Figure 1.7 Schematic magnetic phenomena in a 1D crystal: (a) paramagnetism; (b) ferromagnetism; (c) anti- ferromagnetism; (d) ferrimagnetism, (e) spin glass behaviour; (f) helimagnetism[55].

Since most of the compounds in this thesis show an AFM transition, I would like to introduce the types of antiferromagnetic structures in the following part.

1.5.3 Types of antiferromagnetic structures

There are three types of antiferromagnetic ordering which is particular important in perovskite-related materials. They are illustrated in **Figure 1.8**. In A-type AFM structure, the intra-plane interaction is ferromagnetic but the inter-plane is antiferromagnetic. In C-type AFM structure, the case is inverse, the intra-plane coupling is antiferromagnetic while inter-plane coupling is ferromagnetic. Another type is the G-type AFM structure, in which both of the intra- and inter-plane coupling are antiferromagnetic. In addition, a more complicated CE-Type is possible, in which the spin and charge ordered antiferromagnetic phase[56].

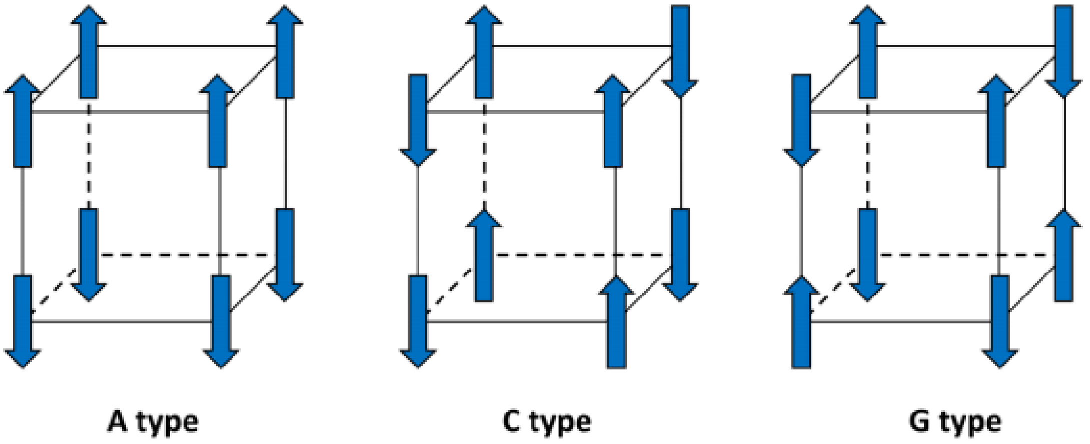

Figure 1.8 Three antiferromagnetic structure types in perovskite

1.5.4 Magnetic susceptibility and Currie-Weiss law

When a substance is placed in magnetic field $\boldsymbol{H}$, a magnetization $\boldsymbol{M}$ is induced in the substance which shows a relationship with $\boldsymbol{H}$ by equation $\boldsymbol{M} = \chi\boldsymbol{H}$. The proportional coefficient χ is known as magnetic susceptibility of the substance. The values of χ and by their temperature and field dependences could be important aspects to distinguish the several different kinds of magnetic behavior. For diamagnetic substances, χ is very small and slightly negative. For paramagnetic substances, χ is small and positive. In ferromagnetic substances, $\chi < 1$ and such materials are strongly interacted with a magnetic field. In antiferromagnetic substances, χ is positive and the value may be comparable to or somewhat less than that for paramagnetic substances[57].

Besides the absolute magnitudes, the susceptibilities of different kinds of magnetic material are also distinguished by their temperature dependences. Ordered magnetic structures, whether ferro-, ferri-, antiferro-, heli-magnetic or spin glass, tend to lose their ordered states above a temperature known as either the Curie temperature, T_C (ferro- and ferri-magnets), or the Neel point, T_N (antiferro- and heli-magnets); the spins become to align disorderedly and therefore the materials become paramagnetic. At these transition temperatures, there is a balance between the exchange interactions and the thermal energy, in which the former maintains the ordered-aligned structures and the latter tend to randomize the orientation of spins. **Figure 1.9** describes the schematic diagram of the temperature dependence of the magnetic susceptibility of different magnetic behaviors.

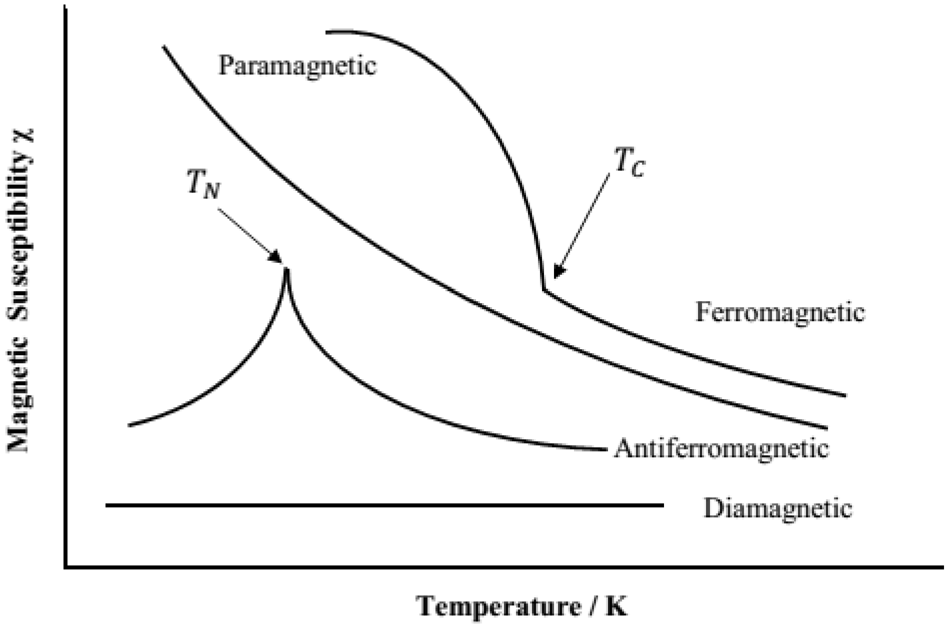

Figure 1.9 The temperature dependence of the magnetic susceptibility of diamagnetic, paramagnetic, ferromagnetic and antiferromagnetic materials[55].

Paramagnetic materials may obey the simple Curie law. It states that magnetic susceptibility of a material is inversely proportional to temperature: $\chi = C/T$ where C is Curie constant. Such a Curie behavior is observed when no spontaneous interaction exists between adjacent unpaired electrons[58]. They do try to align orderedly, but this alignment becomes more difficult with temperature increasing and therefore χ decreases. A more general Curie-Weiss law, $\chi = C/T - \theta$, is developed considering the case when there is spontaneous interaction between adjacent spins. In this equation, Weiss temperature (θ) can either be positive, negative or zero. When $\theta = 0$ then the Curie-Weiss law is equivalent to Curie's law. If θ is positive, ferromagnetic interaction is dominated; if θ is negative, antiferromagnetic interaction is dominated. **Figure 1.10** depicts the schematic diagrams of Currie's law and Curie-Weiss law. Based on Currie's law or Curie-Weiss law, one can calculate the effective moment from Currie constant by using the equation $\mu_{\mathrm{eff}} = 2.84\sqrt{\chi(T-\theta)} = 2.84\sqrt{C}$.[58]

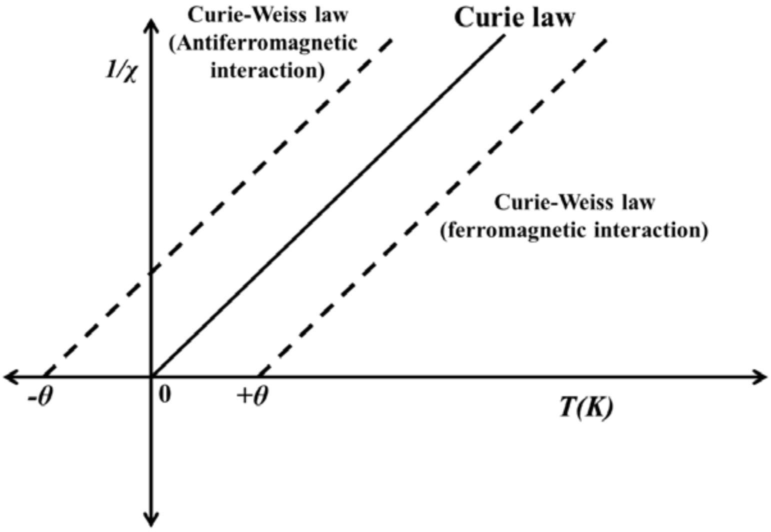

Figure 1.10 Schematic diagrams of Curie's law and Curie-Weiss law[58].

1.6 Magnetic interaction

1.6.1 Exchange interaction

Magnetic ordering originates from electrostatic interactions at a quantum mechanical level. The exchange interaction depicts the discreet magnetic moments interacted mutually through a quantum mechanical force. Hamiltonian, $\hat{H} = -2J\mathrm{S}_{\mathrm{i}} \bullet \mathrm{S}_{\mathrm{j}}$ is usually used to describe the exchange between two magnetic ions with spin $\mathbf{S}_{\mathrm{i}}$ and $\mathbf{S}_{\mathrm{j}}$. Extended it to many body system gives the Hamiltonian of the Heisenberg model: $\hat{H} = -\sum_{ij} J_{ij}\mathrm{S}_{\mathrm{i}} \bullet \mathrm{S}_{\mathrm{j}}$, where J_{ij} is known as the magnetic exchange constant between the spins of ion i$^{\mathrm{th}}$ and ion j$^{\mathrm{th}}$ and its absolute value represents the strength of the magnetic interaction. A material with strong magnetic interactions usually shows magnetic ordering transition at higher temperatures. One can estimate whether the exchange interacion is ferro- or antiferromagnetic according to the sign of J. When $J > 0$, the interaction favors a parallel alignment of two spins, i.e. ferromagnetically, when $J < 0$, it favors anti-parallel alignment of two spins, i.e. antiferromagnetically[59].

Two types of magnetic interactions are important for perovskite related materials, i.e. superexchange and double exchange. They are described in the following two sections. These two exchanges belong to indirect exchanges because the two magnetic ions concerned do not interact with each other directly, instead the interaction is mediated by a non-magnetic ion.

1.6.2 Superexchange

Superexchange is an indirect interaction between two magnetic cations (M_1 and M_2) via an intervening anion often O^{2-} ($2p^6$). It is also known as Kramers–Anderson superexchange. It arises because there is a kinetic energy that favors antiferromagnetism, it can be illustrated in **Figure 1.11**. If the moments of magnetic ions are aligned parallel (ferromagnetic), then the possible excited states of this system cannot exist as it breaks the Pauli exclusion principle. However, the excited states of the antiferromagnetic state are allowed. Therefore, if the two magnetic ions are aligned antiferromagnetically, the electrons on all three sites are delocalized over the whole structure thus lowering the kinetic energy. In addition, the kinetic energy depends on the degree of overlap of the orbitals and thus superexchange interaction is strongly dependent on the angle of the M_1-O-M_2.

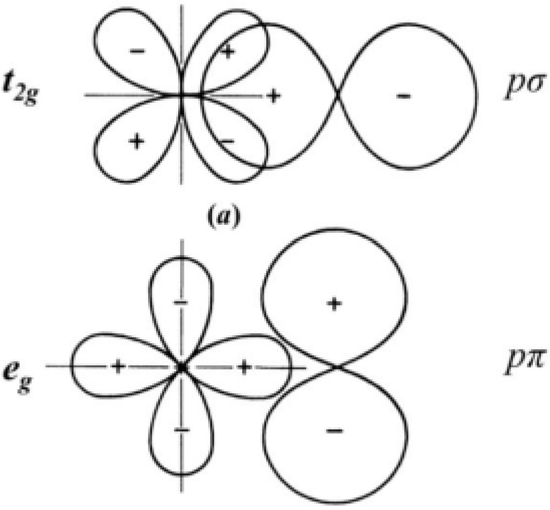

Figure 1.11 Schematic diagrams of $p\sigma$ orbital and $p\pi$ orbital[58].

A represented example of how the superexchange mechanism can be used to explain antiferromagnetic ordering is NiO. The Ni^{2+} ion is situated in an octahedral environment with electron configuration $t^6_{2g}\ e^1_g\ (d^2_{xy}d^2_{xz}d^2_{yz}d^1_{z2}d^1_{x2-y2})$. If we consider the linear 180° overlap between the Ni $3d_{x2-y2}$ and the O $2p_x$ orbitals (as depicted in **Figure 1.12**), it is obvious that the unpaired electrons in the e_g orbitals of the Ni^{2+} cations are able to couple magnetically with the electrons in the p orbitals of the O^{2-} anions in order to form the lowest possible energy state[55].

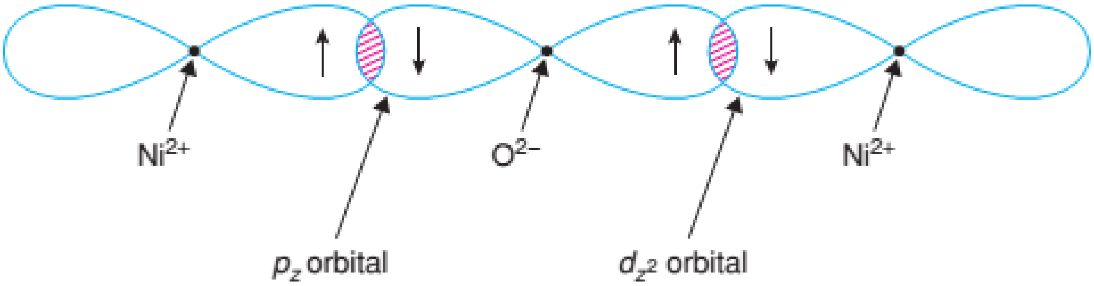

Figure 1.12 Antiferromagnetic coupling of spins of *d* electrons on Ni^{2+} ions through *p* electrons of oxide ions[55].

1.6.2 Double exchange

The double exchange interaction which was proposed by Zener is most relevant in mixed valence materials, such a compound that contains Mn^{3+} and Mn^{4+} *via* an intermediate anion[57, 60]. **Figure1.13** illustrates the principles of double exchange in mixed-valence contained compound. The crystal field causes the d-levels splitting into the e_g and t_{2g} levels. The Mn^{3+} electron is able to ‘hop’ to the vacancy in the Mn^{4+} e_g orbitals via an intervening O^{2-} anion without changing their spin direction. In this way, in order for electron spins to be conserved, the t_{2g} electrons on the Mn^{4+} cation must be ferromagnetically aligned with the t_{2g} electrons on the Mn^{3+} cation., as the antiferromagnetic arrangement would break Hund’s rules when such hopping occurred[61, 62].

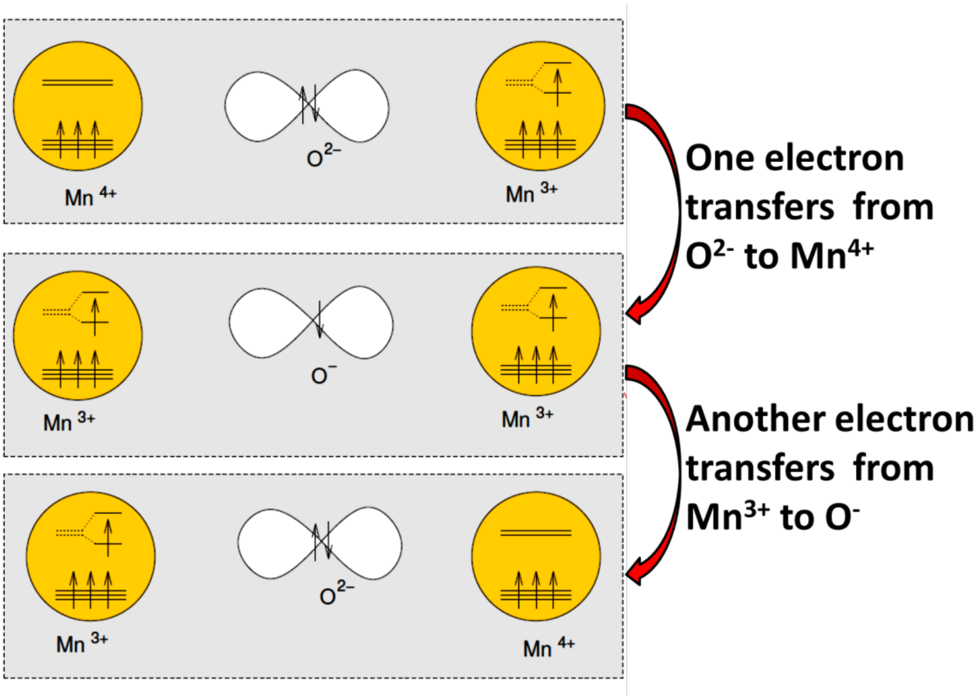

One electron transfers from O^{2-} to Mn^{4+}

Another electron transfers from Mn^{3+} to O^{-}

Figure 1.13 Schematic diagram of double exchange in mixed-valences manganite[61].

1.7 Flexibility of Ruddlesden-Popper phases

The perovskites are known for their flexibility not only with regards to oxygen stoichiometry but also in terms of A and B cation substitutions. The Ruddlesden-Popper phases also possess this kind of flexibility. There have been a great numbers of studies on cation substitution. As a famous example, substitution La^{3+} with M^{2+} in La_2CuO_4 has been proved to undergo a superconducting transition of the composition $La_{2-\delta}M_{\delta}CuO_4$[63-65]. In addition doping excess oxygen of La_2CuO_4 thus introducing mixed Cu oxidation states also induces superconducting property. Researches show that $La_2CuO_{4+\delta}$ up to $\delta = 0.07$ has already been synthesized at ambient temperature by electrochemistry, which induces the material to high-Tc superconductor (Tc = 44 K). Besides excess oxygen, these compounds with oxygen deficiency can be achieved by different reducing techniques. The deficiency of oxygen induces symmetry lowering, disorder and re-ordering at long range, structural defects, etc[66]. However, the main structure does not collapse but undergoes topotactic transformations. La_2CuO_{4-x} have been well studied, depending on which kind of oxygen is lacking, i.e. apical or equatorial, different prototypes are put forward for describing La_2CuO_{4-x}. The well accepted model is the S type structure, in which equatorial sites are only half occupied by oxygen, leaving ordered vacancies and CuO_4 square planes are arranged along c axis, as shown in **Figure 1.14**[67]. This type of structure is well studied in the field of high-T_C superconductors[68].

Besides cation doped and oxygen varied RP phase, anion doped RP phase are drawn more and more attentions recently. Compared with the other two strategies, anion doping seems a little difficult because of the strong bond of the metal-oxygen. And also that each anion possesses specific characteristics, including electronegativity, polarizability, ionic radius, and valence state that prevent the possibilities of anion doping. However, recent studies show the successful substitution. And considering that the anion strongly affects the crystal field and electronic state of the metal center, we can expect that substitution of anions with different bonding nature, valence state or ionic radius from oxygen in a metal oxide can enhance the original physical properties or induce new exotic phenomena.

Perovskite structure can also accommodate the anion doping, as seen in Sr(Nb/Ta)O_2N[69, 70], but because of the identical environment of the anion, anion seems to occupy oxygen sites disorderedly, the perovskite structure almost does not change and the symmetry either. And it makes it difficult to explore heterogeneous structure with exotic phenomena compared with perovskite.

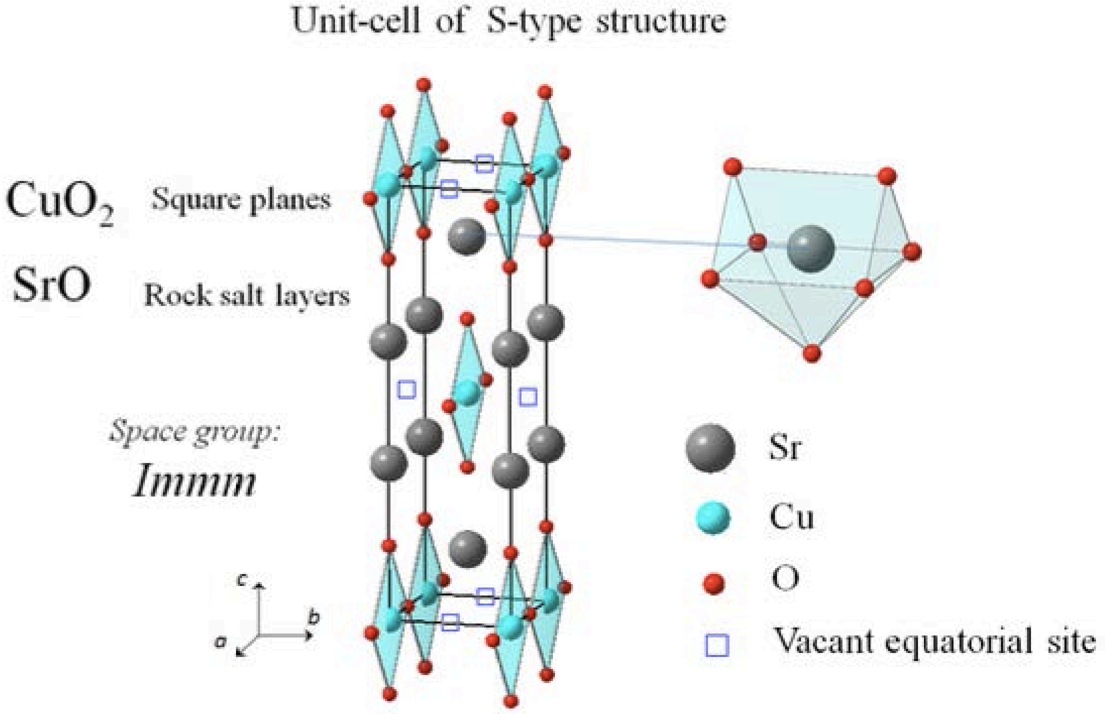

Figure 1.14 Crystal structure of the S type Sr_2CuO_{4-x}[67].

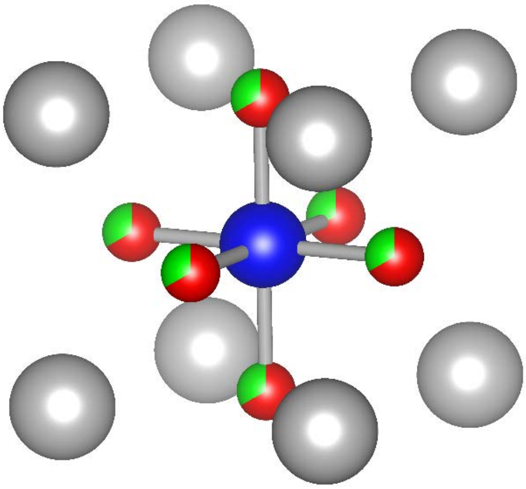

Figure 1.15 Crystal structure of Sr(Nb/Ta)O_2N, blue， grey, red, and green spheres represents Nb/Ta, Sr, O and N, respectively.

For layered perovskite structure, because there are several different anion sites, anion tends to occupy orderedly. In $n = 1$ RP type structure, A_2BO_4, two anion sites exist and several ordered states were discovered. In $Sr_2(Nb/Ta)O_3N$, equatorial sites were occupied by oxygen and nitrogen disorderedly while the apical site is fully occupied by oxygen[71, 72]. In Sr_2VO_3H[73], H occupied the O2 (which site ? label of define each sphere in Fig 1.16) site linearly and orderedly, leading the space group from *I*4/mmm to *Immm*. This can also be observed in $Sr_3Co_2O_{4.33}H_{0.84}$[74], $LaSrMnO_{3.3}H_{0.7}$[75] and $LaSrCoO_3H_{0.7}$[76]. In $NdAlO_3N$, N occupied one of the apical site of octahedra, lowering the symmetry to *I*4mm. These all indicate that the anion doped RP type structure may provide different structures and thus may induce some intriguing properties.

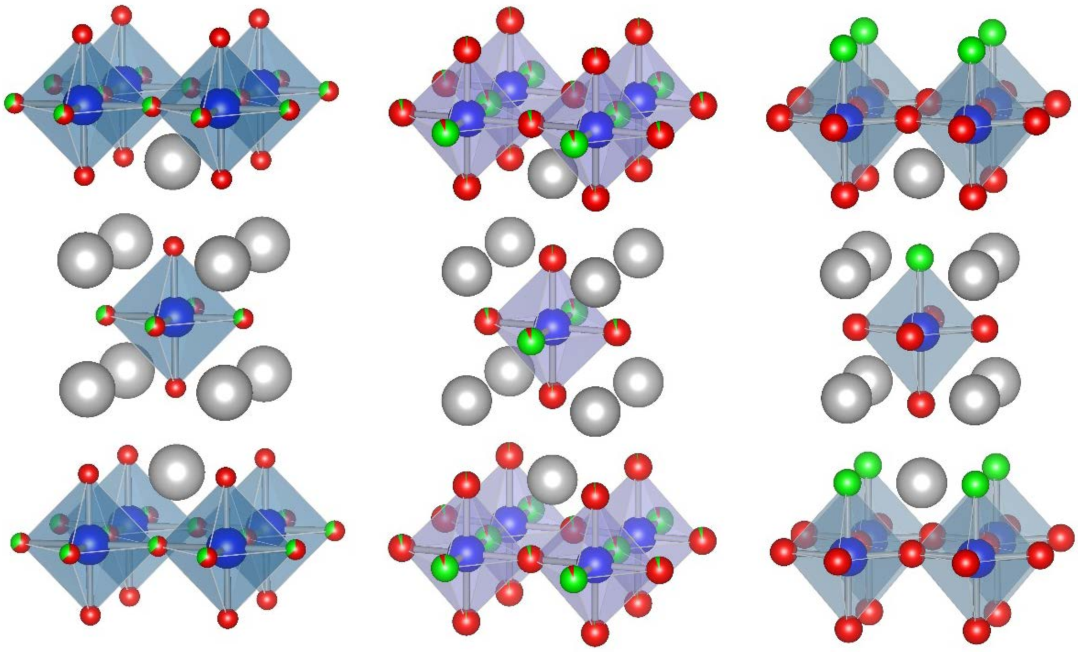

Figure 1.16 From left to right: Crystal structure of $Sr_2(Nb/Ta)O_3N$, Sr_2VO_3H, and $NdAlO_3N$. Grey, blue, red and green spheres represent *A*, *B*, O and H/N.

1.8 Objectives of this thesis

As aforementioned, the coordination environment around metal centers of Ruddlesden-Popper phases can be modified by anion substitution in a way that different from cation substitution. Of several mixed anion systems, layered oxyhalide compounds give unique structural features as follows. First, halide ions selectively occupy the apical anion sites, leading to full or partial anion order. Second, the coordination number of the metal center can be reduced by changing the halide-to-oxygen ratio. These structural features provide good opportunities for tuning the electronic structure, crystal field splitting energy, charge transfer energy, exchange interactions in non-doped RP phases, To date, many layered oxyhalide perovskites have been reported, such as Sr_2BO_3F (B = Fe, Co, Ni, Sc, etc.) and $A_2BO_2X_2$ (A = Sr, Ba, Ca, B = Cu, Co, Ni, Pd, X = F, Cl, etc.), and their structures and properties were studied. **Table 1.2** lists the coordination environment of the transition metal centers for A_2BO_3X and $A_2BO_2X_2$. Basically, the RP type structure with the general formula $A_2BO_2X_2$ exclusively possesses a tetragonally distorted octahedron for the *B* site, which is surrounded by four oxide ions at the equatorial sites and two apical halide ions (**Figure 1.17**). However, the interaction between the *B* cation and halide ions is considerably weak, so the coordination geometry for the *B* cation can be effectively viewed as a square plane. For $Sr_2NiO_2Cl_2$ and $Sr_2MnO_2Cl_2$,which was synthesized in 2014, the square planar is very unique since Ni^{2+} and Mn^{2+} are not Jahn-Teller active and do not prefer square planar coordination. The discovery of these phases opens up further possibilities for extending square-planar coordinated systems. In contrast, A_2BO_3X exhibits complex relationship between the coordination geometry of the *B* cation and the O/*X* anion order. (LaCa)CuO_3Cl has a square planar coordination for Cu ion. The copper ion is bonded to four oxide ions at the equatorial sites and one chloride ion at the apical site. Owing to the Jahn-Teller activity of Cu ion, however, the Cu-Cl bond length is much longer than that expected from the ionic model. In contrast, Sr_2BO_3X (*B* = Fe, Co, Ni; *X* = F, Cl), Sr_2MnO_3Cl, and Sr_2CrO_3F exhibit a square pyramidal coordination of BO_5. The halide ions are very loosely bound bonded to the *B* cation, although the fluoride (chloride) ions tend to occupy the apical site with oxide ion in a disordered (ordered) manner. Compared with the pyramidally coordinated oxyhalides, the octahedral geometry for Sc ion observed in Sr_2ScO_3F is quite unusual but the mechanism for the octahedral coordination has not been clear yet.

My thesis has focused on the synthesis of new oxyhalide compounds with unusual coordination environment, especially A_2BO_3X and $A_2BO_2X_2$ family. As seen in **Table 1.2**, there are still a lot of the members of this family which remain to be explored. Manganese based compounds are well known to exhibit a lot of attractive properties originated from competition between spin, charge, and orbital degrees of freedom, for example, metal-insulator transition, and colossal magnetoresistance (CMR). Thus we can expect layered manganese perovskites may have some interesting properties. Hence in this thesis, Sr_2MnO_3F and $Sr_2MnO_2Cl_2$ were investigated. Zinc containing compounds also show a lot of interesting properties, such as their exceptional optical, magnetic and electronic properties. But the variety of the coordination is generally limited to tetrahedral, thus leaving a lot of possibilities either to prepare compounds with unusual coordination environment or properties. Therefore we focused on zinc based compounds with square planar coordination and investigated $Sr_2ZnO_2Cl_2$ in this thesis. Based on this motivation, several research works have been done.

Table 1.2 Reported layered oxyhalide compounds with $n = 1$ RP structure. Compounds written with bold font were reported by my colleagues.

	$A_2B^{3+}O_3X$		$A_2B^{2+}O_2X_2$	
	F	Cl	F	Cl
Sc	octahedra[77]	-	-	-
V	-	-	-	-
Cr	pyramid[78]	-	-	-
Mn	**this study**	pyramid[79]	-	**this study**
Fe	**pyramid** **[80]**	pyramid[81]	-	-
Co	**pyramid[82]**	**pyramid[83]**	-	square planar[84]
Ni	**pyramid[85]**	**pyramid[85]**	-	**square planar[86]**
Cu	-	square planar[87]	square planar[36]	square planar[21]
Zn	-	-	-	**this study**

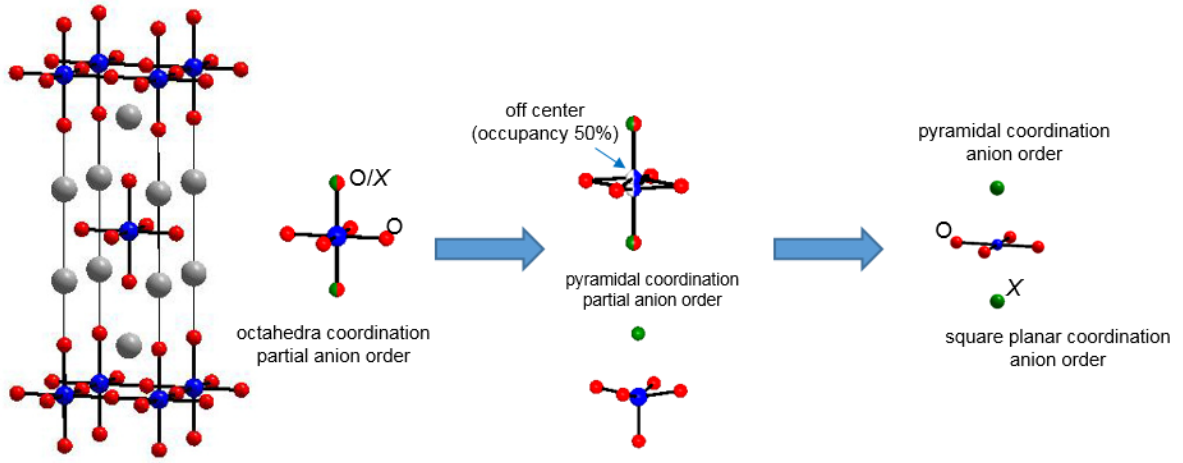

Figure 1.17 Anion lattice engineering design.

The thesis consists of six chapters. A brief introduction to crystal structure, magnetism was presented in **Chapter 1**. The description of the high pressure techniques and characterization of the properties used in this thesis, containing X-ray diffraction, magnetization, Synchrotron Powder diffraction, UV-vis spectrum, was given in **Chapter 2**. Layered RP-type Sr_2MnO_3F was presented in **Chapter 3**. The manganese oxyfluoride exhibits unique structural features that have never been observed in any other related layered oxyhalides: the coexistence of anion disorder between O and F at the apical sites and the octahedral coordination subject to the 1st order Jahn-Teller effect. The MnO2 planes separated by non-magnetic Sr(O/F) rock-salt layers result in low-dimensional magnetic correlations with $T_N = 133$ K, which is totally different from paramagnetic behaviors observed in known RP type layered manganese oxyfluorides. To explore new oxychloride with square planar coordination, $Sr_2ZnO_2Cl_2$ was prepared using high pressure method, which would be discussed in **Chapter 4**. To explore notable magnetic behavior with RP-type structure, $Sr_2MnO_2Cl_2$ was prepared by high pressure method. Short range order develops at 80K, no long-range magnetic order down to 2 K, which is different with the K_2NiF_4 series. The detailed crystal structure and magnetic properties would be discussed in **Chapter 5**. In **Chapter 6** revealed a general conclusion and outlines some prospects for follow-up research.

References in Chapter 1

1. Tybell, T., C.H. Ahn, and J.M. Triscone, *Ferroelectricity in thin perovskite films.* Applied Physics Letters, 1999. **75**(6), 856-858.

2. Nemeth, Z., Z. Homonnay, F. Arva, Z. Klencsar, E. Kuzmann, J. Hakl, K. Vad, S. Meszaros, K. Kellner, G. Gritzner, and A. Vertes, *Mossbauer and magnetic studies of* $La_{0.8}Sr_{0.2}CoO_{3}$*-delta CMR perovskite.* Journal of Radioanalytical and Nuclear Chemistry, 2007. **271**(1), 11-17.

3. Raveau, B., A. Maignan, C. Martin, and M. Hervieu, *Ru doping of perovskite manganites: An effective route to ferromagnetism, metallicity, CMR.* Journal of Superconductivity, 2001. **14**(2), 217-229.

4. Halmi, M., G. Desgardin, and B. Raveau, *Improved Lead Perovskite Compounds (PFn-PFt) for* Z_5U*Capacitor Applications.* Advanced Ceramic Materials, 1988. **3**(1), 32-37.

5. Guo, R.J., Y.P. Guo, H.A. Duan, H. Li, and H.Z. Liu, *Synthesis of Orthorhombic Perovskite-Type* $ZnSnO_3$ *Single-Crystal Nanoplates and Their Application in Energy Harvesting.* Acs Applied Materials & Interfaces, 2017. **9**(9), 8271-8279.

6. Gupta, S., T. Bendikov, G. Hodes, and D. Cahen, $CsSnBr_3$*, A Lead-Free Halide Perovskite for Long-Term Solar Cell Application: Insights on* SnF_2 *Addition.* Acs Energy Letters, 2016. **1**(5), 1028-1033.

7. Hu, C.C., C.C. Tsai, and H. Teng, *Structure Characterization and Tuning of Perovskite-Like* $NaTaO_3$ *for Applications in Photoluminescence and Photocatalysis.* Journal of the

American Ceramic Society, 2009. **92**(2), 460-466.

8. Shen, Z.B., X.H. Wang, B.C. Luo, and L.T. Li, *$BaTiO_3$-$BiYbO_3$ perovskite materials for energy storage applications.* Journal of Materials Chemistry A, 2015. **3**(35), 18146-18153.

9. Anderson, M.T., K.B. Greenwood, G.A. Taylor, and K.R. Poeppelmeier, *B-Cation Arrangements in Double Perovskites.* Progress in Solid State Chemistry, 1993. **22**(3), 197-233.

10. Pena, M.A. and J.L.G. Fierro, *Chemical structures and performance of perovskite oxides.* Chemical Reviews, 2001. **101**(7), 1981-2017.

11. Davies, P.K., H. Wu, A.Y. Borisevich, I.E. Molodetsky, and L. Farber, *Crystal chemistry of complex perovskites: New cation-ordered dielectric oxides.* Annual Review of Materials Research, 2008. **38**, 369-401.

12. Ruddlesden, S.N. and P. Popper, *The Compound $Sr_3Ti_2O_7$ and Its Structure.* Acta Crystallographica, 1958. **11**(1), 54-55.

13. Beznosikov, B.V. and K.S. Aleksandrov, *Perovskite-like crystals of the Ruddlesden-Popper series.* Crystallography Reports, 2000. **45**(5), 792-798.

14. Bariev, R.Z., *Correlation-Functions of the Semi-Infinite Two-Dimensional Ising-Model .1. Local Magnetization.* Theoretical and Mathematical Physics, 1979. **40**(1), 623-626.

15. Mazenko, G.F., J.E. Hirsch, M.J. Nolan, and O.T. Valls, *Dynamical Correlation-Functions in the Two-Dimensional Kinetic Ising-Model - a Real-Space Renormalization-Group Approach.* Physical Review Letters, 1980. **44**(16), 1083-1086.

16. Bariev, R.Z., *Correlation-Functions of the Semi-Infinite Two-Dimensional Ising-Model .2. 2-Point Correlation-Functions.* Theoretical and Mathematical Physics, 1980. **42**(2), 173-178.

17. Bhattacharjee, S.M. and A. Khare, *Fifty years of the exact solution of the two-dimensional Ising model by Onsager.* Current Science, 1995. **69**(10), 816-821.

18. Mermin, N.D. and H. Wagner, *Absence of Ferromagnetism or Antiferromagnetism in One- or 2-Dimensional Isotropic Heisenberg Models.* Physical Review Letters, 1966. **17**(22), 1133-

&.

19. Ruddlesden, S.N. and P. Popper, *New Compounds of the* K_2NiF_4 *Type.* Acta Crystallographica, 1957. **10**(8), 538-540.

20. Birgeneau, R.J., H.J. Guggenheim, and G. Shirane, *Neutron Scattering from* K_2NiF_4 *- a 2-Dimensional Heisenberg Antiferromagnet.* Physical Review Letters, 1969. **22**(14), 720-+.

21. Miller, L.L., X.L. Wang, S.X. Wang, C. Stassis, D.C. Johnston, J. Faber, and C.K. Loong, *Synthesis, Structure, and Properties of* $Sr_2CuO_2Cl_2$*.* Physical Review B, 1990. **41**(4), 1921-1925.

22. Degennes, P.G. and E. Guyon, *Superconductivity in Normal Metals.* Physics Letters, 1963. **3**(4), 168-169.

23. Boorse, H.A., D.B. Cook, and M.W. Zemansky, *Superconductivity of Lead.* Physical Review, 1950. **78**(5), 635-636.

24. Domashnev, I.A., O.M. Grebtsova, O.D. Torbova, and V.N. Troitskii, *Synthesis and Superconductivity of Niobium Nitride.* Inorganic Materials, 1983. **19**(6), 819-822.

25. Wexler, A. and W.S. Corak, *Superconductivity of Vanadium.* Physical Review, 1952. **85**(1), 85-90.

26. Bardeen, J., L.N. Cooper, and J.R. Schrieffer, *Theory of Superconductivity.* Physical Review, 1957. **108**(5), 1175-1204.

27. Alexandrov, A.S., *Theory of High Temperature Superconductivity Beyond BCS with Realistic Coulomb and Frohlich Interactions.* Journal of Superconductivity and Novel Magnetism, 2013. **26**(4), 1313-1317.

28. Baral, P.C. and G.C. Rout, *A modified BCS theory of heavy fermion superconductivity.* Indian Journal of Physics, 2012. **86**(6), 431-437.

29. Hirsch, J.E., *BCS theory of superconductivity: it is time to question its validity.* Physica Scripta, 2009. **80**(3).

30. Bennemann, K.H., *On High-Tc Superconductivity in* La_2CuO_4*-Type Compounds.* Physics

Letters A, 1987. **126**(1), 67-70.

31. Tholence, J.L., *Superconductivity of* La_2CuO_4 *and* $Yba_2Cu_3O_7$*.* Physica B & C, 1987. **148**(1-3), 353-356.

32. Shaheen, S.A., N. Jisrawi, Y.H. Lee, Y.Z. Zhang, M. Croft, W.L. Mclean, H. Zhen, L. Rebelsky, and S. Horn, *Superconductivity in La-Deficient and Stoichiometric* La_2CuO_4*.* Physical Review B, 1987. **36**(13), 7214-7217.

33. Fine, S.M., M. Greenblatt, S. Simizu, and S.A. Friedberg, *Effect of Nominal Composition on Superconductivity in* La_2ACuO_{4-Y}*.* Acs Symposium Series, 1987. **351**, 95-101.

34. Shimada, D., Y. Shiina, N. Miyakawa, and N. Tsuda, *Phonon contribution to superconductivity of* $Bi_2Sr_2CaCu_2O_8$*.* Physica B: Condensed Matter, 1996. **219–220**, 192-194.

35. Kondo, R., K. Kawatani, F. Ichikawa, T. Fukami, and T. Aomine, *Hysteretic effect of sound velocity in sintered* $Bi_2Sr_2CaCu_2O_{8+\delta}$ *with excess oxygen.* Physica B: Condensed Matter, 1996. **219–220**, 195-197.

36. Almamouri, M., P.P. Edwards, C. Greaves, and M. Slaski, *Synthesis and Superconducting Properties of the Strontium Copper Oxyfluoride* $Sr_2CuO_2F_{2+\delta}$*.* Nature, 1994. **369**(6479), 382-384.

37. Miessler G. L and T. D.A., *Inorganic Chemistry*. 2004: Pearson Education.

38. Tokura, Y. and N. Nagaosa, *Orbital physics in transition-metal oxides.* Science, 2000. **288**(5465), 462-468.

39. Rodriguez, E., M.L. Lopez, J. Campo, M.L. Veiga, and C. Pico, *Crystal and magnetic structure of the perovskites* La_2MTiO_6 *(M = Co, Ni).* Journal of Materials Chemistry, 2002. **12**(9), 2798-2802.

40. Ju, S., T.Y. Cai, H.S. Lu, and C.D. Gong, *Pressure-Induced Crystal Structure and Spin-State Transitions in Magnetite (*Fe_3O_4*).* Journal of the American Chemical Society, 2012. **134**(33), 13780-13786.

41. Ding, Y., D. Haskel, S.G. Ovchinnikov, Y.C. Tseng, Y.S. Orlov, J.C. Lang, and H.K. Mao,

Novel pressure-induced magnetic transition in magnetite (Fe_3O_4). Physical Review Letters, 2008. **100**(4).

42. Valant, M., A.K. Axelsson, and N. Alford, *Peculiarities of a solid-state synthesis of multiferroic polycrystalline $BiFeO_3$.* Chemistry of Materials, 2007. **19**(22), 5431-5436.

43. Baettig, P., R. Seshadri, and N.A. Spaldin, *Anti-polarity in ideal $BiMnO_3$.* Journal of the American Chemical Society, 2007. **129**(32), 9854-+.

44. Azuma, M., S. Carlsson, J. Rodgers, M.G. Tucker, M. Tsujimoto, S. Ishiwata, S. Isoda, Y. Shimakawa, M. Takano, and J.P. Attfield, *Pressure-induced intermetallic valence transition in $BiNiO_3$.* Journal of the American Chemical Society, 2007. **129**(46), 14433-14436.

45. Viola, M.C., M.J. Martinez-Lope, J.A. Alonso, P. Velasco, J.L. Martinez, J.C. Pedregosa, R.E. Carbonio, and M.T. Fernandez-Diaz, *Induction of colossal magnetoresistance in the double perovskite Sr_2CoMoO_6.* Chemistry of Materials, 2002. **14**(2), 812-818.

46. Obrien, M.C.M. and C.C. Chancey, *The Jahn-Teller Effect - an Introduction and Current Review.* American Journal of Physics, 1993. **61**(8), 688-697.

47. Vallin, J.T. and G.D. Watkins, *The Jahn-teller effect for Cr^{2+} in II–VI crystals.* Solid State Communications, 1971. **9**(13), 953-956.

48. Alonso, J.A., M.J. Martínez-Lope, M.T. Casais, and M.T. Fernández-Díaz, *Evolution of the Jahn−Teller Distortion of MnO6 Octahedra in $RMnO_3$ Perovskites (R = Pr, Nd, Dy, Tb, Ho, Er, Y): A Neutron Diffraction Study.* Inorganic Chemistry, 2000. **39**(5), 917-923.

49. Lufaso, M.W., W.R. Gemmill, S.J. Mugavero Iii, S.-J. Kim, Y. Lee, T. Vogt, and H.-C. zur Loye, *Synthesis, structure, magnetic properties and structural distortion under high pressure of a new osmate, Sr_2CuOsO_6.* Journal of Solid State Chemistry, 2008. **181**(3), 623-627.

50. Attfield, M.P., P.D. Battle, S.K. Bollen, S.H. Kim, A.V. Powell, and M. Workman, *Structural and electrical studies of mixed copper/ruthenium oxides and related compounds of zinc and antimony.* Journal of Solid State Chemistry, 1992. **96**(2), 344-359.

51. Todate, Y., *Antiferromagnetism and Frustration in Ba_2CuWO_6.* Journal of the Physical

Society of Japan, 2001. **70**(2), 337-340.

52. Cotton, F.A., G. Wilkinson, C.A. Murillo, M. Bochmann, and R. Grimes, *Advanced inorganic chemistry*. Vol. 5. 1988: Wiley New York.

53. Handley, O. and C. Robert, *Modern Magnetic Materials: Principles and Applications*. 2000, New York, USA: Wiley.

54. Griffith, J.S., *The theory of transition-metal ions*. 1961, Cambridge: Cambridge university press.

55. West, A.R., *Solid State Chemistry and its Application*. 2014, University of Sheffield, UK: Wiley.

56. Koshibae, W., Y. Kawamura, S. Ishihara, S. Okamoto, J. Inoue, and S. Maekawa, *Interplay of spin and orbital orderings in perovskite manganites.* Journal of the Physical Society of Japan, 1997. **66**(4), 957-960.

57. Landolt and Bornstein, *Numerical Data and Functional Relationships in Science and Technology*. 1986, Heidelberg: Springer-Verlag.

58. Kittle, C., *Introduction to solid state physics*. 2004: Wiley.

59. Blundell, S., *Magnetism in Condensed Matter*. 2001: Oxford University Press, UK.

60. Anderson, P.W. and H. Hasegawa, *Considerations on Double Exchange.* Physical Review, 1955. **100**(2), 675-681.

61. Bhaskar, A., C.-J. Liu, J.J. Yuan, and C.-L. Chang, *Thermoelectric properties of n-type* $Ca_{1-x}Bi_xMn_{1-y}Si_yO_{3-\delta}$ *(x = y = 0.00, 0.02, 0.03, 0.04, and 0.05) system.* Journal of Alloys and Compounds, 2013. **552**, 236-239.

62. Raveau, B., Y.M. Zhao, C. Martin, M. Hervieu, and A. Maignan, *Mn-Site Doped* $CaMnO_3$*: Creation of the CMR Effect.* Journal of Solid State Chemistry, 2000. **149**(1), 203-207.

63. Koyama, Y., Y. Wakabayashi, K. Ito, and Y. Inoue, *Low-temperature structural transitions and Low-temperature structural transitions and Tc suppression in* $La_{2-x}M_xCuO_4$ *(M=Ba, Sr).* Physical Review B, 1995. **51**(14), 9045-9051.

64. Attfield, J.P., A.L. Kharlanov, and J.A. McAllister, *Cation effects in doped* La_2CuO_4 *superconductors.* Nature, 1998. **394**(6689), 157-159.

65. Shamoto, S., M. Onoda, M. Sato, and S. Hosoya, *Anisotropy of the Superconducting Critical Magnetic Field* H_{c2} *of La–M–Cu–O System (M=Sr and Ba).* Japanese Journal of Applied Physics, 1987. **26**(S3-2), 1131.

66. Fisher, R.A., J.E. Gordon, and N.E. Phillips, *Some chemical and structural effects on the properties of high-Tc superconductors.* Annual Review of Physical Chemistry, 1996. **47**, 283-325.

67. Dréau, L.L., *Phase transitions and oxygen ordering in* $La_2CoO_{4+\delta}$ *and (T, T')-*La_2CuO_4*: single crystal growth and structural studies using synchrotron and neutron diffraction methods,* 2011, University of Rennes 1 France.

68. Hiroi, Z., M. Takano, M. Azuma, and Y. Takeda, *A New Family of Copper-Oxide Superconductors* $Sr_{n+1}Cu_nO_{2n+1+\delta}$ *Stabilized at High-Pressure.* Nature, 1993. **364**(6435), 315-317.

69. Tobias, G., D. Beltran-Porter, O.I. Lebedev, G. Van Tendeloo, J. Rodriguez-Carvajal, and A. Fuertes, *Anion ordering and defect structure in Ruddlesden-Popper strontium niobium oxynitrides.* Inorganic Chemistry, 2004. **43**(25), 8010-8017.

70. Yang, M.H., J. Oro-Sole, J.A. Rodgers, A.B. Jorge, A. Fuertes, and J.P. Attfield, *Anion order in perovskite oxynitrides.* Nature Chemistry, 2011. **3**(1), 47-52.

71. Tobias, G., J. Oro-Sole, D. Beltran-Porter, and A. Fuertes, *New family of Ruddlesden-Popper strontium niobium oxynitrides: (SrO)(SrNbO2-xN)(n) (n = 1, 2).* Inorganic Chemistry, 2001. **40**(27), 6867-+.

72. Clarke, S.J., K.A. Hardstone, C.W. Michie, and M.J. Rosseinsky, *High-temperature synthesis and structures of perovskite and n=1 Ruddlesden-Popper tantalum oxynitrides.* Chemistry of Materials, 2002. **14**(6), 2664-2669.

73. Bang, J., S. Matsuishi, S. Maki, J. Yamaura, M. Hiraishi, S. Takeshita, I. Yamauchi, K.M.

Kojima, and H. Hosono, *Low dimensionalization of magnetic ordering in Sr2VO4 by hydride ion substitution.* Physical Review B, 2015. **92**(6).

74. Helps, R.M., N.H. Rees, and M.A. Hayward, *Sr3Co2O4.33H0.84: An Extended Transition Metal Oxide-Hydride.* Inorganic Chemistry, 2010. **49**(23), 11062-11068.

75. Tassel, C., Y. Goto, D. Watabe, Y. Tang, H.C. Lu, Y. Kuno, F. Takeiri, T. Yamamoto, C.M. Brown, J. Hester, Y. Kobayashi, and H. Kageyama, *High-Pressure Synthesis of Manganese Oxyhydride with Partial Anion Order.* Angewandte Chemie-International Edition, 2016. **55**(33), 9666-9669.

76. Hayward, M.A., E.J. Cussen, J.B. Claridge, M. Bieringer, M.J. Rosseinsky, C.J. Kiely, S.J. Blundell, I.M. Marshall, and F.L. Pratt, *The hydride anion in an extended transition metal oxide array:* $LaSrCoO_3H_{0.7}$. Science, 2002. **295**(5561), 1882-1884.

77. Wang, Y.K., K.B. Tang, B.C. Zhu, D. Wang, Q.Y. Hao, and Y. Wang, *Synthesis and structure of a new layered oxyfluoride* Sr_2ScO_3F *with photocatalytic property.* Materials Research Bulletin, 2015. **65**, 42-46.

78. PENNY, S.L., *a Magnetic Structural Study of* $Tb_2Mo_2O_7$, Sr_2CrO_3F *and* $SrLaCrO_4$, in *Chemistry*1990, McMaster University: Hamilton, Ontario, Canada.

79. Knee, C.S., A.A. Zhukov, and M.T. Weller, *Crystal structures and magnetic properties of the manganese oxide chlorides* Sr_2MnO_3Cl *and* $Sr_4Mn_3O_{8-y}Cl_2$. Chemistry of Materials, 2002. **14**(10), 4249-4255.

80. Tsujimoto, Y., Y. Matsushita, N. Hayashi, K. Yamaura, and T. Uchikoshi, *Anion Order-to-Disorder Transition in Layered Iron Oxyfluoride* Sr_2FeO_3F *Single Crystals.* Crystal Growth & Design, 2014. **14**(9), 4278-4284.

81. Hector, A.L., J.A. Hutchings, R.L. Needs, M.F. Thomas, and M.T. Weller, *Structural and Mossbauer study of* Sr_2FeO_3X $(X = F, Cl, Br)$ *and the magnetic structure of* Sr_2FeO_3F. Journal of Materials Chemistry, 2001. **11**(2), 527-532.

82. Tsujimoto, Y., J.J. Li, K. Yamaura, Y. Matsushita, Y. Katsuya, M. Tanaka, Y. Shirako, M.

Akaogi, and E. Takayama-Muromachi, *New layered cobalt oxyfluoride,* Sr_2CoO_3F. Chemical Communications, 2011. **47**(11), 3263-3265.

83. Knee, C.S., D.J. Price, M.R. Lees, and M.T. Weller, *Two- and three-dimensional magnetic order in the layered cobalt oxychloride* Sr_2CoO_3Cl. Physical Review B, 2003. **68**(17).

84. Gui, H., X. Li, W.X. Lv, Z.J. Zhao, and W.H. Xie, *Structural and Electronic Properties of* $Sr_2CoO_2Cl_2$. Journal of Electronic Materials, 2016. **45**(10), 4843-4846.

85. Tsujimoto, Y., K. Yamaura, and T. Uchikoshi, *Extended Ni(III) Oxyhalide Perovskite Derivatives:* Sr_2NiO_3X *(X = F, Cl).* Inorganic Chemistry, 2013. **52**(17), 10211-10216.

86. Tsujimoto, Y., C.I. Sathish, Y. Matsushita, K. Yamaura, and T. Uchikoshi, *New members of layered oxychloride perovskites with square planar coordination:* $Sr_2MO_2Cl_2$ *(M = Mn, Ni) and* $Ba_2PdO_2Cl_2$. Chemical Communications, 2014. **50**(44), 5915-5918.

87. Fuller, R.L. and M. Greenblatt, *Synthesis, Structure, and Properties of a New T-Star Structure Copper-Oxychloride of* $MLnCuO_3Cl$ *(M = Ca, Sr and Ln = Nd, Sm, Eu, Gd).* Journal of Solid State Chemistry, 1991. **92**(2), 386-400.

Chapter 2 Experimental methods

High pressure synthesis was reported to be a useful approach to the synthesis of oxyfluoride, as it has several advantages, it can (i) stabilize dense structure; (ii) good for the formation of ordered structure; (iii) shorten the synthesis time; (iv) control evaporation of starting materials. In this thesis, all the samples were synthesized by using high pressure and high temperature method. Then the crystal structures, magnetic properties and other physical properties were characterized.

2.1 Sample preparation: high-pressure method

In this thesis, a belt-type high-pressure apparatus (Kobe Steel, Ltd.) was used to synthesize samples. The pressure and temperature range of the apparatus are 8 GPa and 2000°C, respectively. **Figure 2.1** shows the image of the high pressure apparatus and the schematic picture of the sample container and the capsule in which we put starting materials in. To obtain quasi-hydrostatic conditions, we used pyrophyllite cell[1]. The graphite plays a role as heating furnace to heat the samples. Inside the graphite furnace is the Pt capsule. To be insulated with graphite furnace, NaCl sleeve and two cylindrical pieces are used to block the contact of Pt and graphite.

To prepare samples, stoichiometric amounts of starting materials were mixed and ground thoroughly in an Ar-filled glove box. The mixtures were sealed and pressed into a Pt capsule by using hand press and the sealed Pt capsules were put into the sample cell as shown in **Figure 2.1**. Then the sample cell was put into high-pressure apparatus by certain position as shown in the right one of **Figure 2.1**. The pressure was increased slowly to the target pressure. After the pressure became stable, samples were then heated to certain temperatures and kept heating for certain time, the sample was quenched to room temperature by turning off the heater, or cooled down to 1200 °C for 30 min. Then the pressure was released slowly.

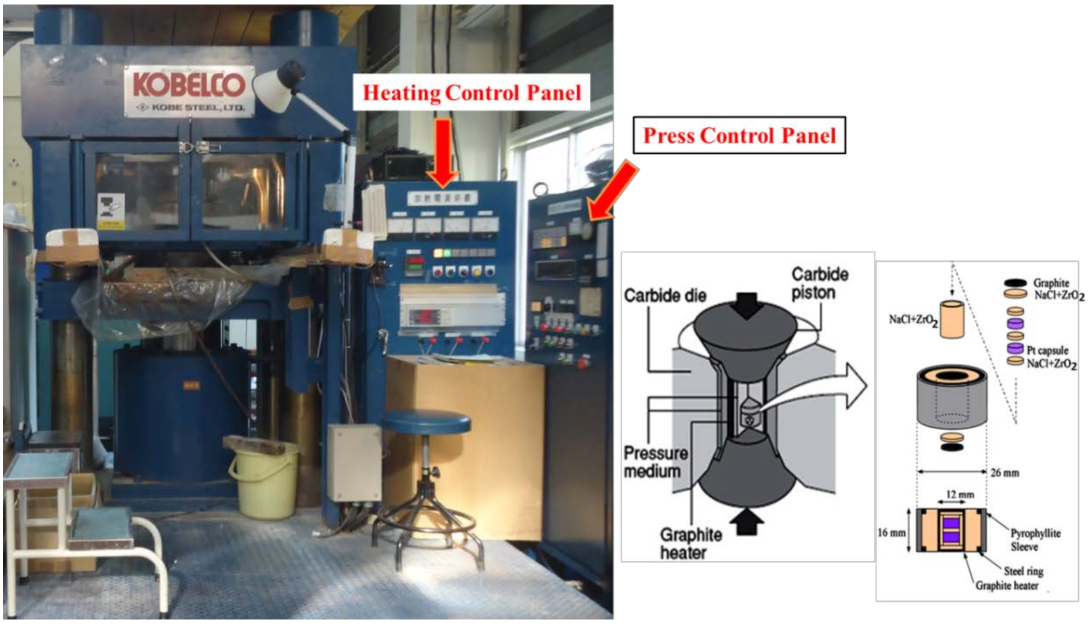

Figure 2.1 High pressure apparatus set in National Institute for Materials Science (NIMS), and the schematic diagram of the capsule and sample container.

2.2 X-ray diffraction

2.2.1 Powder X-ray diffraction

Powder X-ray diffraction (XRD) is a laboratory technique which is widely used for preliminary characterizations such as phase identification and structure determination. Room-temperature powder XRD data were collected from the products using a Desktop X-ray Diffractometer MiniFlex (Rigaku) equipped with a graphite monochromator and Cu Ka radiation ($\lambda = 1.5418$ Å), in 0.036° increments over the range $10° < 2\theta < 70°$ with scanning rate of 5°/min.

2.2.2 Synchrotron X-ray diffraction

Synchrotron radiation is emitted when charged particles such as electrons, are accelerated radially, i.e., when their acceleration is perpendicular to their velocity. Synchrotron radiation was first observed in 1947. Synchrotron X-ray Diffraction (SXRD) is a very useful technique to analyze unknown materials efficiently. To generate synchrotron radiation, electrons or positrons are accelerated to speeds which is close to that of light. And these high speed particles circulate in ultra-high vacuum tubes, or storage rings, made of certain arrangement of magnets. A simplified sketch of a storage ring is shown in **Figure 2.2**. It is worthy noted that synchrotron sources are very large scale national facilities. The diameter of the storage ring may be hundreds of meters.

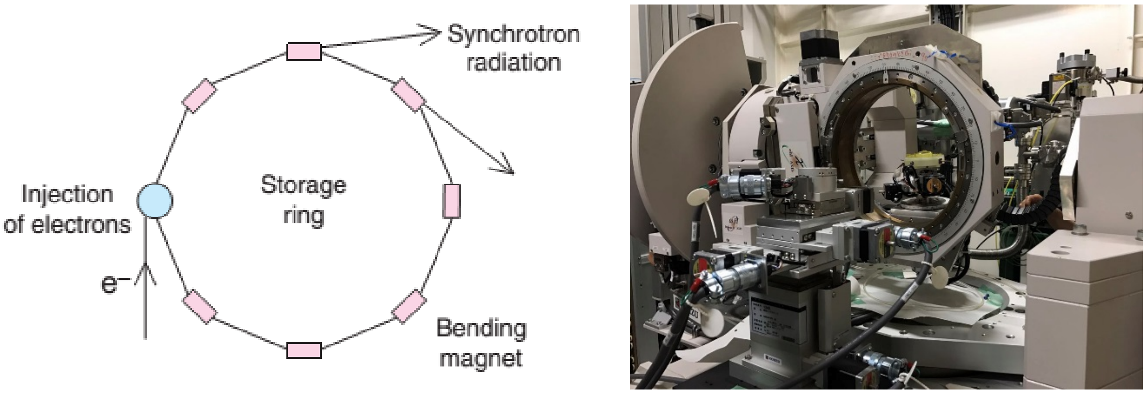

Figure 2.2 Schematic diagram of a synchrotron storage ring and a picture of BL15XU in Spring-8.

Synchrotron diffraction had several advantages. It is of very high intensity, which is at least 5 orders of magnitude more than the conventional X-ray laboratory source. The beams are accurately parallel, therefore it has a high resolution. The wavelength are continuous over the complete spectral range and are tunable, possible for energy-dispersive experiments.

Synchrotron XRD (SXRD) data were also collected at room temperature using a Debye-Scherrer camera installed on NIMS beamline (BL15XU) at SPring-8(the world's largest third-generation synchrotron radiation facility, short for super photon ring 8GeV), which is located in Harima Science Park City, Hyogo Prefecture, Japan[2]. The synchrotron radiation X-rays were monochromatized to the wavelength of 0.65298 Å. The samples were put in a glass capillary of 0.1 mm in diameter, and their profile data were recorded in 0.003° increments over the range $5° \leq 2\theta \leq 50°$. Rietveld structural refinements were performed against the SXRD data using the program RIETAN-FP[3, 4]. The split pseudo-Voigt function, which was formulated by Toraya, was employed as a profile function. The weighting R index (R_{wp}), the Bragg R index (R_{I}), and goodness of fit (S) are defined as follows; $R_{\mathrm{wp}} = [\Sigma_{\iota} w_i(y_{io}–y_{ic})^2/\Sigma_{\iota} w_i y_{io}^2]$ and $R_{\mathrm{I}}= \Sigma_{\kappa}|I_{ko}–I_k|/\Sigma_{\kappa} I_{ko}$, where y_{io} and y_{ic} are the observed and calculated intensities, w_{i} is the weighting factor, and I_{ko} and I_k are the observed and calculated integrated intensities. $S = R_{\mathrm{wp}}/R_{\mathrm{exp}}$. $R_{\mathrm{exp}} = [(N–P)/\Sigma_{\iota} w_i y_{io}^2]^{1/2}$, where N is the total number of y_{io} data when the background is refined, and P is the number of adjusted parameters.

2.2.3 Neutron diffraction (NPD)

Neutron powder diffraction is a complementary to synchrotron X-ray powder diffraction method, it is particularly useful for materials with light elements and for magnetic structure analysis. Because of the weak absorption of neutrons, they can generalize information on bulk materials and detect the lattice distortions and defects in a nondestructive way. In addition, since neutrons possess spin ½ which provide the neutrons to interact with unpaired electrons and consequently, neutrons are diffracted by both atomic nuclei and unpaired electrons. In this way, neutron powder diffraction can detect the magnetic structure with priority of any other methods.

The NPD experiments in this thesis were carried out using either the HRPT (High-Resolution Powder Diffractometer for Thermal Neutrons) at PSI (Paul Scherrer Institute)[5] or the high resolution powder diffractometer Echidna at OPAL (Open Pool Australian Lightwater reactor) in ANSTO (Australian Nuclear Science and Technology Organizations)[6], as shown in **Figure 2.3**. The wavelength of the incident neutrons, which were monochromated with a Ge 335, was 1.622 Å. The sample was sealed in a 6 mm diameter vanadium can and set in a cryostat. The NPD data were collected in 0.125° increments over the range of $9° \leq 2\theta \leq 157°$ at several temperatures between 3 to 300 K. Rietveld structural refinements were performed against both NPD data using the programs FullProf[7].

Figure 2.3 (a) HRPT at PSI[5] and **(b)** ECHIDNA at OPAL in ANSTO[6].

2.3 Magnetic properties measurement system (MPMS)

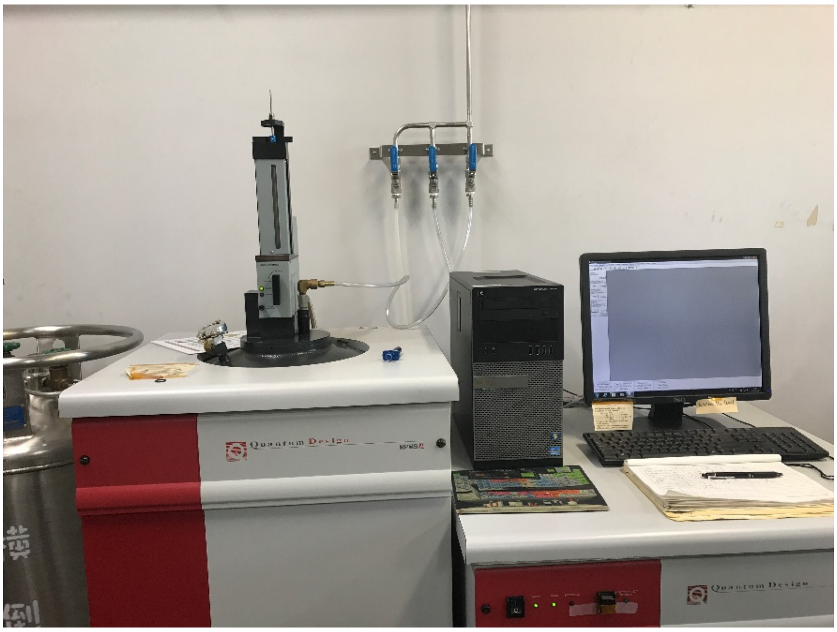

Figure 2.4 Image of the MPMS-XL in NIMS Namiki-site

The magnetic properties of all the samples were measured by using MPMS-7T (Quantum Design) as shown in **Figure 2.4**. The temperature dependent magnetic susceptibilities (χ) and field dependent isothermal magnetizations of all the as prepared samples were measured. The temperature dependent magnetic susceptibilities (χ) were measured under both field cooling (FC) and zero field cooling (ZFC) conditions in a temperature range 2-400 K under an applied magnetic field of 10 kOe. The field dependence isothermal magnetizations were measured between +70 kOe and –70 kOe. The ac susceptibility were measured under 5Oe over the range of 1 Hz to 100 Hz.

2.4 Heat capacity measurement

Heat capacity or thermal capacity is a measurable physical quantity which refers to the energy that is required to heat up or cool down of an object for a certain temperature change. Heat capacity measurements were carried out at zero magnetic field using a relaxation technique with a Physical Property Measurement System (PPMS, Quantum Design), as shown in **Figure 2.5**. A hand-pressed pellet of sample was mounted on an aluminum plate with Apiezon N-Grease for better thermal contact.

Figure 2.5 Image of the PPMS-7T in NIMS Namiki-site

2.5 Diffuse-Reflectance Spectroscopy Measurements

Measurement was carried out at room temperature using a Varian Cary 500 UV-vis-near-IR spectrophotometer equipped with a double-beam photomultiplier tube and a lead sulfide detector. Reflectance measurement of the sample was made relative to poly (tetrafluoroethylene): the reference material was used to establish a baseline, and the absolute reflectivity of a sample was then calculated from that of the reference. Data were collected in the wavelength range 260-3000 nm. The Kubelka-Munk function was used to convert diffuse-reflectance data to absorbance spectra.

2.6 Band calculation

The *ab initio* calculations were performed on the basis of the plane-wave pseudopotential strategy using the computer program VASP (Vienna *Ab Initio* Simulation Package)[8]. The projector-augmented wave approach[9] and the generalized-gradient approximation (GGA) of PBE-type were used[10]. An energy cutoff of 400 eV was utilized, and the lattice parameters and atomic positions were optimized until the residual force was less than 0.02 eV/Å. The *k*-point grid of 16 × 16 × 4 was automatically generated according to the method by Monkhorst and Pack[11]. The density of state and chemical bonding analyses were calculated by the LOBSTER code[12].

2.7 Scanning electron microscope (SEM)

Scanning electron microscopy (SEM) is an electron microscope that uses electron beam to scan the surface of a sample to obtain sample information. It can produce high-resolution three-dimensional images on the surface of the sample. Besides, elemental analysis can also be carried out.

In this thesis, the elemental analysis for the single crystal sample was conducted using a scanning electron microscope (SEM, HITACHI-TM3000) equipped with an energy dispersive

X-ray spectroscopy (EDX) analyser (Oxford Instruments, SwiftED3000). The accelerating voltage was 15 kV.

References in chapter 2

1. Fernández-Sanjulián, J., E. Morán, and M. Ángel Alario-Franco, *Synthesis, stability range and characterization of* $Pr_2Cu_2O_5$. High Pressure Research, 2010. **30**(1), 159-166.

2. Tanaka, M., Y. Katsuya, and A. Yamamoto, *A new large radius imaging plate camera for high-resolution and high-throughput synchrotron x-ray powder diffraction by multiexposure method.* Review of Scientific Instruments, 2008. **79**(7).

3. Izumi, F., H. Asano, H. Murata, and N. Watanabe, *Rietveld analysis of powder patterns obtained by TOF neutron diffraction using cold neutron sources.* Journal of Applied Crystallography, 1987. **20**(5), 411-418.

4. Izumi, F. and K. Momma, *Three-Dimensional Visualization in Powder Diffraction.* Solid State Phenomena, 2007. **130**, 15-20.

5. Fischer, P., G. Frey, M. Koch, M. Könnecke, V. Pomjakushin, J. Schefer, R. Thut, N. Schlumpf, R. Bürge, U. Greuter, S. Bondt, and E. Berruyer, *High-resolution powder diffractometer HRPT for thermal neutrons at SINQ.* Physica B: Condensed Matter, 2000. **276–278**, 146-147.

6. Liss, K.-D., B. Hunter, M. Hagen, T. Noakes, and S. Kennedy, *Echidna—the new high-resolution powder diffractometer being built at OPAL.* Physica B: Condensed Matter, 2006. **385–386, Part 2**, 1010-1012.

7. Izumi, F. and Y. Kawamura, *Three-dimensional visualization of nuclear densities by MEM analysis from time-of-flight neutron powder diffraction data.* Bunseki Kagaku, 2006. **55**(6), 391-395.

8. Kresse, G., *Ab-Initio Molecular-Dynamics for Liquid-Metals.* Journal of Non-Crystalline

Solids, 1995. **193**, 222-229.

9. Blöchl, P.E., *Projector augmented-wave method.* Physical Review B, 1994. **50**(24), 17953-17979.

10. Perdew, J.P., J.A. Chevary, S.H. Vosko, K.A. Jackson, M.R. Pederson, D.J. Singh, and C. Fiolhais, *Atoms, Molecules, Solids, and Surfaces - Applications of the Generalized Gradient Approximation for Exchange and Correlation.* Physical Review B, 1992. **46**(11), 6671-6687.

11. Monkhorst, H.J. and J.D. Pack, *Special points for Brillouin-zone integrations.* Physical Review B, 1976. **13**(12), 5188.

12. Tnak, R.W., O. Jepsen, Burkhardt， A., and O.K. Anderson, *The Stuttgart TB-LMTO-ASA program (v47)*. 1998, MPI-fu ¨ rFestko ¨ rperforschung.

Chapter 3 High-Pressure Synthesis, Crystal Structure, and Magnetic Properties of Sr_2MnO_3F

3.1 Introduction

Perovskite-based manganese oxides expressed as AMnO$_3$ (A = alkaline earth and lanthanide metals) have been extensively studied because of their interesting physical properties, for example, metal-insulator transition, colossal magnetoresistance (CMR), spin-driven ferroelectricity, and charge/orbital ordering[1-6]. These phenomena are very sensitive to the covalency between manganese and oxide ions and the Mn-O-Mn bond angle, which are directly linked to super-exchange interaction, charge transfer energy, and double exchange interaction[7-9]. A rich variety of electronic phases involving strong correlation among spin, charge, and orbital degrees of freedom has been revealed by fine tuning of chemical compositions at cation sites[7, 9, 10].

In comparison with a great deal of studies on cation substitution, the effects of anion substitution on physical properties of manganese perovskite compounds have been investigated to a less extent. In general, the stability of the metal-oxygen bond is high compared with the case of other anions, which make it difficult to confine mixed anions to anion sublattices under conventional high-temperature conditions. Nevertheless, much effort made to develop kinetic reactions opens up doors for unprecedented mixed anion phases, for example, metal-hydride reduction giving $Sr_{n+1}V_nO_{2n+1}H_n$(n = 1, 2, and 3)[11] and $BaTiO_{0.6}H_{0.4}$[12] and reductive ammonolysis to produce $NdVO_2N$[13] and $EuNbO_2N$[14]. Oxyfluoride perovskites have been most vastly explored among mixed anion systems, especially since the discovery of a superconducting layered copper oxyfluoride $Sr_2CuO_2F_{2+\delta}$[15]. The low-temperature fluorination generally involves a simple fluorine insertion into interstitial sites such as oxygen vacancy sites, a substitution of fluorine for oxygen, or both[16]. For manganese, the fluorination of the oxygen deficient phases $Sr_2Mn_2O_5$ and Sr_2MnGaO_5 using XeF_2 as a fluorinating agent results in $Sr_2Mn_2O_{5-x}F_{1+x}$ and $Sr_2MnGaO_{4.78}F_{1.22}$ with Mn^{3+}/Mn^{4+} valence states through the filling of the oxygen vacancy sites with fluorine and the partial substitution of fluorine for oxygen, as shown in **Figure 3.1(a)**[17, 18]. Of layered manganese oxides adopting the Ruddlesden-Popper (RP) type perovskite structure with general formula $(AO)(AMnO_3)_n$, $LaSrMnO_4$ (n=1) and $Ln_{1.2}Sr_{1.8}Mn_2O_7$(n = 2) accommodate fluorine in the interstitial sites of the (La/Sr)O rock-salt layers, not in anion sites of the perovskite block layers, giving $LaSrMnO_4F_y$ (y = 1, 1.7, and 2) and $Ln_{1.2}Sr_{1.8}Mn_2O_7F_y$($y$ = 1 and 2; Ln = La, Pr, Nd, Sm, Eu, and Gd)[19-22], as shown in **Figure 3.1(b)**. On the other hand, the oxygen deficient phase $Sr_3Mn_2O_6$, which has pseudo-square and -hexagonal tunnels composed of corner-sharing MnO_5 square pyramids, exhibits a step-wise fluorination: the fluorine atoms occupy the oxygen vacancies at the equatorial sites of MnO_5 square pyramids, then interstitial sites in the rock-salt layers, with varying the fluorine content in $Sr_3Mn_2O_6F_y$ (y = 1, 2, and 3)[23]. Thus, the fluorination of the manganese oxide described above successfully resulted in the modification of coordination environments and valence states for manganese; however, these fluorinated compounds did not exhibit either a magnetic phase transition, metallic conductivity or magnetoresistance.

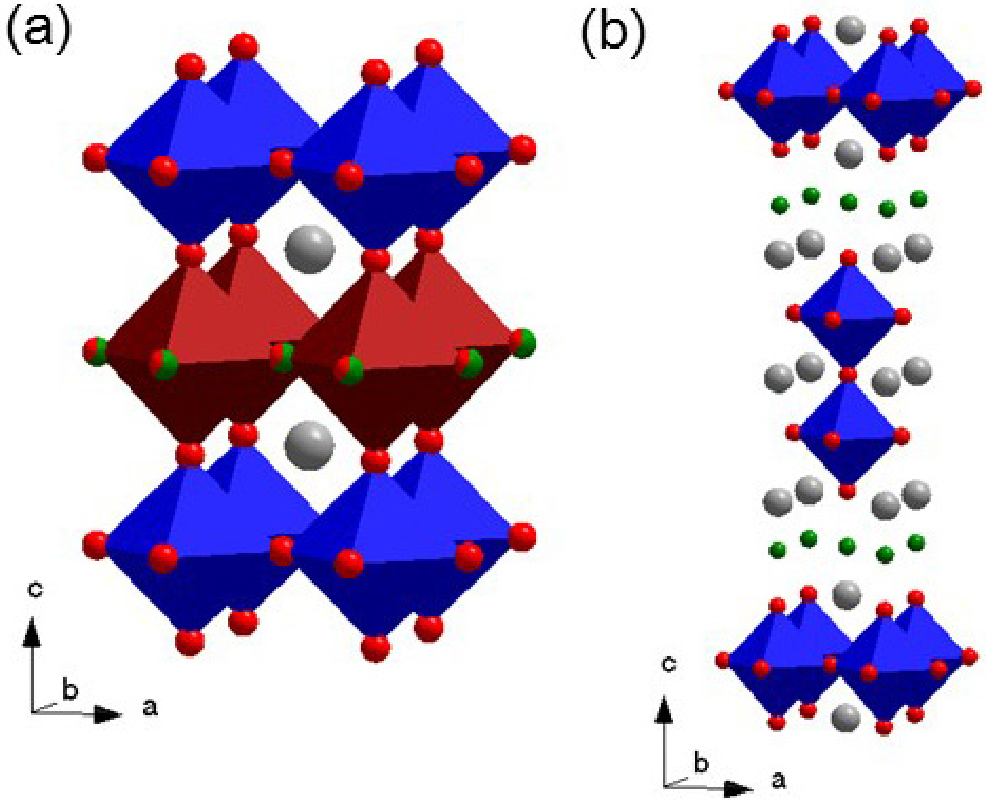

Figure 3.1 Crystal structures of **(a)** $Sr_2MnGaO_{4.78}F_{1.22}$ and **(b)** $La_{1.2}Sr_{1.8}Mn_2O_7F_2$. MnO_6 and $Ga(O, F)_6$ are octahedra.Gray, red, and green spheres represent Sr/La, O, and F atoms, respectively.

Another useful approach toward mixed anion compounds is the high-pressure method, by which two new perovskite manganese compounds, i.e. $PbMnO_2F$[24] and $MnTaO_2N$[25] were obtained. Recently, our research group have successfully extended to RP-type layered oxyhalide series by using this technique. Sr_2NiO_3X (X = F and Cl) with the high oxidation state of Ni^{3+} were synthesized at 6 GPa and 1500°C for X = F and 3 GPa and 1300°C for X = Cl[26]. The nickel oxyhalides crystallize in the so-called K_2NiF_4 type structure belonging to the $n = 1$ RP, but have highly distorted octahedra around the nickel centers with the fluorine (chlorine) atom being disordered (ordered) at the apical sites with one apical oxygen atom (see **Figure 3.1 (a)** and **(b)**). Specifically, the nickel cation forms strong covalent bonds with five surrounding oxygen anions and a significantly weak bond with the halogen anion, leading to the low-spin configuration of $S = 1/2$. Thus, the nickel-centered coordination can be effectively viewed as a square pyramid rather than an octahedron. In addition to the nickel oxyhalides, Sr_2CoO_3F was synthesized under high-pressure condition[27, 28] in contrast to Sr_2CoO_3Cl that can be synthesized at ambient pressure[29, 30]. These cobalt oxyhalides were found to exhibit the O/X-site ordered patterns and coordination environments similar to those of Sr_2NiO_3X.

So far, several layered oxyhalide compounds expressed as A_2BO_3X (A = alkaline and alkali earth metal; B = In, Sc, Nb, Co, and Fe, and Ni, X = F and Cl) have been reported[26, 31-35]. To our knowledge, however, the manganese oxyfluoride, namely, A_2MnO_3F, has never been obtained. Actually, Hagenmuller et al. synthesized $Ca_2MnO_{4-y}F_y$ by conventional solid state reaction, but the fluorine content range in which the homogeneous sample could be obtained, was limited to $0 \leq y \leq 0.3$[36]. On the other hand, Greaves et al. attempted fluorine insertion into $Sr_2MnO_{3.5+x}$with a complex oxygen vacancy ordered structure, using fluorine gas as a fluorinating agent[23]. But it resulted in inhomogeneous phases corresponding to an average chemical composition $Sr_2MnO_{3.53}F_{0.39}$, which consists of the slightly fluorinated phase maintaining the $Sr_2MnO_{3.5+x}$ structure and the highly fluorinated phase with a K_2NiF_4 structure[24].

In this chapter, we have demonstrated the successful synthesis of Sr_2MnO_3F by high-pressure and high-temperature reaction. The product adopts the K_2NiF_4 type structure with octahedral coordination around Mn and with O/F site disordered at the apical sites. An antiferromagnetic phase transition takes place at 133 K., which is the first observation of a long-range magnetic order among perovskite based manganese oxyfluoride compounds.

3.2 Experimental details

Sr_2MnO_3F was prepared by solid-state reaction under high pressure and high temperature. A stoichiometric amount of SrF_2 (99.9%, Rare Metallic Co., Ltd.), SrO prepared by heating

$SrCO_3$ in flowing O_2 gas, and Mn_2O_3 prepared by heating $MnCO_3$ at 800 °C overnight was thoroughly ground in an agate mortar in an argon-filled glovebox, sealed in a platinum capsule, and then set in a high-pressure cell. This was then heated to temperatures ranging from 1700 to 2000 °C at 6 GPa using a belt-type high-pressure apparatus. After heating for the prerequisite time, the sample was cooled to 1200 °C for 30 min and then quenched to room temperature by switching off the heater before pressure release. Of the reaction conditions we examined, we found that heating at 1800 °C for 45 min gave the best sample quality.

3.3 Results and discussion

3.3.1 Synthesis and Structure

Figure 3.2 shows the SXRD profile collected from Sr_2MnO_3F that was prepared by heating at 6 GPa and 1800 °C and subsequently slowly cooled down to 1200°C while keeping the pressure. The main reflections could be readily indexed on a simple body-centered tetragonal cell in the space group $I4/mmm$, which are common to related layered oxyfluorides such as Sr_2NiO_3F[26] and Sr_2CoO_3F[16, 27] with $n = 1$ RP structure. Some very tiny and broad peaks were visible which can be characterized as impurity phases such as SrO, SrF_2 and MnO_2, as seen in **Figure 3.3**. The lattice parameters calculated on Sr_2MnO_3F are $a = 3.79009(1)$ Å and $c = 13.28974(6)$ Å. The c axis length significantly expands compared with those of Sr_2MnO_4 ($a = 3.787$ Å and $c = 12.496$ Å)[37] and $Sr_2MnO_{3.53}F_{0.39}$ ($a = 3.82069(5)$ Å and $c = 12.6309(4)$ Å)[23], while the a axis length remains almost unchanged. In contrast, both of the lattice parameters of the product are comparable to those of the isovalent compound $LaSrMnO_4$ ($a = 3.786$ Å and $c = 13.163$ Å) with a Janh-Teller active Mn^{3+}, which strongly suggests that the manganese center in the oxyfluoride phase is subject to the Jahn-Teller effect, too.

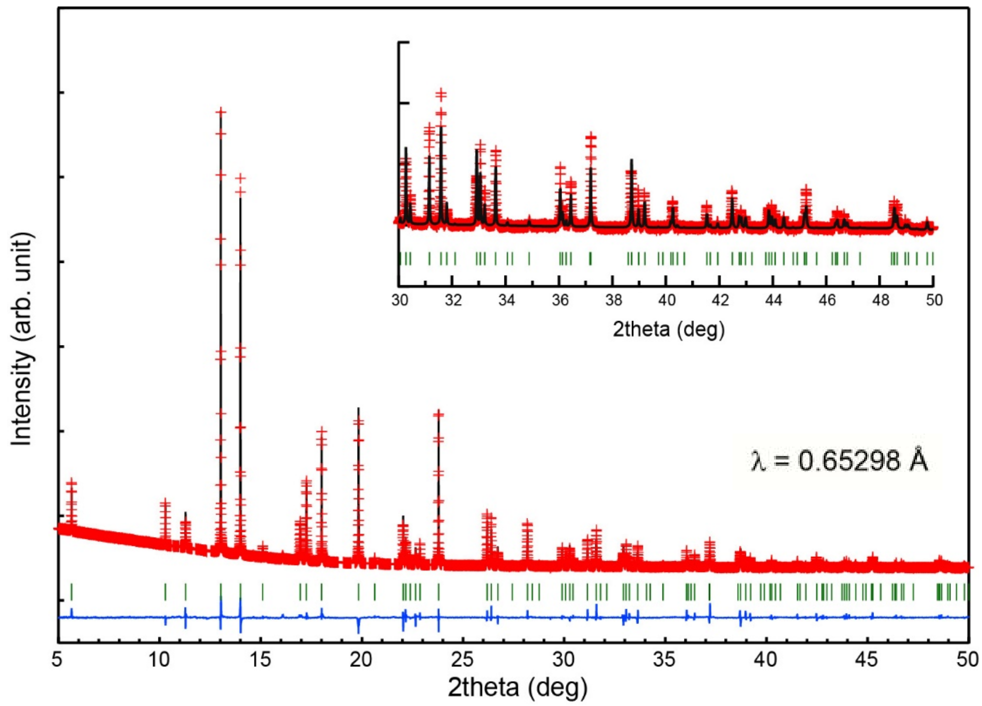

Figure 3.2 Synchrotron XRD patterns for Sr_2MnO_3F measured at room temperature. Obtained, calculated and difference are presented with cross marks, upper and bottom solid lines, respectively. The vertical lines mark represent the Bragg peak positions.

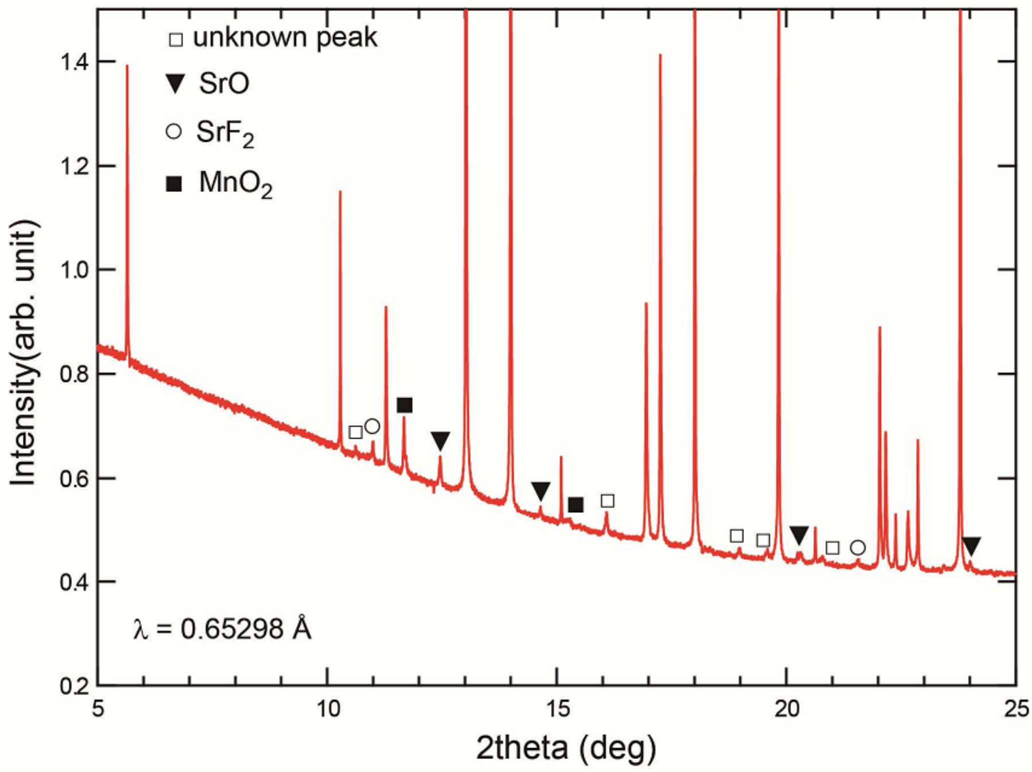

Figure 3.3 Synchrotron X-ray diffraction patterns collected from Sr_2MnO_3F at room

temperature. SrO, SrF_2, and MnO_2 were detected as minor phases while several peaks could not be characterized.

Determination of fluorine site in the anion lattices is of a major concern in oxyfluoride materials because X-ray and neutron scattering cannot distinguish between O and F atoms[27, 28, 38, 39]. However, related layered oxyhalides with the anion site ordered at the apical sites are generally subject to symmetry lowering. For example, Sr_2FeO_3F[40]and Sr_2NiO_3Cl[26] adopt the space group *P*4*/nmm*. There was no evidence for O/F site order in the present sample, a model based on the Sr_2MnO_4-type structure where the O/F atoms are randomly distributed over the apical sites 4e (0 0 *z*) was initially examined by Rietveld structural refinement. The site occupancies (*g*) of Sr, Mn, and the equatorial oxygen (O_{eq}) were fixed at unity while the oxygen (O_{ap}) and fluorine occupancies at the apical site were 50%, respectively, according to the nominal composition. All the atomic coordinates and isotropic displacement parameters (B_{iso}) of O_{ap}/F atoms were constrained to the same values during the refinement. The refinement gave a satisfactory result with reliable factors, R_{wp} = 2.211% and R_B = 3.96%. The relatively large atomic displacement parameters of O_{ap}/F sites (B_{iso} = 1.88(8) Å^2) is attributable to a statistical 50:50 O_{ap}/F mixture at the 4e site, as in Sr_2NiO_3F[26]. In fact, the introduction of site deficiency or splitting to more general positions such as 16*m* (*x*, *x*, *z*) did not improve the refinements. Details of the refined crystallographic data are tabulated in **Table 3.1**. The crystal structure is illustrated in **Figure 3.5(c)** with the local coordination environment around Sr and Mn atoms in **Figure 3.4**.

Table 3.1 Crystallographic Parameters Refined from SXRD Data Collected from Sr_2MnO_3F at Room Temperature.

Atom	Site	g^b	x	y	z	B_{iso}/ Å ^{2}
Sr	4*e*	1	0	0	0.36036(5)	0.823(19)
Mn	2*a*	1	0	0	0	0.97(3)
O_{eq}	4*c*	1	0	0.5	0	0.52(8)
O_{aq}/F	4*e*	0.5/0.5	0	0	0.1722(2)	1.88(8)

The space group is *I4/mmm* (no. 139), a = 3.79009(1) Å, c = 13.28974(6) Å. R indices are R_{wp} = 2.211%, R_p = 1.135%, R_B = 3.96%, and R_F = 2.025%.

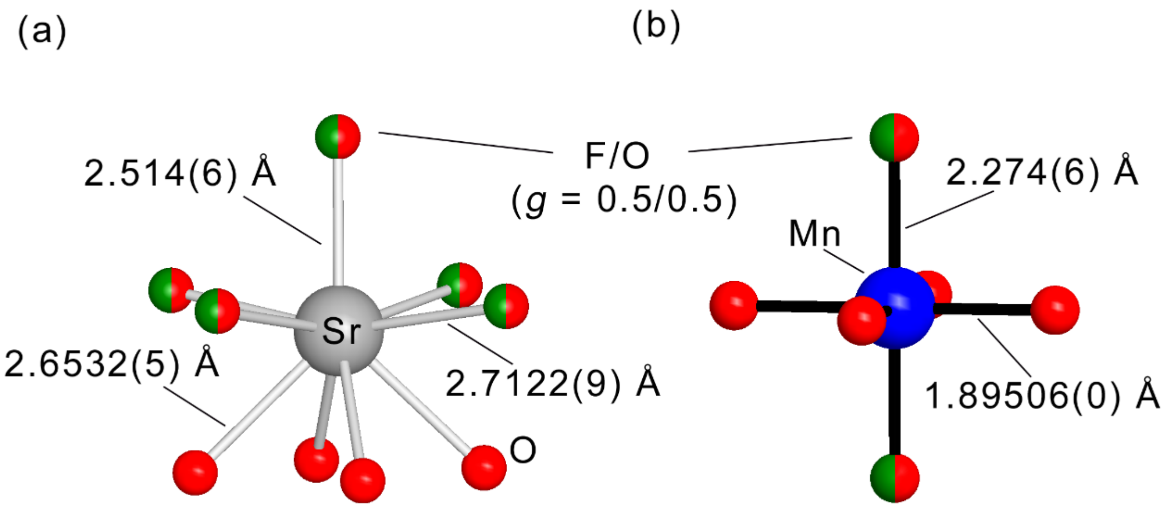

Figure 3.4 Local coordination environment around Sr and Mn atoms for Sr_2MnO_3F.

Bond-valence-sum (BVS) calculation is a useful technique to compare possible distribution patterns of mixed anions on the basis of refined crystallographic data[41]. The BVS values for Sr, Mn and O_{eq} using the obtained crystallographic data were 1.95, 3.22, and 2.33, respectively. In addition, the calculation of BVS for O_{ap}/F was 1.23 on average. These results are consistent with values expected from the nominal composition. In contrast, a model where one fluoride ion occupies the equatorial sites at random with three oxide ions resulted in a significantly lower value of 1.39 for O_{ap} than that expected from full occupation of the apical sites by oxide ions. Therefore, the model with random distribution of both oxide and fluoride ions at the apical sites describe better the structure of Sr_2MnO_3F.

3.3.2 Coordination geometry of the Mn center

The structural refinements revealed that the manganese cation is located at the center position of an octahedron comprising of four oxide ions at the equatorial sites and oxide and fluoride ions at the apical sites. The Mn-(O_{ap}/F) and Mn-O_{eq} bond lengths are 2.274(6) Å and 1.89506(0) Å, respectively, thus the bond ratio of the former to the latter is 1.20. The anisotropic bond lengths indicate that the Mn centered octahedron is heavily distorted along the *c* axis because of the Jahn-Teller effect, which is commonly observed in trivalent Mn cations. The bond ratio for Sr_2MnO_3F is comparable to 1.20 of the Mn-O_{ap}/Mn-O_{eq} bond ratio for the $n = 1$ RP $LaSrMnO_4$ with isoelectronic manganese cation[42].

The coordination environment around the Mn center is unique compared with those in related oxyfluoride compounds. For example, Sr_2MO_3F (M = Fe, Co, and Ni) exhibits a square-pyramid MO_5 which is loosely linked by a fluoride ion with the apical O/F anions being ordered for M = Fe and disordered for Co and Ni, as shown in **Figure. 5(a)** and **(b)**[26-30]. Sr_2ScO_3F[35] and K_2NbO_3F[33] with the non-magnetic transition metals apparently take a coordination geometry of the metal center similar to that of the Mn cation in Sr_2MnO_3F: the ScO_5F or TiO_5F octahedron with the O/F anions disordered at the apical sites. However, the ratio of the apical bond to the equatorial bond is 1.075 Sr_2ScO_3F and 1.043 for K_2TiO_3F, indicating that the bond anisotropy is much smaller than for Sr_2MnO_3F. The slight elongation of the octahedra is attributable to 2nd Jahn-Teller effect[43, 44]. The influence of the Jahn-Teller distortion in Mn^{3+} ion on the phonon energy is manifested by comparing the heat capacity with that of Sr_2ScO_3F, as will be discussed later.

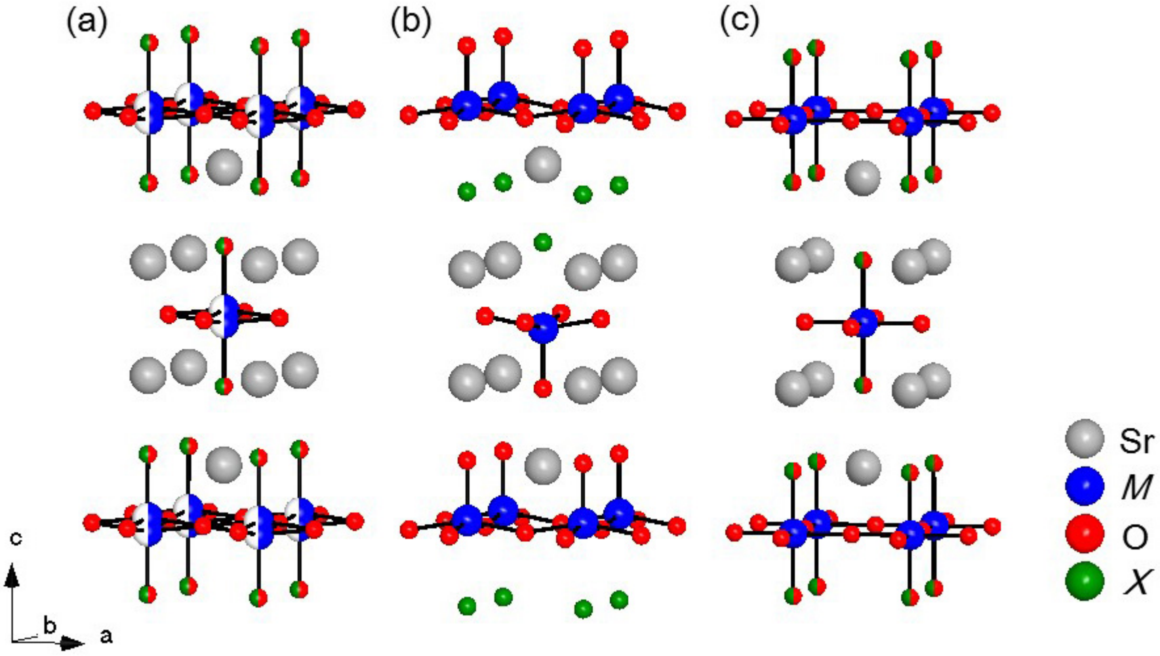

Figure 3.5 Comparison among metal centered coordination and anion-ordered patterns in layered oxyhalide system with general formula Sr_2MO_3X (M = transition metal, X = halogen). **(a)** Square pyramidal coordination with anion disorder, **(b)** square pyramidal coordination with anion order, and (c) octahedral coordination with anion disorder. Each types of structural features are adopted by Sr_2MO_3F (M = Co and Ni), Sr_2MO_3Cl (M = Mn, Co, and Ni), and Sr_2MO_3F (M = Sc and Mn), from left to right.

It is interesting to compare the structure of Sr_2MnO_3F with the manganese oxychloride analogue, Sr_2MnO_3Cl, with a square-pyramidal coordination around Mn and with O/Cl order at the apical sites[30, 34]. The reduction in the coordination number for the manganese oxychloride results from the Coulomb repulsion between oxide and chloride ions or steric effect by chloride ion much bigger in size than oxide ion (r_{O2-} = 1.40 Å and r_{Cl-} = 1.81 Å)[45]. On the other hand, there are two important factors to cause anion disorder, as discussed previously for related layered oxyfluorides with non-d^0 based transition metals[26-28, 38]. One is the relative size of halide and oxide ions: the ionic radius of oxide is close to that of fluoride (r_{F-}= 1.33 Å)[45], but significantly smaller than that of chloride. The other is high reaction temperature associated with entropic effects, which favors a random distribution of mixed anions. The reaction temperatures required for the syntheses of Sr_2CoO_3F, Sr_2NiO_3F, and Sr_2MnO_3F with O/F site disordered are 1900, 1500, and 1800°C, respectively, which are much higher than those for related oxyfluorides synthesized by conventional solid state reaction, for example, 900°C for Sr_2FeO_3F[40] and 1050 °C for Sr_2ScO_3F[35]. The anion-site ordering patterns have yet to be controlled in Sr_2MO_3F (M = Co, Ni, and Mn), but we recently observed a partial O/F site disorder in Sr_2FeO_3F single crystals synthesized at 1800°C and 6 GPa, which is in contrast to the full anion-ordered Sr_2FeO_3F prepared by conventional solid state reaction[46]. The high-pressure effect may be ruled out for the anion-site disordering, because the density of the anion-disordered Sr_2FeO_3F was lower than that of the ordered one.

3.3.3 Magnetic susceptibility and heat capacity

Figure 3.6 shows the temperature dependence of the magnetic susceptibility χ (= M/H) and its inverse in magnetic field H = 1kOe for Sr_2MnO_3F. The $\chi(T)$ data showed a smooth increase with decreasing temperature, following the Curie-Weiss law, $1/\chi = (T - \theta)/C$, in the range of $350 < T < 400$ K, where C and θ stand for the Curie constant and Weiss constant, respectively. The large negative value of θ = -526(23) K suggests that a strong antiferromagnetic interaction is present in the MnO_2 plane. The estimated value of the Curie constant was 3.90(10) (emu K)/mol, which is comparable to those of Sr_2MnO_3Cl and $LaSr_{1-x}Ba_xMnO_4$with a trivalent manganese cation[29, 30, 47]. On further cooling from 350 K, the susceptibility curve started to deviate from the Curie-Weiss law because of short-range spin correlation in the MnO_2 plane and exhibited a broad maximum at T_{max} = 178 K. This behavior is typically seen in low-dimensional antiferromagnets. In addition, we observed a clear inflection point associated with an antiferromagnetic ordering at T_N = 133 K. The Curie tail below 50 K should be due to free spins of impurities. It is noting that the T_{max} and θ values for the manganese oxyfluoride are much larger than T_{max} = 95 K and θ = -284 K for the oxychloride counterpart[29, 30], indicating stronger magnetic coupling in the MnO_2 plane in the former. This is attributed to stronger hybridization between Mn and O orbitals on the MnO_2 plane in the oxyfluoride than that in oxychloride with the corrugated Mn-O-Mn bond angle (163.2°) in the basal plane[29, 30]. **Figure 3.7** shows the field dependence of magnetization at 5 K. The *M*(*H*) increased almost linearly in proportion to applied magnetic fields and reached 0.05 μ_B at 50 kOe. No hysteresis was observed as shown in the inset of **Figure 3.7**.

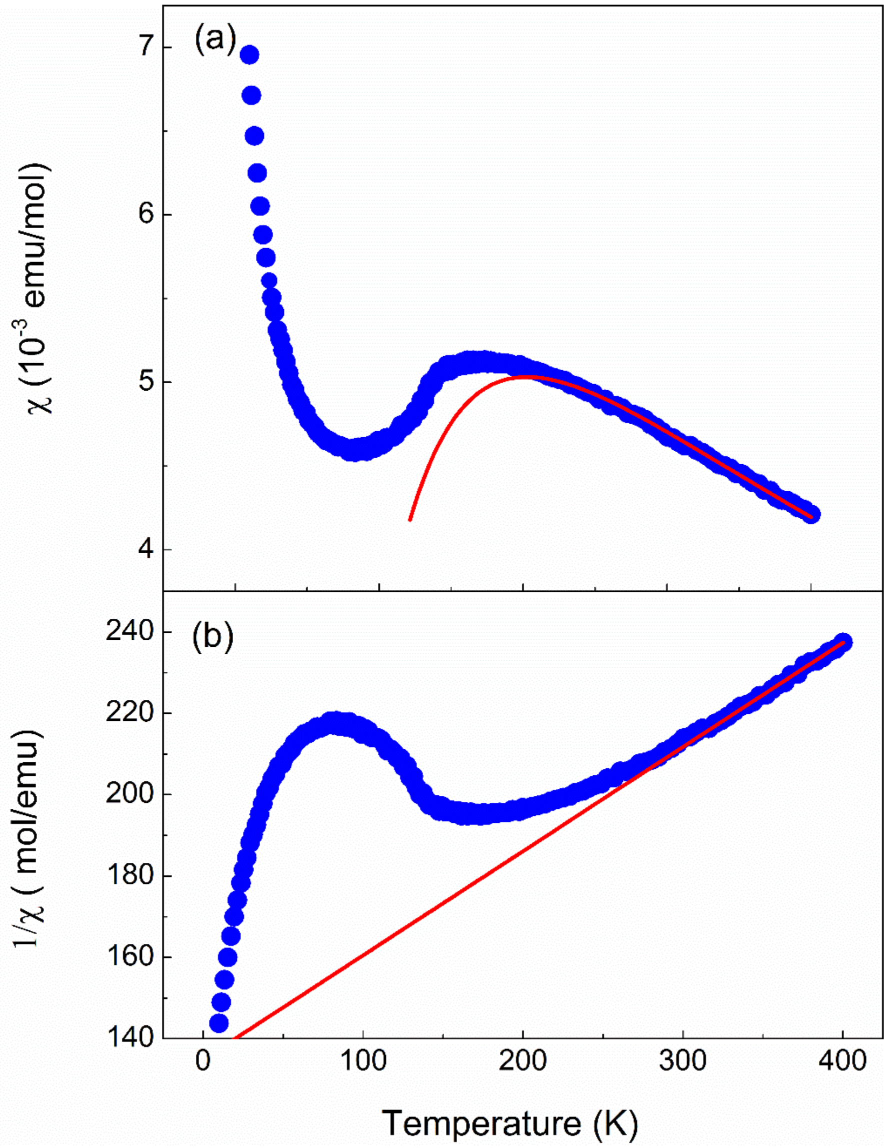

Figure 3.6 (a) The temperature dependence of the magnetic susceptibility at *H*= 0.1 kOe for Sr_2MnO_3F. The red line on the data points between 300 and 400 K is a fit to a $S = 2$ square-lattice Heisenberg antiferromagnetic spin (SLHAS) model obtained by high-temperature series expansion. **(b)** The inverse susceptibility vs *T* plot where the solid lines represent Curie -Weiss fit.

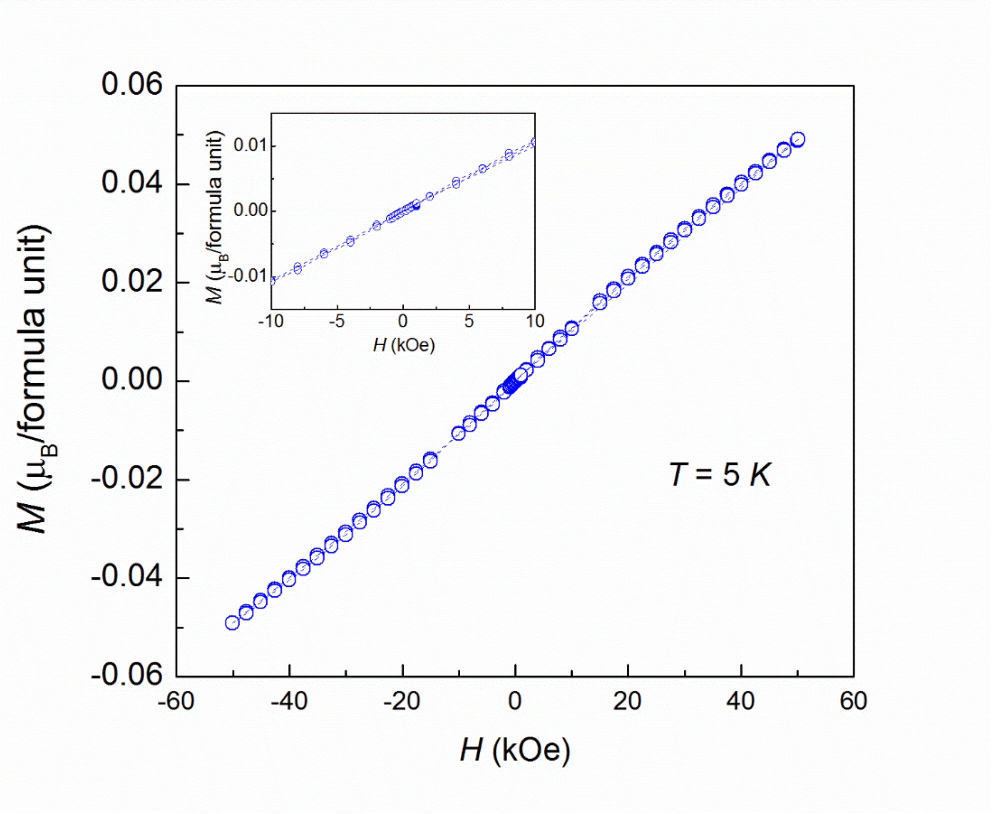

Figure 3.7 Isothermal magnetizations at 5 K for Sr_2MnO_3F. The inset is an expansion of the plots.

The electronic configuration of the Jahn-Teller active Mn^{3+} ion is described as $(d_{xz}, d_{yz})^2(d_{xy})^1(d_{3z^2-r^2})^1(d_{x^2-y^2})^0$. In a square lattice system composed of corner-shared MnO_4 squares, not only the exchange interactions along the edges (J_1) in a MnO_2 square net but also ones along the diagonal direction (J_2) should be considered. However, the magnitude of the J_2 derived mainly from the direct d_{xy}-d_{xy} bond is smaller than that of J_1. Laroochelle et al. estimated $J_1/k_B = 39.7$ K and $J_2/J_1 = 0.11$ on the isoelectronic $LaSrMnO_4$ by neutron scattering technique[48]. We evaluated roughly the exchange coupling constant on Sr_2MnO_3F by employing a high-temperature series expansion for the square-lattice Heisenberg antiferromagnetic spin(SLHAS) model taking only the nearest neighbor interaction into consideration,[45] which is described as follows,

$$\frac{Ng^2 \mu_B{}^2}{\chi J} = 3\xi + \sum_{n=1}^{6} \frac{C_n}{\xi^{n-1}} \qquad (3.1)$$

Where N is the Avogadro constant, J is the nearest neighbor exchange constant, k_B is the Boltzmann constant, $\xi = k_BT/JS(S+1)$, the C_n coefficients are $C_1 = 4$, $C_2 = 1.5$, $C_3 = 0.252$, $C_4 = 0.258$, $C_5 = 0.134$, and $C_6 = 0.015$. As shown in **Figure 3.6(a)**, we obtained a reasonable fit in the range of $120 < T < 400$ K, resulting in $J/k_B = 32.62(2)$ K, which is somewhat smaller than J_1 in $LaSrMnO_4$.

The heat capacity C_p of Sr_2MnO_3F, which was measured between 2 and 250 K in zero magnetic field, is presented in **Figure 3.8**. A λ-type anomaly in the data was detected at around 140 K. This result is consistent with the antiferromagnetic phase transition observed in the $\chi(T)$ curve. To estimate the magnetic entropy of the manganese oxyfluoride, one have to subtract the phonon contribution from the total heat capacity. Simple Debye model as the phonon part is not applicable because the low-dimensional magnetic correlation persists even at high temperatures. Therefore, we employed Sr_2ScO_3F as a non-magnetic reference material, which was prepared by conventional solid-state reaction according to Ref. 35. However, as shown in the inset of **Figure 3.8**, the heat capacity curve of Sr_2ScO_3F crossed that of Sr_2MnO_3F at around 60 K, thus it was not possible to precisely subtract the phonon contribution of the manganese oxyfluoride, especially in the low temperature region. It is likely that these behaviors mainly resulted from different coordination environments between manganese and scandium centers: the driving force of Jahn-Teller effects is by first order for Mn and by 2nd order for Sc[43]. At present, we cannot extract the magnetic contribution from the total heat capacity.

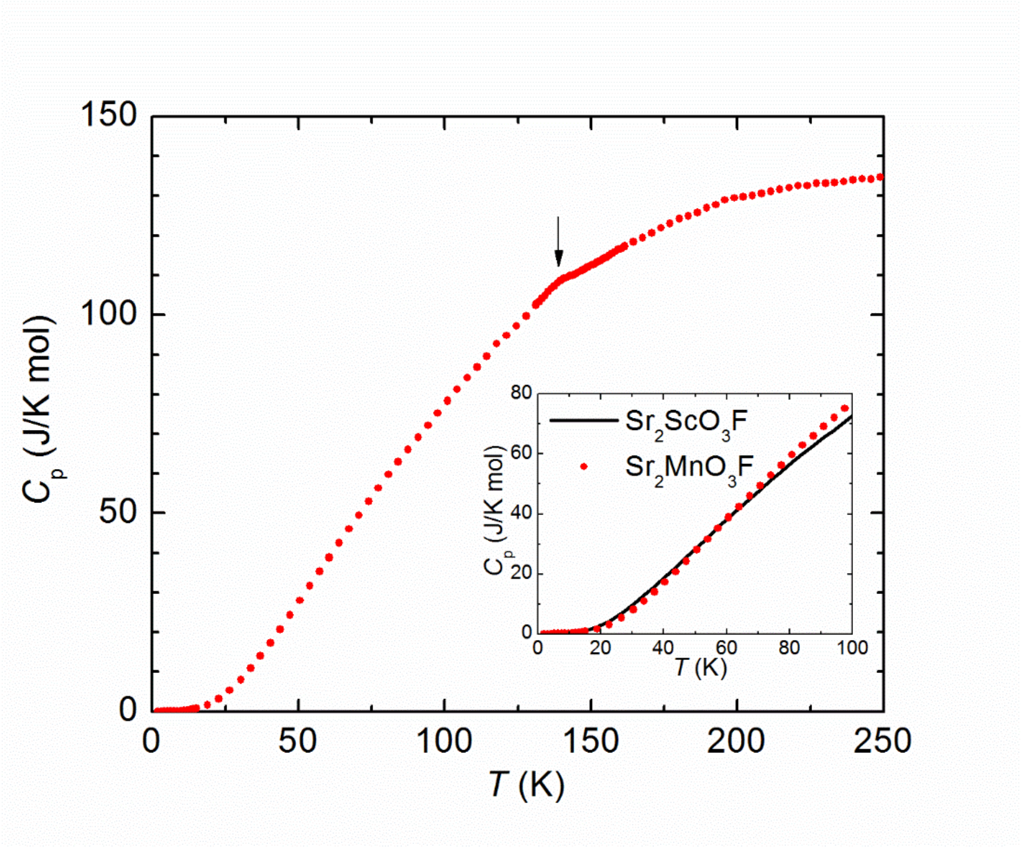

Figure 3.8 Specific heat of Sr_2MnO_3F. The inset shows the comparison with the diamagnetic reference compound Sr_2ScO_3F. The $C_p(T)$ curves crosses at around 50 K, indicating quite different phonon spectra between each other.

Finally, we compare the halogen-site dependence of the magnetic properties of Sr_2MO_3X (M = Mn, Co, and Ni; X = F and Cl). As described above, both of the manganese oxyhalide compounds take a long-range magnetic ordered state at low temperatures, which is remarkably different from the situation in Sr_2NiO_3X. Both of the nickel oxyhalide compounds exhibit a low-spin configuration of Ni^{3+} with $S = 1/2$ as well as similar positive Weiss temperatures close to 20 K[26]. However, the oxyfluoride undergoes a spin-glass like transition at T_{SG} = 11 K in contrast to a long-range magnetic ordering at 33 K for the oxychloride. It has been assumed that the unpaired electron in the nickel cation occupies a d_{xy} orbital, giving antiferromagnetic J_1 and ferromagnetic J_2 on a NiO_4 square. Thus, it is likely that the spin-glassy behavior in the nickel oxyfluoride originates from a bond randomness of J_2 whose magnitude varies depending on the direction of NiO_5 square pyramids or fluorine sites. In light of the situation in the nickel oxyhalides, it is likely that two factors favor the long-range magnetic ordered state in the manganese oxyfluoride with a d_{xy} orbital being half-filled. One is no bond randomness along the diagonal direction unlike the nickel oxyfluoride, since the Mn center sits on the center position of a MnO_5F octahedron. Second is concerning the magnitude and sign of J_2. If J_2 as well as J_1 is antiferromagnetic, the two magnetic interactions are competing between each other: spin frustration which suppresses a long-range magnetic order occurs and a novel quantum spin liquid state is theoretically predicted at $J_2/J_1 \approx 1/2$[49, 50]. Given the small value of $J_2/J_1 = 0.11$ for $LaSrMnO_4$, the J_2 or spin frustration in Sr_2MnO_3F would be quite weak, too. This is actually consistent with the magnetic ordering observed in the manganese oxyfluoride. ForSr_2CoO_3X (X = F and Cl) with square-pyramidal coordination, the d_{xy} orbital is fully occupied and magnetically non-active against O/X site ordered patterns[27, 28, 34, 51, 52]. Therefore, it is reasonable that both compounds exhibit antiferromagnetic ordered states.

3.4 Summary of Chapter 3

In this chapter, we have demonstrated the high-pressure synthesis of another member of layered oxyfluoride family, Sr_2MnO_3F, at 6 GPa and 1800 °C. The manganese oxyfluoride exhibits unique structural features that have never been observed in any other related layered oxyhalides: the coexistence of anion disorder between O and F at the apical sites and the octahedral coordination subject to the 1st order Jahn-Teller effect. The MnO_2 planes separated by non-magnetic Sr(O/F) rock-salt layers result in low-dimensional magnetic correlations with $T_N = 133$ K, which is totally different from paramagnetic behaviors observed in known RP type layered manganese oxyfluorides.

References in Chapter 3

1. Ishiwata, S., Y. Tokunaga, Y. Taguchi, and Y. Tokura, *High-Pressure Hydrothermal Crystal Growth and Multiferroic Properties of a Perovskite* $YMnO_3$. Journal of the American Chemical Society, 2011. **133**(35), 13818-13820.

2. Kimura, T., T. Goto, H. Shintani, K. Ishizaka, T. Arima, and Y. Tokura, *Magnetic control of ferroelectric polarization.* Nature, 2003. **426**(6962), 55-58.

3. Urushibara, A., Y. Moritomo, T. Arima, A. Asamitsu, G. Kido, and Y. Tokura, *Insulator-Metal Transition and Giant Magnetoresistance in* $La_{1-x}Sr_xMnO_3$. Physical Review B, 1995. **51**(20), 14103-14109.

4. Izumi, F., H. Asano, H. Murata, and N. Watanabe, *Rietveld analysis of powder patterns obtained by TOF neutron diffraction using cold neutron sources.* Journal of Applied Crystallography, 1987. **20**(5), 411-418.

5. Tanaka, M., Y. Katsuya, and A. Yamamoto, *A new large radius imaging plate camera for high-resolution and high-throughput synchrotron x-ray powder diffraction by multiexposure method.* Review of Scientific Instruments, 2008. **79**(7).

6. Jonker, G.H., *Semiconducting Properties of Mixed Crystals with Perovskite Structure.* Physica, 1954. **20**(11), 1118-1122.

7. Imada, M., A. Fujimori, and Y. Tokura, *Metal-insulator transitions.* Reviews of Modern Physics, 1998. **70**(4), 1039-1263.

8. Millis, A.J., R. Mueller, and B.I. Shraiman, *Fermi-liquid-to-polaron crossover .2. Double exchange and the physics of colossal magnetoresistance.* Physical Review B, 1996. **54**(8), 5405-5417.

9. Salamon, M.B. and M. Jaime, *The physics of manganites: Structure and transport.* Reviews of Modern Physics, 2001. **73**(3), 583-628.

10. Nakajima, T., H. Yshizawa, and Y. Ueda, *A-site randomness effect on structural and physical properties of ba-based perovskite manganites.* Journal of the Physical Society of Japan, 2004. **73**(8), 2283-2291.

11. Romero, F.D., A. Leach, J.S. Moller, F. Foronda, S.J. Blundell, and M.A. Hayward, *Strontium Vanadium Oxide-Hydrides: "Square-Planar" Two-Electron Phases.* Angewandte Chemie-International Edition, 2014. **53**(29), 7556-7559.

12. Sakaguchi, T., Y. Kobayashi, T. Yajima, M. Ohkura, C. Tassel, F. Takeiri, S. Mitsuoka, H. Ohkubo, T. Yamamoto, J.E. Kim, N. Tsuji, A. Fujihara, Y. Matsushita, J. Hester, M. Avdeev, K. Ohoyama, and H. Kageyama, *Oxyhydrides of (Ca,Sr,Ba)*TiO_3 *Perovskite Solid Solutions.* Inorganic Chemistry, 2012. **51**(21), 11371-11376.

13. Oro-Sole, J., L. Clark, W. Bonin, J.P. Attfield, and A. Fuertes, *Anion-ordered chains in a d(1) perovskite oxynitride:* $NdVO_2N$. Chemical Communications, 2013. **49**(24), 2430-2432.

14. Jorge, A.B., J. Oro-Sole, A.M. Bea, N. Mufti, T.T.M. Palstra, J.A. Rodgers, J.P. Attfield, and A. Fuertes, *Large coupled magnetoresponses in* $EuNbO_2N$. Journal of the American Chemical Society, 2008. **130**(38), 12572-12573.

15. Almamouri, M., P.P. Edwards, C. Greaves, and M. Slaski, *Synthesis and Superconducting Properties of the Strontium Copper Oxyfluoride* $Sr_2CuO_2F_{2+\delta}$. Nature, 1994. **369**(6479), 382-384.

16. Tsujimoto, Y., K. Yamaura, and E. Takayama-Muromachi, *Oxyfluoride Chemistry of Layered Perovskite Compounds.* Applied Sciences-Basel, 2012. **2**(1), 206-219.

17. Lobanov, M.V., A.M. Abakumov, A.V. Sidorova, M.G. Rozova, O.G. D'yachenko, E.V. Antipov, J. Hadermann, and G. Van Tendeloo, *Synthesis and investigation of novel Mn-based oxyfluoride* $Sr_2Mn_2O_{5-x}F_{1+x}$. Solid State Sciences, 2002. **4**(1), 19-22.

18. Alekseeva, A.M., A.M. Abakumov, M.G. Rozova, E.V. Antipov, and J. Hadermann, *Synthesis and crystal structure of the* $Sr_2MnGa(O,F)_6$ *oxyfluorides.* Journal of Solid State Chemistry, 2004. **177**(3), 731-738.

19. Aikens, L.D., R.K. Li, and C. Greaves, *The synthesis and structure of a new oxide fluoride,* $LaSrMnO_4F$*, with staged fluorine insertion.* Chemical Communications, 2000(21), 2129-2130.

20. Aikens, L.D., L.J. Gillie, R.K. Li, and C. Greaves, *Staged fluorine insertion into manganese oxides with Ruddlesden-Popper structures:* $LaSrMnO_4F$ *and* $La_{1.2}Sr_{1.8}Mn_2O_7F$*.* Journal of Materials Chemistry, 2002. **12**(2), 264-267.

21. Sivakumar, T. and J.B. Wiley, *Topotactic route for new layered perovskite oxides containing fluorine:* $Ln_{1.2}Sr_{1.8}Mn_2O_7F_2$ *(Ln = Pr, Nd, Sm, Eu, and Gd).* Materials Research Bulletin, 2009. **44**(1), 74-77.

22. Bhaskar, A., C.S. Sheu, and C.J. Liu, *Electrical properties of fluorine-intercalated layered manganite:* $La_{1.4}Sr_{1.6}Mn_2O_7F_2$. Journal of Alloys and Compounds, 2015. **623**, 324-327.

23. Sullivan, E., L.J. Gillie, J. Hadermann, and C. Greaves, *Fluorine intercalation in the n=1 and n=2 layered manganites* $Sr_2MnO_{3.5+x}$ *and* $Sr_3Mn_2O_6$*.* Materials Research Bulletin, 2013. **48**(4), 1598-1605.

24. Katsumata, T., M. Nakashima, Y. Inaguma, and T. Tsurui, *Synthesis of New Perovskite-Type Oxyfluoride,* $PbMnO_2F$*.* Bulletin of the Chemical Society of Japan, 2012. **85**(3), 397-399.

25. Tassel, C., Y. Kuno, Y. Goto, T. Yamamoto, C.M. Brown, J. Hester, K. Fujita, M. Higashi, R. Abe, K. Tanaka, Y. Kobayashi, and H. Kageyama, $MnTaO_2N$*: Polar* $LiNbO_3$*-type Oxynitride with a Helical Spin Order.* Angewandte Chemie-International Edition, 2015. **54**(2), 516-521.

26. Tsujimoto, Y., K. Yamaura, and T. Uchikoshi, *Extended Ni(III) Oxyhalide Perovskite Derivatives:* Sr_2NiO_3X *(X = F, Cl).* Inorganic Chemistry, 2013. **52**(17), 10211-10216.

27. Tsujimoto, Y., J.J. Li, K. Yamaura, Y. Matsushita, Y. Katsuya, M. Tanaka, Y. Shirako, M. Akaogi, and E. Takayama-Muromachi, *New layered cobalt oxyfluoride,* Sr_2CoO_3F*.* Chemical Communications, 2011. **47**(11), 3263-3265.

28. Tsujimoto, Y., C.I. Sathish, K.P. Hong, K. Oka, M. Azuma, Y.F. Guo, Y. Matsushita, K. Yamaura, and E. Takayama-Muromachi, *Crystal Structural, Magnetic, and Transport Properties of Layered Cobalt Oxyfluorides,* $Sr_2CoO_{3+x}F_{1-x}$ $(0 \leq x \leq 0.15)$. Inorganic Chemistry, 2012. **51**(8), 4802-4809.

29. Knee, C.S., A.A. Zhukov, and M.T. Weller, *Crystal structures and magnetic properties of the manganese oxide chlorides* Sr_2MnO_3Cl *and* $Sr_4Mn_3O_{8-y}Cl_2$. Chemistry of Materials, 2002. **14**(10), 4249-4255.

30. Knee, C.S. and M.T. Weller, *New layered manganese oxide halides.* Chemical Communications, 2002(3), 256-257.

31. Needs, R.L., M.T. Weller, U. Scheler, and R.K. Harris, *Synthesis and structure of* Ba_2InO_3X *(X=F,Cl,Br) and* Ba_2ScO_3F*; Oxide/halide ordering in* K_2NiF_4*-type structures.* Journal of Materials Chemistry, 1996. **6**(7), 1219-1224.

32. Hector, A.L., J.A. Hutchings, R.L. Needs, M.F. Thomas, and M.T. Weller, *Structural and Mossbauer study of* Sr_2FeO_3X *(X = F, Cl, Br) and the magnetic structure of* Sr_2FeO_3F. Journal of Materials Chemistry, 2001. **11**(2), 527-532.

33. Galasso, F. and W. Darby, *Preparation, Structure, and Properties of* K_2NbF_3F. Journal of Physical Chemistry, 1962. **66**(7), 1318-&.

34. Knee, C.S., D.J. Price, M.R. Lees, and M.T. Weller, *Two- and three-dimensional magnetic order in the layered cobalt oxychloride* Sr_2CoO_3Cl. Physical Review B, 2003. **68**(17).

35. Wang, Y.K., K.B. Tang, B.C. Zhu, D. Wang, Q.Y. Hao, and Y. Wang, *Synthesis and structure of a new layered oxyfluoride* Sr_2ScO_3F *with photocatalytic property.* Materials Research Bulletin, 2015. **65**, 42-46.

36. Leflem, G., R. Colmet, C. Chaumont, J. Claverie, and P. Hagenmuller, $Ca_2MnO_{4-x}F_x$ *Solid-Solution - Radiocrystallography and Dilatometry.* Materials Research Bulletin, 1976. **11**(4), 389-396.

37. Bouloux, J.C., J.L. Soubeyroux, G. Leflem, and P. Hagenguller, *Bidimensional Magnetic-Properties of Beta-*Sr_2MnO_4*.* Journal of Solid State Chemistry, 1981. **38**(1), 34-39.

38. Tsujimoto, Y., C.I. Sathish, Y. Matsushita, K. Yamaura, and T. Uchikoshi, *New members of layered oxychloride perovskites with square planar coordination:* $Sr_2MO_2Cl_2$ *(M = Mn, Ni) and* $Ba_2PdO_2Cl_2$*.* Chemical Communications, 2014. **50**(44), 5915-5918.

39. Senff, D., P. Reutler, M. Braden, O. Friedt, D. Bruns, A. Cousson, F. Bouree, M. Merz, B. Buchner, and A. Revcolevschi, *Crystal and magnetic structure of* $La_{1-x}Sr_{1+x}MnO_4$*: Role of the orbital degree of freedom.* Physical Review B, 2005. **71**(2).

40. Li, B., Y. Chen, H. Wang, W. Liang, G. Liu, W. Ren, C. Li, Z. Liu, G. Rao, C. Jin, and Z. Zhang, *Unveiling the electronic origin of anion order in* $CrO_{2-x}F_x$*.* Chemical Communications, 2014. **50**(7), 799-801.

41. Brese, N.E. and M. Okeeffe, *Bond-Valence Parameters for Solids.* Acta Crystallographica Section B-Structural Science, 1991. **47**, 192-197.

42. Simon Case, G., A. L. Hector, W. Levason, R. L. Needs, M. F. Thomas, and M. T. Weller, *Syntheses, powder neutron diffraction structures and Mossbauer studies of some complex iron oxyfluorides:* $Sr_3Fe_2O_6F_{0.87}$*,* Sr_2FeO_3F *and* $Ba_2InFeO_5F_{0.68}$*.* Journal of Materials Chemistry, 1999. **9**(11), 2821-2827.

43. Kunz, M. and I.D. Brown, *Out-of-Center Distortions around Octahedrally Coordinated d0 Transition Metals.* Journal of Solid State Chemistry, 1995. **115**(2), 395-406.

44. Pearson, R.G., *Concerning Jahn-Teller Effects.* Proceedings of the National Academy of Sciences of the United States of America, 1975. **72**(6), 2104-2106.

45. Shannon, R.D., *Revised Effective Ionic-Radii and Systematic Studies of Interatomic Distances in Halides and Chalcogenides.* Acta Crystallographica Section A, 1976. **32**(Sep1), 751-767.

46. Tsujimoto, Y., Y. Matsushita, N. Hayashi, K. Yamaura, and T. Uchikoshi, *Anion Order-to-Disorder Transition in Layered Iron Oxyfluoride* Sr_2FeO_3F *Single Crystals.* Crystal Growth & Design, 2014. **14**(9), 4278-4284.

47. Bieringer, M. and J.E. Greedan, *Structure and magnetism in* $BaLaMnO_{4+/-\delta}$ *(*$\delta = 0.00, 0.10$*) and* $Ba_xSr_{1-x}LaMnO_4$*. Disappearance of magnetic order for* $x > 0.30$*.* Journal of Materials Chemistry, 2002. **12**(2), 279-287.

48. Larochelle, S., A. Mehta, L. Lu, P.K. Mang, O.P. Vajk, N. Kaneko, J.W. Lynn, L. Zhou, and M. Greven, *Structural and magnetic properties of the single-layer manganese oxide* $La_{1-x}Sr_{1+x}MnO_4$*.* Physical Review B, 2005. **71**(2).

49. Tsirlin, A.A., A.A. Belik, R.V. Shpanchenko, E.V. Antipov, E. Takayama-Muromachi, and H. Rosner, *Frustrated spin-1/2 square lattice in the layered perovskite* $PbVO_3$*.* Physical Review B, 2008. **77**(9), 092402.

50. Anderson, P.W., *The Resonating Valence Bond State in* La_2CuO_4 *and Superconductivity.* Science, 1987. **235**(4793), 1196-1198.

51. McGlothlin, N., D. Ho, and R.J. Cava, $Sr_3Co_2O_5Cl_2$ *and* Sr_2CoO_3Cl*: two layered cobalt oxychlorides.* Materials Research Bulletin, 2000. **35**(7), 1035-1043.

52. Wu, H., *Phase evolution of layered cobalt oxides versus varying corrugation of the cobalt-oxygen basal plane.* European Physical Journal B, 2002. **30**(4), 501-510.

Chapter 4 A Layered Wide-Gap Oxyhalide Semiconductor with an Infinite ZnO_2 Square Planar Sheet: $Sr_2ZnO_2Cl_2$

4.1 Introduction

The coordination geometry of the transition metal is closely linked to the physical or chemical properties through charge transfer between the metal and ligands and the ligand field energy in the metal center. In condensed matter science, there has been great interest in the study of square planar coordination since high-T_C superconductivity and ideal two-dimensional magnetism arise from CuO_4 square units. The square planar coordination, however, is generally limited to Jahn-Teller active ions (e.g. Cu^{2+} and Ti^{3+}) and 4d/5d metals with a large crystal field energy (e.g. Pd^{2+} and Pt^{2+}). Therefore, properties and electronic states of the transition metals at which the square planar coordination is not thermodynamically favoured have not been well-characterized.

There have been recently great interests in the study of mixed anion systems such as oxyhalides[1-6] and oxypnictides[7-10] because accommodation of more than one anion with different bonding natures in one structure can allow us to design new anion lattices and unusual coordination environment around the metal center. For example, $A_2ZnO_2A'_2Ch_2$ (A = Sr, Ba; A' = Cu, Ag; Ch = S, Se)[11, 12] adopt alternate stacking of $[A'_2Ch_2]^{2-}$ layer with anti-fluorite structure and $[A_2ZnO_2]^{2+}$ layer with ZnO_2 square lattice network as in high T_C cuprate superconductors, as shown in **Figure 4.1**. The Zn center is also loosely bound to two sulphide ions at the apical sites, but the bond lengths are significantly larger than typical ones expected from ionic model. Thus, the pseudo square-planar geometry can be realized for zinc, in contrast to the exclusively stable tetrahedral geometry. Stabilization of such a rare coordination for zinc provides an important playground to study the unexplored properties which differ from those in tetrahedrally coordinated zinc compounds, which is commonly seen in hexagonal wurzite

ZnO[13], as shown in **Figure 4.2**. However, the relationship between the electronic structures and properties related to the Zn-centered square-planar coordination has not been adequately understood yet. $Sr_2ZnO_2Cu_2S_2$ was reported as a possible p-type transparent semiconductor[14], but the electrical properties are mainly derived from a hybridized Cu 3*d* and S 3*p* orbitals comprising the top of the valence bands[15]. Thus, this phase was discussed in terms of copper sulphide chemistry[16].

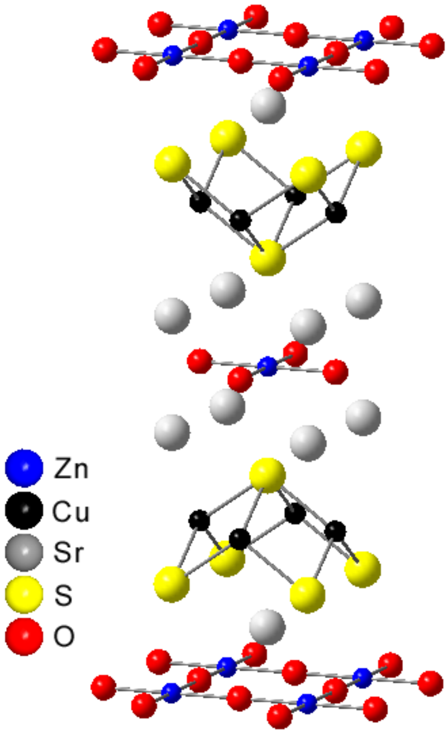

Figure 4.1 Crystal structure of $Sr_2CuZnO_2S_2$, blue, black, grey, yellow and red spheres stand for Zn, Cu, Sr, S and O atoms, respectively.

In this chapter, we report the high-pressure synthesis of the new layered perovskite zinc oxychloride with ZnO_2 square planar sheets, $Sr_2ZnO_2Cl_2$. The oxychloride exhibited an indirect band gap of 3.66 eV in contrast to wurzite ZnO with a direct band gap of 3.37 eV. First principles calculation revealed that the Zn(3*d*)–O(2*p*) antibonding state and Zn(4*s*) dominate the valence band maximum (VBM) and the conduction band minimum (CBM), respectively, with the Cl(3*p*) derived states being located in lower valence bands. Thus, $Sr_2ZnO_2Cl_2$ provides a direct counterpoint to zinc-based compounds with tetrahedral coordination.

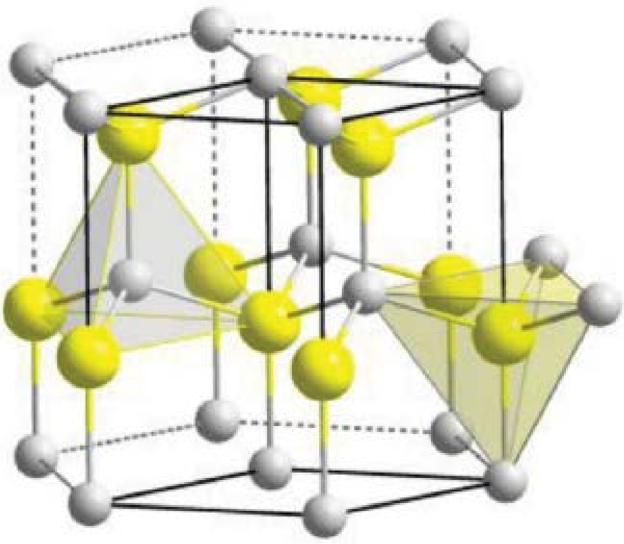

Figure 4.2 Crystal structure of wurzite ZnO, grey and yellow spheres are O atoms and Zn atoms, respectively[13].

4.2 Experimental Details

$Sr_2ZnO_2Cl_2$ was synthesized from a stoichiometric mixture of SrO, $SrCl_2$, and ZnO. SrO was obtained by heating $SrCO_3$ at 1100 °C in flowing oxygen gas. The mixture enclosed in a Pt capsule was heated in a belt-type high-pressure apparatus at 6 GPa and 1500 °C. After heating for 1 h, the sample was quickly quenched to room temperature by switching off the heater. Then the pressure was slowly released. The sample colour was white, which is consistent with the d^{10} electronic configuration of Zn^{2+}. Synchrotron X-ray powder diffraction (SXRD) measurement was performed at room temperature on BL15XU at SPring-8[17]. The wavelength was $\lambda = 0.65298$ Å. Because the product was highly hygroscopic, the powder sample was sealed into capillary in an Ar-filled glovebox for the measurement. Neutron powder diffraction (NPD) measurements were carried out at various temperatures with a high-resolution diffractometer ECHIDNA at ANSTO ($\lambda = 1.622$ Å). The SXRD and NPD data were analysed by the Rietveld method using the programs RIETAN-FP[18] and FullProf[19], respectively. Diffuse-reflectance spectra were measured at room temperature using a UV-Vis-NIR spectrophotometer (JASCO, V-570). Elemental analysis for the single crystal sample was conducted using a scanning electron microscope (SEM, HITACHI-TM3000) equipped with an energy dispersive X-ray spectroscopy (EDX) analyser (Oxford Instruments, SwiftED3000). The accelerating voltage was 15 kV.

The *ab initio* calculations were performed on the basis of the basis of the plane-wave pseudopotential strategy using the computer program VASP (Vienna *Ab Initio* Simulation Package)[20]. The projector- augmented wave approach[21, 22] and the generalized-gradient approximation of PBE-type were used[23]. An energy cutoff of 400 eV was chosen, and the lattice parameters and atomic positions were optimized until the residual force was less than 0.01 eV/Å. The *k*-point grid of 16 × 16 × 4 was automatically generated according to the method by Monkhorst and Pack[24]. The density of state and chemical bonding analyses were calculated by the LOBSTER code[25].

4.3 Results and Discussion

4.3.1 Crystal Structure

A photograph of a hand-picked crystal is shown in the inset of **Figure 4.3**. Elemental analysis by SEM-EDX displayed in **Figure 4.3** resulted in an average atomic ratio of Sr : Zn : Cl = 1.90 : 1 : 1.45. The Cl content is somewhat small relative to the nominal composition. **Figure 4.4(a)** shows the SXRD patterns collected from $Sr_2ZnO_2Cl_2$, which could be readily indexed by a simple body-centered tetragonal cell with the space group *I*4/*mmm*. The calculated lattice constants are a = 4.06981(2) Å and c = 15.20076(8) Å[26]. These values are very close to those for $Sr_2CuO_2Cl_2$ with the n = 1 Ruddlesden-Popper (RP) type structure (a = 3.9716 Å, c = 15.6126 Å). Rietveld structural refinement was performed on the basis on a model of $Sr_2CuO_2Cl_2$, with Sr on 4*e* (0, 0, *z*), Zn on 2*a* (0, 0, 0), O on 4*c* (0, 0.5, 0), and Cl on 4*e* (0, 0, *z*). The refinement converged well with reasonable reliability factors (R_{wp} = 1.15%, R_{B} =

1.45%). No site deficiencies were found for all chemical species. However, the Rietveld refinement against the room-temperature NPD data shown in **Figure 4.4(b)**, which is more sensitive to the scattering of the oxide and chloride ions than X-ray data, revealed deficiencies at the chloride site as well as the zinc site, giving a refined composition formula of $Sr_2Zn_{0.962}O_2Cl_{1.92}$. The oxidation state of the Zn ion is 1.97, which is consistent with the white sample colour associated with the closed shell electronic configuration of Zn^{2+}. The crystal structure and refined structural parameters including selected bond lengths are displayed in **Figure 4.6 (a)** and **Table 4.1** and **4.2**, respectively. The bond-valence-sum calculation resulted in 2.00 for Sr and 1.83 for Zn. These values agree well with the oxidation number expected from the estimated chemical composition. In addition, there is no phase transition down to 3 K, suggesting the persistence of the *I*4/mmm space group, as seen in **Figure 4.5**.

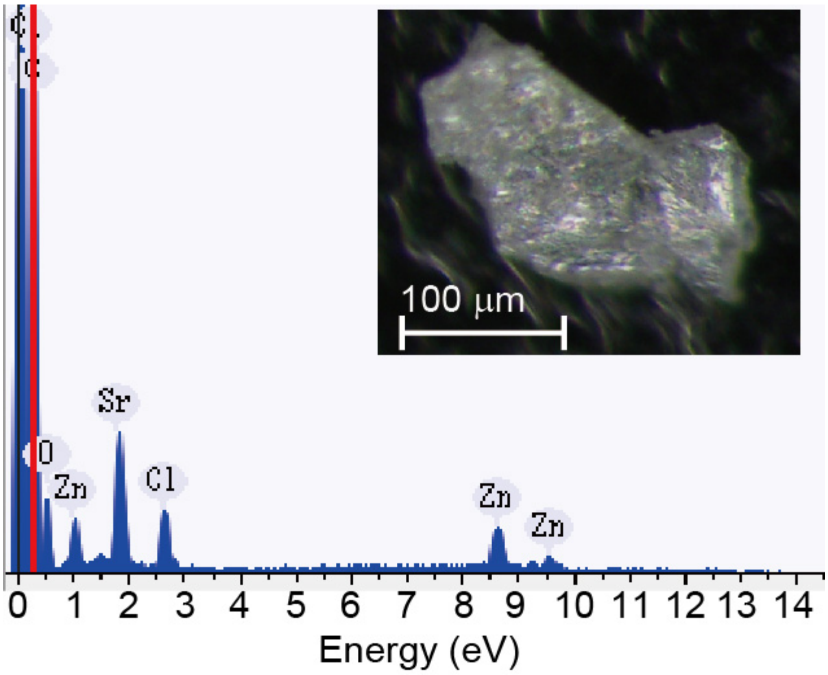

Figure 4.3 Energy dispersive X-ray spectrum collected from a typical Sr2ZnO2Cl2crystal of. The inset shows a photograph of a white transparent crystal of the oxychloride compound. **(b)** Crystal structure of $Sr_2ZnO_2Cl_2$. White, blue, red, and green spheres represent Sr, Zn, O, and Cl atoms.

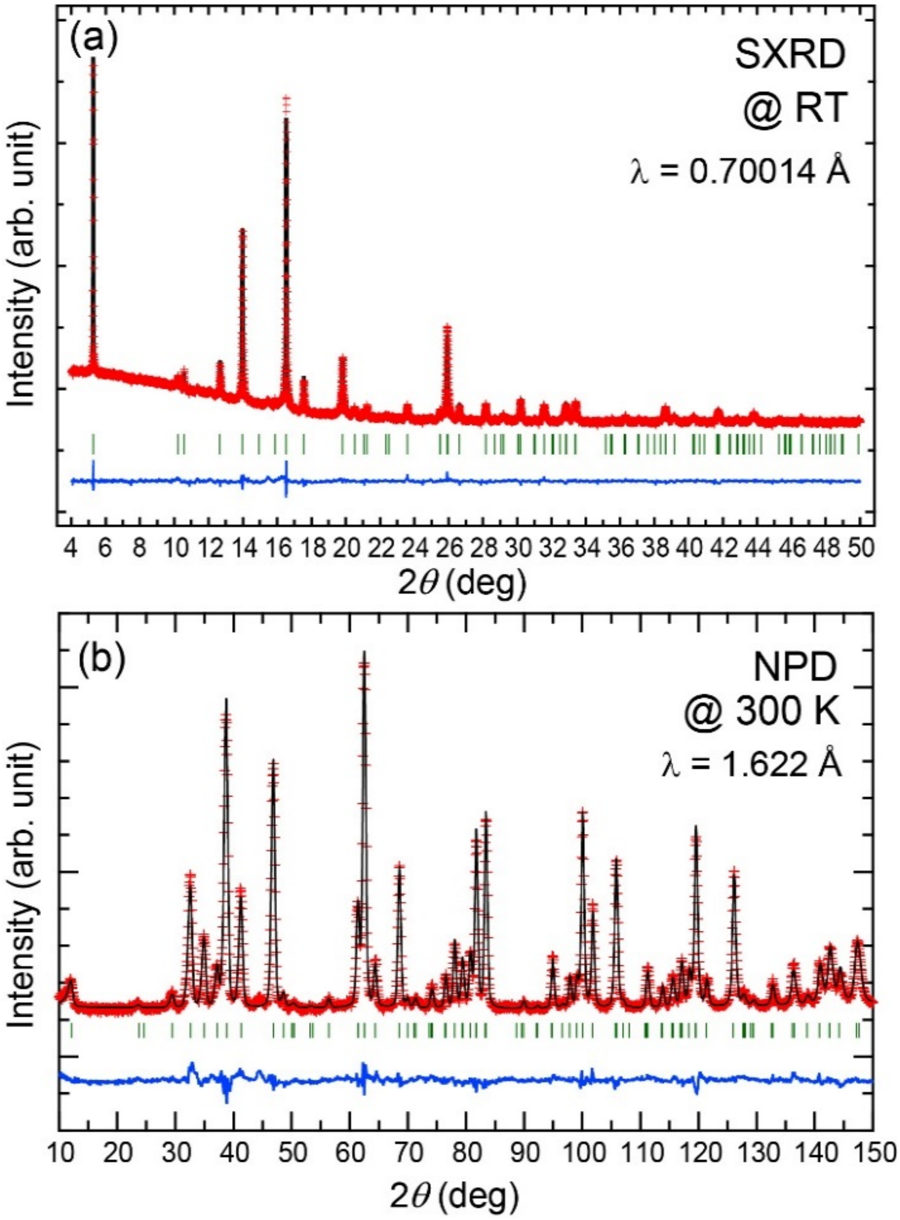

Figure 4.4 Rietveld structural refinements against **(a)** synchrotron X-ray diffraction (SXRD) and **(b)** neutron powder diffraction (NPD) patterns collected from $Sr_2ZnO_2Cl_2$. Obtained, calculated, and difference are plotted by cross marks, upper solid lines, and bottom solid lines, respectively. Vertical lines represent the Bragg peak positions.

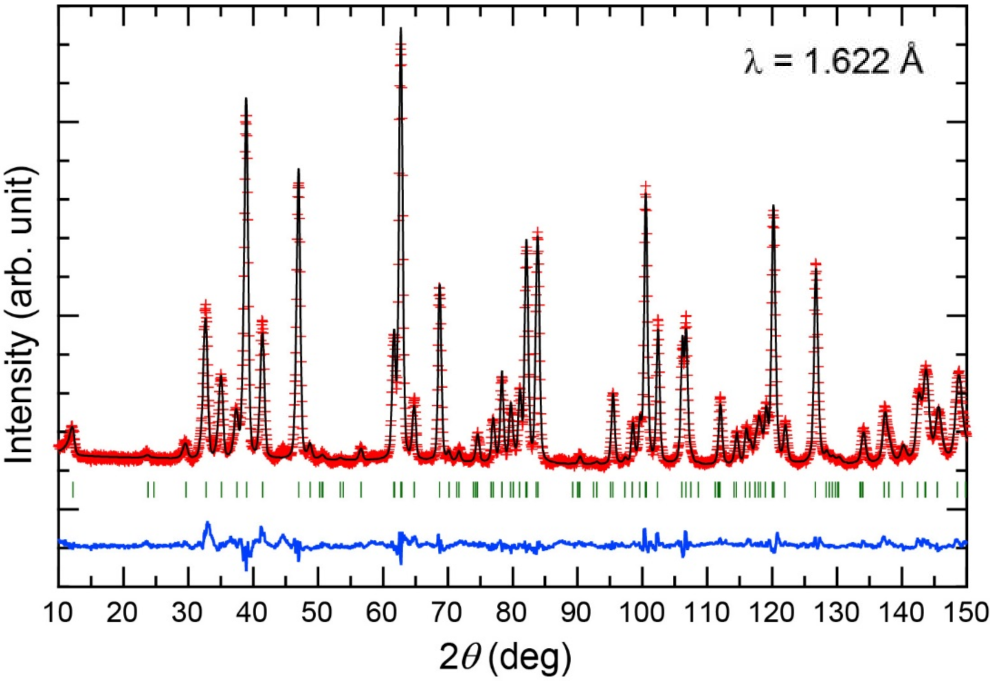

Figure 4.5 Rietveld structural refinement against the neutron diffraction patterns collected from $Sr_2ZnO_2Cl_2$ at 3 K. The zinc oxychloride adopts the *I*4/*mmm* space group with *a* = 4.057723(1) Å and *c* = 15.114116(4) Å. Sr on 4*e* (0, 0, 0.39208(8)), Zn on 2*a* (0, 0, 0), O on 4*c* (0, 0.5, 0), and Cl on 4*e* (0, 0, 0.18225(7)). The site occupancy factors (*g*) were fixed at those obtained from the refinements using the 300 K data, namely, *g*(Zn) = 0.962 and *g*(Cl) = 0.950. Isotropic atomic displacement parameters (B_{iso}) were 0.204(3) Å^2 for Sr, 0.03(5) Å^2 for Zn, 0.408(1) Å^2 for O, and 0.2150(4) Å^2 for Cl. Reliability factors were R_{wp} = 8.88% and R_B = 3.83%, and Goodness-of-fit = 1.8.

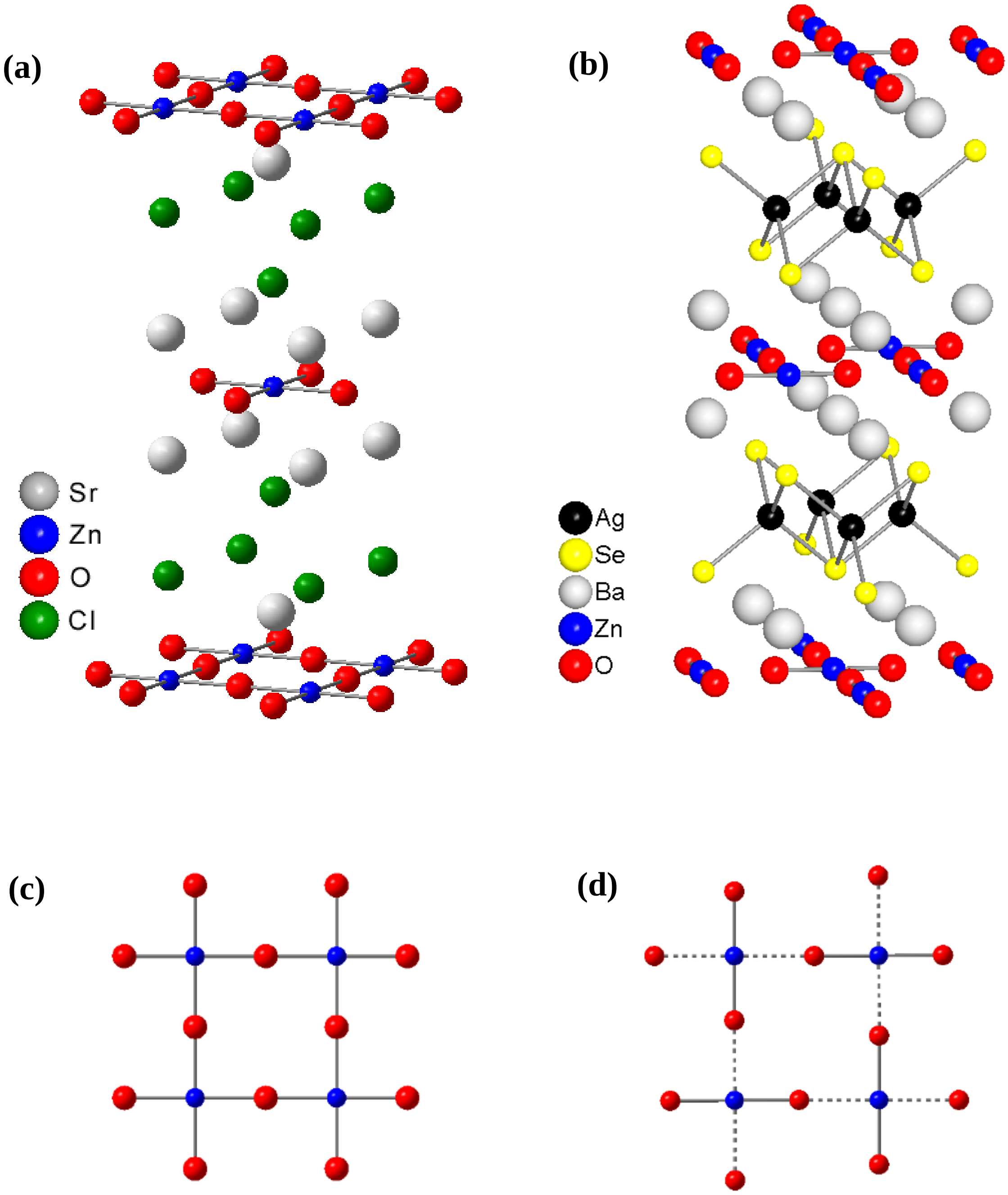

Figure 4.6 Crystal structure of **(a)** $Sr_2ZnO_2Cl_2$ and **(b)** $Ba_2ZnO_2Ag_2Se_2$. The ZnO_2 sheets in **(c)** $Sr_2ZnO_2Cl_2$ and **(d)** $Ba_2ZnO_2Ag_2Se_2$

Table 4.1 Crystallographic Parameters Refined from Neutron and SXRD Data Collected from $Sr_2ZnO_2Cl_2$ at Room Temperature.

atom	Wyckoff positions	*x*	*y*	*z*	occupancy	B_{iso}/ Å^2	BVS
NPD, *a* = 4.06877 (9) Å, *c* = 15.19680(3) Å. *R* Indices were R_{wp} = 10.0%, R_B = 4.93%, *S* = 1.8%.							
Sr	4*e*	0	0	0.39219(11)	1	0.64(2)	2.04
Zn	2*a*	0	0	0	0.962(9)	0.53(5)	2.0
O	4*c*	0	0.5	0	1	0.73(2)	1.83
Cl	4*e*	0	0	0.18176(9)	0.950(5)	0.84(2)	1.12
SXRD, *a* = 4.06981 (2) Å, *c* = 15.20076(8) Å. *R* Indices were R_{wp} = 1.154%, R_p = 0.854%, R_B = 1.451%, and R_F = 0.584%.							
Sr	4*e*	0	0	0.39328(5)	1	0.526(23)	2.04
Zn	2*a*	0	0	0	1	0.250(48)	1.89
O	4*c*	0	0.5	0	1	0.90(13)	1.90
Cl	4*e*	0	0	0.18260(12)	1	0.287(57)	1.09

Table 4.2 Selected bond lengths of the **r**efined data from Neutron and SXRD Data Collected from $Sr_2ZnO_2Cl_2$ at Room Temperature.

Bond length/ Å	Zn-O ×4	Zn-Cl ×2	Sr-O ×4	Sr-Cl ×4	Sr-Cl ×1
NPD	2.03438(5)	2.7622(14)	2.6121(11)	3.0888(8)	3.0888(8)
SXRD	2.03490(0)	2.7757(19)	2.6024(5)	3.1003(8)	3.202(2)

The local coordination environment around the Zn center is very similar to those seen from related layered oxychlorides and the layered oxychalcogenides described above: the zinc ion is surrounded with four oxide ions at the equatorial sites and two chloride ions at the apical sites. The Zn-O bond length is 2.03439(1) Å, which is in good agreement with the sum of ionic radii of 4-coordinate Zn^{2+} (0.74 Å) and O^{2-} (1.26 Å)[27]. This indicates that the zinc center forms covalent bonds with four surrounding oxide ions in the basal plane. In contrast, the Zn-Cl bond distance is 2.762(1) Å, much larger than the sum of ionic radii of Zn^{2+} and Cl^{-} ions (1.67 Å)[27]. Thus, the chloride ions are out of the first coordination sphere, and the interaction between Zn and Cl would be very weak. The effective coordination number (ECoN) computed by the program VESTA[28] is 4.03, which is comparable to those for $Sr_2CuO_2Cl_2$ (ECoN = 4.00) with a pseudo square planar coordination.

Several zinc-centered oxyhalide compounds have been reported, but the pseudo square planar geometry observed in the present compound is quite unique. In $Zn_2(SeO_3)Cl_2$ and $Zn_2(TeO_3)Br_2$ with the sophiite structure[29, 30], zinc atoms are pyramidally coordinated by four equatorial oxygen atoms at 1.996-2.184 Å and one sufficiently hybridizing apical X atom at 2.394 Å for Cl and 2.531 Å for Br, as shown in **Figure 4.7**, ZnO_2Br_2 tetrahedra is also formed. In $Zn_2(SeO_3)Cl_2$, this corner sharing ZnO_2Cl_2 tetrahedra also links the ZnO_4Cl pyramid. The zinc-halogen boracite, $Zn_3B_7O_{13}X$ (X = Cl, Br) contains zinc atoms in square pyramidal coordination by four oxygen and one halogen atoms, but the Zn-Cl bond is intermediate in length (2.515 Å)[31, 32]. $NaZn(SO_4)F$ has been reported in which the zinc center is octahedrally coordinated by four O atoms at 2.194 Å or 2.212 Å and two F atoms at 1.961 Å[33].

The ZnO_4 square unit in $Sr_2ZnO_2Cl_2$ was found to be free from distortion down to 3 K, unlike $Ba_2ZnO_2Ag_2Se_2$ (orthorhombic cell, *Cmca*) which exhibits a rhombic distortion with two short and two long Zn-O bond lengths[12]. The ZnO_4 square unit in $Sr_2ZnO_2Cl_2$ is a regular square planar, while the one in $Ba_2ZnO_2Ag_2Se_2$ has discrete ZnO_2 linear units, which can be clearly seen in **Figure 4.6(d)**. The lattice constants, volume and Zn-O/Zn-Cl bond lengths smoothly decreased with lowering temperature as shown in **Figure 4.8**. The observed distortion of the ZnO_4 square in $Ba_2ZnO_2Ag_2Se_2$ has been assumed to be due to the large Ba^{2+}, Ag^+ and Se^{2+} ions[12]. To examine a possibility of similar polyhedral distortion in related oxychloride family, we synthesized $Ba_2ZnO_2Cl_2$ under 6 GPa and 1800 °C. However, as shown in **Figure 4.9**. The preliminary structural analysis using a laboratory XRD machine did not detect a deviation from $I4/mmm$, although the Zn-O bond length (= 2.128 Å) estimated from the a axis length was very close to the average Zn-O bond length (= 2.141 Å) in $Ba_2ZnO_2Ag_2Se_2$[12].

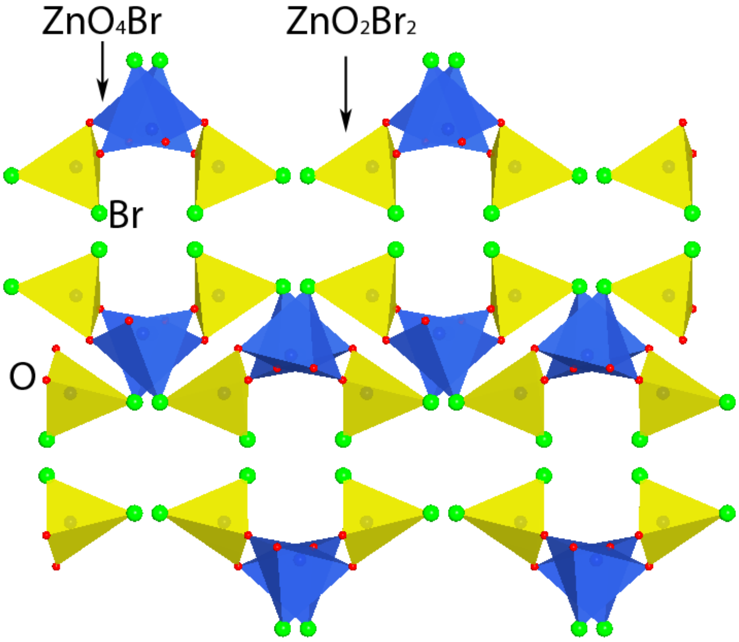

Figure 4.7 Crystal structure of $Zn_2(TeO_3)Br_2$, two zinc coordination environment exist, i.e, ZnO_4Br square pyramidal and ZnO_2Br_2 tetrahedra.

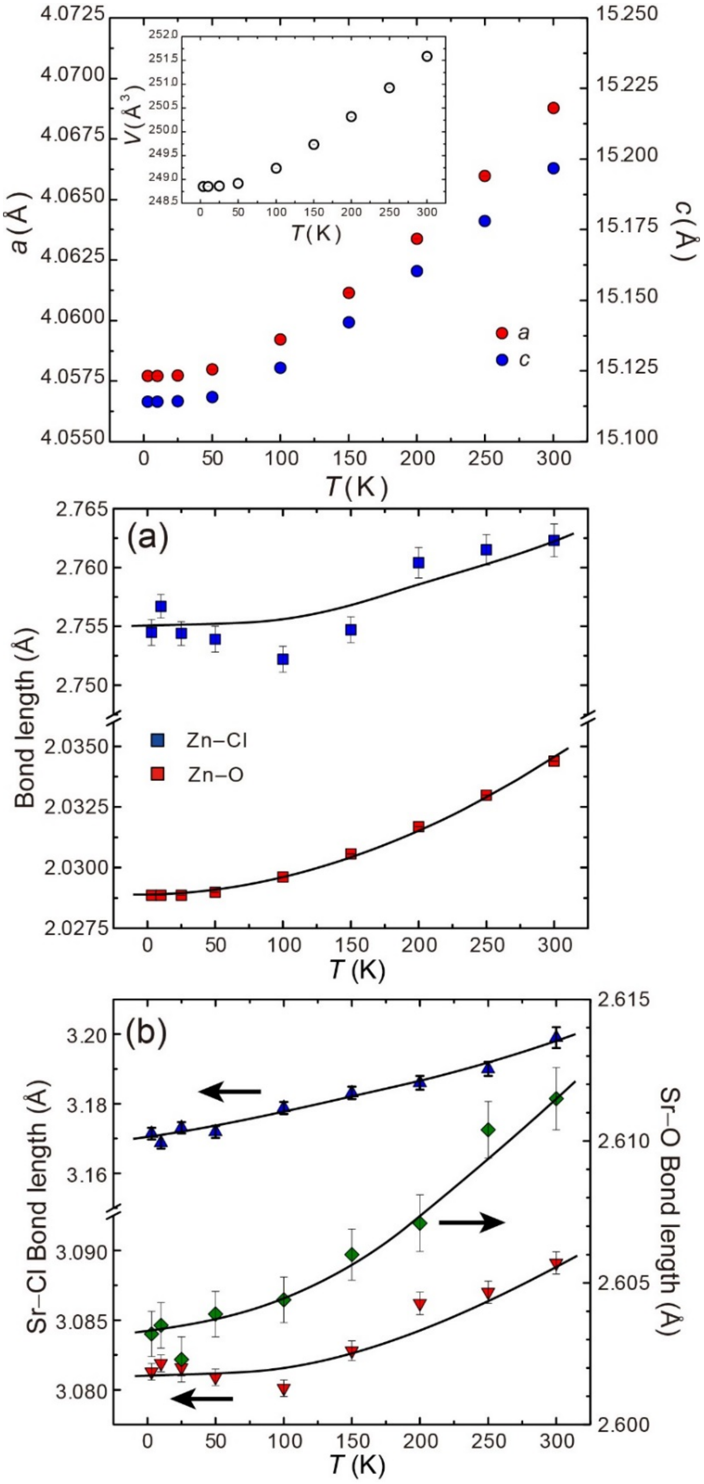

Figure 4.8 Temperature evolution of the lattice constants, volume, Zn-O/Zn-Cl bond lengths, and Sr-O/Sr-Cl bond lengths, which were obtained by Rietveld structure refinements.

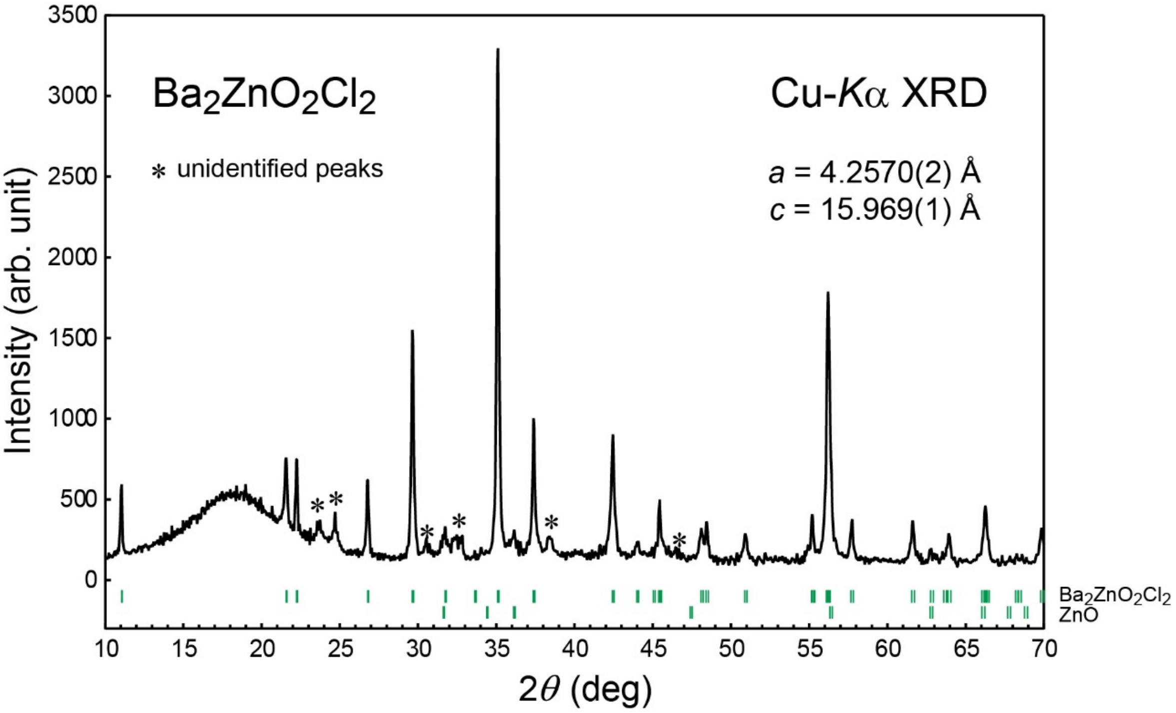

Figure 4.9 Laboratory X-ray diffraction (Cu-K_α radiation) patterns collected from $Ba_2ZnO_2Cl_2$ at room temperature, which was synthesized at 1800 °C and 6 GPa. Due to the hygroscopic nature, the powder sample was suspended in liquid paraffin for the measurement. The XRD data were readily assigned by the *I*4/*mmm* space group with *a* = 4.2570(2) Å and *c* = 15.969(1) Å. In the XRD patterns, wurtzite ZnO and unidentified peaks were detected as impurities. Vertical lines represent expected Bragg peak positions for $Ba_2ZnO_2Cl_2$ (*I*4/*mmm*) and wurtzite ZnO.

4.3.2 UV-vis Spectrum Study

Figure 4.10 shows the UV-Vis-NIR absorption spectrum for $Sr_2ZnO_2Cl_2$, which was converted from the diffuse reflectance by the Kubelka-Munk function, $f(R) = (1 - R)^2/2R$, where *R* is the reflectance. The absorption curve exhibited a steep increase below 300 nm, which is a typical optical response of wide-gap semiconductors. The weak absorption shoulder observed in the range of wavelength from 300 to 450 is probably caused by the hygroscopic nature of the oxychloride. It was not able to fully avoid deliquescence because samples were exposed to air during the spectroscopic measurements. The optical band gap of the zinc oxychloride was estimated by equation of $(f(R)h\upsilon)^n = A(h\upsilon - E_g)$, where h = Planck’s constant, υ = light frequency, E_g = band gap, A = proportional constant, n = 1 or 1/2 depending on whether the transition is direct or indirect. We chose n = 1/2 because theoretical calculation described later predicted the indirect band gap. The Tauc plot shown in the inset of **Figure 4.10** gave an indirect band-gap value of 3.66 eV, which is somewhat larger than those of ZnO and $Sr_2Cu_2ZnO_2S_2$ (2.7 eV)[15] with a direct band gap. It should be noted that the indirect band gap for our compound originates from the square planar geometry for Zn, as discussed below.

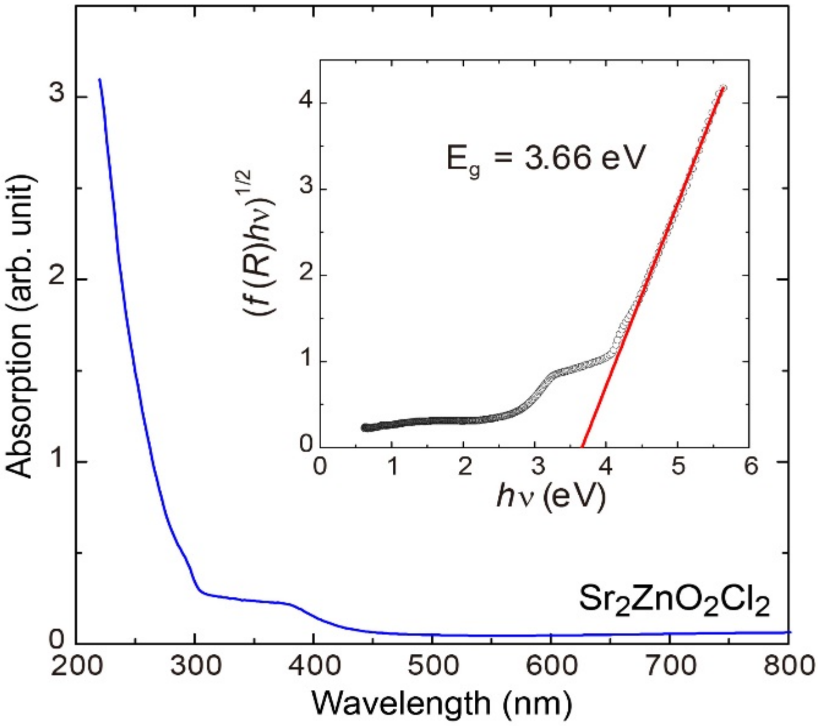

Figure 4.10 UV-vis-NIR diffuse reflectance spectrum of $Sr_2ZnO_2Cl_2$ measured at room temperature. Inset shows the Tauc plot obtained on the basis of the equation $(f(R)h\upsilon)^n = A(h\upsilon - E_g)$ for band gap estimation, where $f(R)$, A, and E_g represents the Kubelka-Munk function, proportional constant, and band gap. The n = 1/2 suggests an indirect gap of 3.66 eV in the oxychloride compound.

4.3.3 Band Structure

Band structures for $Sr_2CuO_2Cl_2$ were calculated at the computationally optimized and stoichiometric crystal structure with lattice parameters a = 4.090 Å and c = 15.20 Å, which are in accordance with the experimentally determined lattice parameters. The total and partial density-of-states (pDOS) for $Sr_2ZnO_2Cl_2$ are shown in **Figure 4.11**, and band dispersions in several symmetry directions are shown in **Figure 4.12**. These results clearly show a semiconducting state with an indirect band gap between the valence band maximum (VBM) at M point and the conduction band minimum (CBM) at Γ point, which is different from the direct gap at Γ point in ZnO. The calculated band gap energy is 1.8 eV, which is much smaller than the experimental one. This is a typical error in using GGA-PBA calculation. The O 2*p* band is highly dispersive ranging from -8 to 1 eV. The Zn 3*d* band is mainly located in the energy range from -8 and -6 eV, resulting in a strong hybridization with O 2*p* orbitals in comparison with the Cl 3*p* orbitals with the band located between -6 and -4 eV. The VBM is derived from the O 2*p* orbitals hybridized with the Zn $3d_{x^2-y^2}$ orbitals. The crystal orbital Hamiltonian population (COHP) analysis for the Zn-O interactions shown in **Figure 4.13** indicates that the VBM is Zn($3d_{x^2-y^2}$)-O(2*p*) antibonding. Similar antibonding state was observed in $Sr_2CuO_2Cl_2$ with the Cu ($3d_{x^2-y^2}$)-O(2*p*) antibonding subbands within the top of valence bands[34, 35]. The CBM is mainly composed of a dispersive Zn 4*s* band, forming an antibonding state with O 2*p* band. The higher energy regions are occupied by Sr 4*d*/5*s* and Zn 4*p* states. As a result, the indirect gap is attributed to a transition between O *2p* and Zn *4s* energy bands.

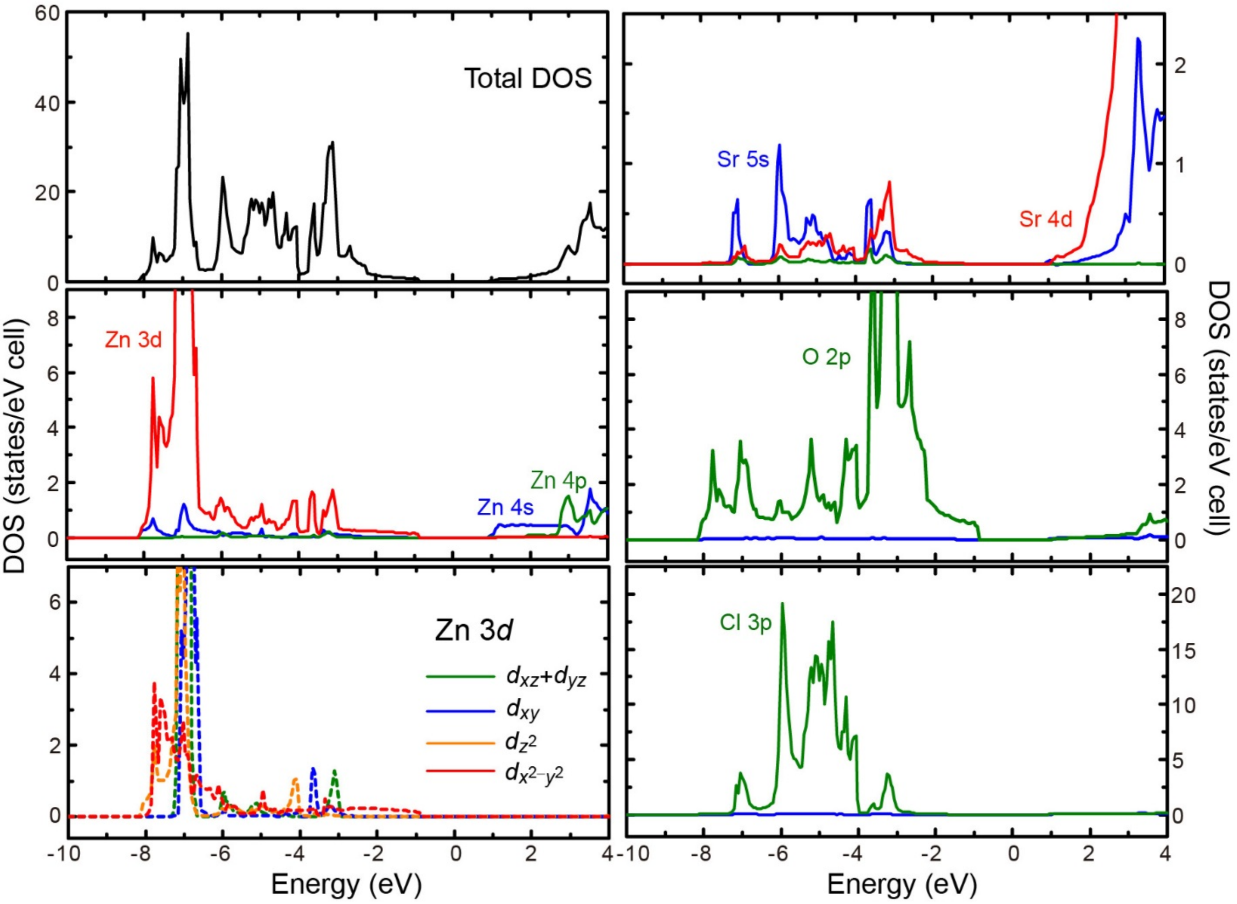

Figure 4.11 Diagrams of total and partial density of states (DOS) for Sr, Zn, O, and Cl in $Sr_2ZnO_2Cl_2$. Blue, green, red lines stand for *s*, *p*, and *d* orbitals, respectively. Black line represents the total DOS. The inset figures correspond to the partial DOS for Zn and O orbitals on a different scale.

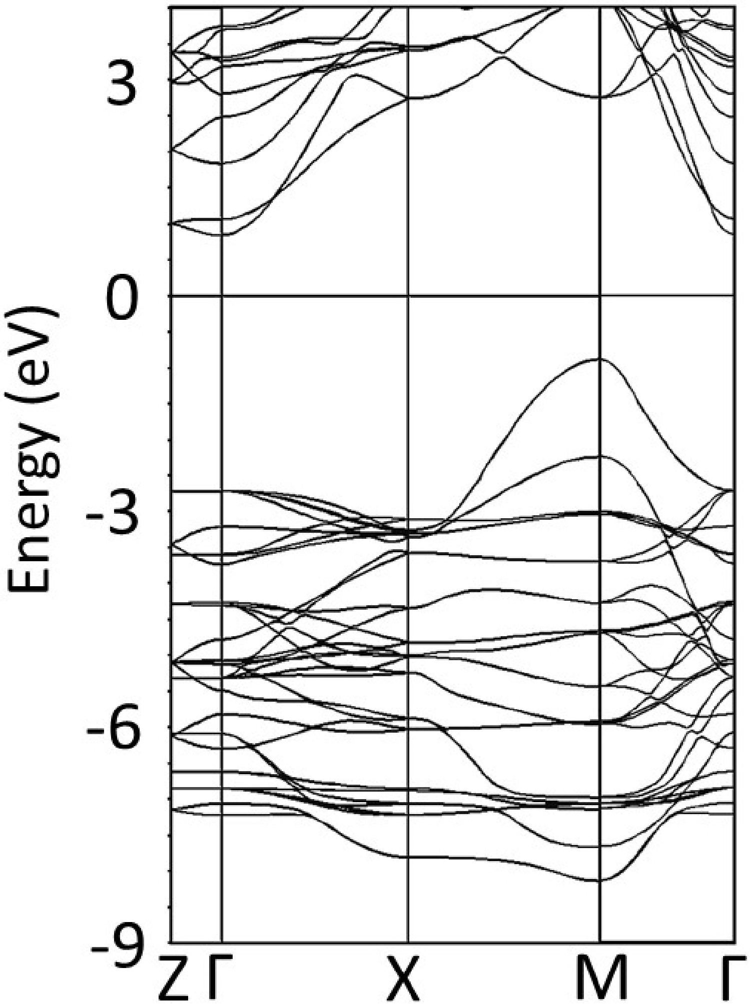

Figure 4.12 Band dispersions for $Sr_2ZnO_2Cl_2$ calculated along high symmetry lines within the GGA framework.

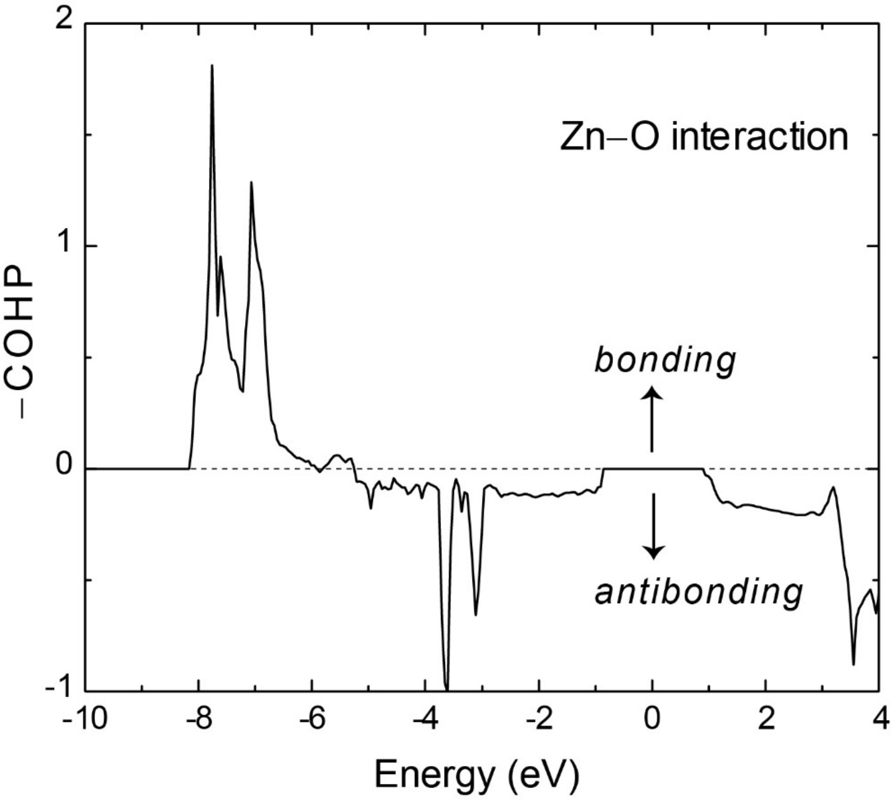

Figure 4.13 Crystal Orbital Hamiltonian Population (COHP) for Zn-O interaction in $Sr_2ZnO_2Cl_2$. The COHP curve shows bonding state between Zn 3*d* and O 2*p* orbitals in the energy range from -8 to -6 eV, but antibonding states in the valence band maximum.

The reason for the indirect gap in the zinc oxychloride can be explained by considering the point group at the Zn site, as discussed in other reports[36-38]. For zinc blende ZnO with the T_d symmetry, as well as wurtzite, a hybridization between the anion *p* and the cation *d* states is symmetry allowed throughout the Brillouin zone, leading to an upward shift of the O 2*p*-like states of the VBM at Γ point through mixing of antibonding character into the VBM. In contrast, such a *p-d* repulsion for the D_{4h} symmetry is symmetry forbidden at the point, but occurs at other points away from point. As a result, the band gap of $Sr_2ZnO_2Cl_2$ becomes indirect. Similar indirect band gap caused by the *p-d* repulsion, but at L point and at the Σ line between K and Γ points, was observed in rock-salt ZnO (high-pressure polymorph) with the octahedral symmetry (O_h)[37-39]. The rock-salt phase exhibits much smaller Zn-O bond length (at ambient pressure) and band gap than those for our present compound[39, 40]. This likely results from stronger hybridization between Zn 3*d* and O 2*p* orbitals on the square planar geometry. Such a well-hybridized band would enhance the mobility parallel to the *ab* plane and the antibonding bonding valence maximum is expected to bring defect tolerant. Thus, $Sr_2ZnO_2Cl_2$ is a potential candidate for transparent semiconductor with high mobility. We preliminarily investigated carrier doping by Na^+ ions into $Sr_2ZnO_2Cl_2$, but up to 5 at% Na doping, namely $Sr_{1.9}Na_{0.1}ZnO_2Cl_2$, the electrical resistance was too high to be measured. Further study on carrier doping toward transparent conductivity is in progress.

4.4 Summary of Chapter 4

In this chapter, a new layered perovskite zinc oxychloride, $Sr_2ZnO_2Cl_2$, with an infinite ZnO_2 square planar sheet has been successfully synthesized by high pressure method. The oxychloride possesses an indirect band gap of E_g = 3.66 eV, corresponding to a transition between O 2*p* and Zn 4*s* energy bands. These results result from the electronic nature of the square planar geometry for zinc.

References in chapter 4

1. Tsujimoto, Y., S. Nakano, N. Ishimatsu, M. Mizumaki, N. Kawamura, T. Kawakami, Y. Matsushita, and K. Yamaura, *Pressure-Driven Spin Crossover Involving Polyhedral Transformation in Layered Perovskite Cobalt Oxyfluoride.* Scientific Reports, 2016. **6**.
2. Tsujimoto, Y., C.I. Sathish, Y. Matsushita, K. Yamaura, and T. Uchikoshi, *New Members of Layered Oxychloride Perovskites with Square Planar Coordination:* $Sr_2MO_2Cl_2$ *(M = Mn, Ni) and* $Ba_2PdO_2Cl_2$*.* Chemical Communications, 2014. **50**(44), 5915-5918.

3. Fujito, H., H. Kunioku, D. Kato, H. Suzuki, M. Higashi, H. Kageyama, and R. Abe, *Layered Perovskite Oxychloride* Bi_4NbO_8Cl*: A Stable Visible Light Responsive Photocatalyst for Water Splitting.* Journal of the American Chemical Society, 2016. **138**(7), 2082-2085.

4. Batuk, M., D. Batuk, A.A. Tsirlin, D.S. Filimonov, D.V. Sheptyakov, M. Frontzek, J. Hadermann, and A.M. Abakumov, *Layered Oxychlorides [PbBiO2]A(n+1)B(n)O(3n-1)Cl(2) (A = Pb/Bi, B = Fe/Ti): Intergrowth of the Hematophanite and Sillen Phases.* Chemistry of Materials, 2015. **27**(8), 2946-2956.

5. Clemens, O., R. Kruk, E.A. Patterson, C. Loho, C. Reitz, A.J. Wright, K.S. Knight, H. Hahn, and P.R. Slater, *Introducing a Large Polar Tetragonal Distortion into Ba-Doped* $BiFeO_3$ *by Low-Temperature Fluorination.* Inorganic Chemistry, 2014. **53**(23), 12572-12583.

6. Kodenkandath, T.A., J.N. Lalena, W.L.L. Zhou, E.E. Carpenter, C. Sangregorio, A.U. Falster, W.B. Simmons, C.J. O'Connor, and J.B. Wiley, *Assembly of Metal-Anion Arrays Within a Perovskite Host. Low-temperature Synthesis of New Layered Copper-Oxyhalides,* $(CuX)LaNb_2O_7$*, X = Cl, Br.* Journal of the American Chemical Society, 1999. **121**(46), 10743-10746.

7. Yajima, T., K. Nakano, F. Takeiri, T. Ono, Y. Hosokoshi, Y. Matsushita, J. Hester, Y. Kobayashi, and H. Kageyama, *Superconductivity in* $BaTi_2Sb_2O$ *with a d(1) Square Lattice.* Journal of the Physical Society of Japan, 2012. **81**(10).

8. Paglione, J. and R.L. Greene, *High-Temperature Superconductivity in Iron-based Materials.* Nature Physics, 2010. **6**(9), 645-658.

9. Brock, S.L. and S.M. Kauzlarich, $A_2Zn_3As_2O_2$ *(A=Ba, Sr) - A Rare Example of Square-Planar Zinc.* Inorganic Chemistry, 1994. **33**(11), 2491-2492.

10. Pitcher, M.J., D.R. Parker, P. Adamson, S.J.C. Herkelrath, A.T. Boothroyd, R.M. Ibberson, M. Brunelli, and S.J. Clarke, *Structure and Superconductivity of LiFeAs.* Chemical Communications, 2008(45), 5918-5920.

11. Zhu, W.J. and P.H. Hor, *Unusual layered transition-metal oxysulfides: Sr2Cu2MO2S2 (M=Mn, Zn)*. Journal of Solid State Chemistry, 1997. **130**(2), 319-321.

12. Herkelrath, S.J.C., I. Saratovsky, J. Hadermann, and S.J. Clarke, *Fragmentation of an Infinite ZnO_2 Square Plane into Discrete [ZnO2](2-) Linear Units in the Oxyselenide $Ba_2ZnO_2Ag_2Se_2$*. Journal of the American Chemical Society, 2008. **130**(44), 14426-+.

13. Khaksar, M., M. Amini, and D.M. Boghaei, *Efficient and green oxidative degradation of methylene blue using Mn-doped ZnO nanoparticles ($Zn_{1-x}Mn_xO$)*. Journal of Experimental Nanoscience, 2015. **10**(16), 1256-1268.

14. Ueda, K., S. Hirose, H. Kawazoe, and H. Hosono, *Electrical and optical properties of layered oxysulfides with CuS layers: Sr-Cu-M-O-S system (M = Zn, Ga, In)*. Chemistry of Materials, 2001. **13**(5), 1880-1883.

15. Hirose, H., K. Ueda, H. Kawazoe, and H. Hosono, *Electronic structure of $Sr_2Cu_2ZnO_2S_2$ layered oxysulfide with CuS layers*. Chemistry of Materials, 2002. **14**(3), 1037-1041.

16. Vajenine, G.V. and R. Hoffmann, *Compounds Containing Copper-Sulfur Layers: Electronic structure, Conductivity, and Stability*. Inorganic Chemistry, 1996. **35**(2), 451-457.

17. Tanaka, M., Y. Katsuya, Y. Matsushita, and O. Sakata, *Development of a Synchrotron Powder Diffractometer with a One-Dimensional X-ray Detector for Analysis of Advanced Materials*. Journal of the Ceramic Society of Japan, 2013. **121**(1411), 287-290.

18. Izumi, F. and K. Momma, *Three-Dimensional Visualization in Powder Diffraction*. Applied Crystallography XX, 2007. **130**, 15-20.

19. Rodriguezcarvajal, J., *Recent Advances in Magnetic-Structure Determination by Neutron Powder Diffraction*. Physica B, 1993. **192**(1-2), 55-69.

20. Kresse, G. and J. Hafner, *Ab initio molecular dynamics for liquid metals*. Physical Review B, 1993. **47**(1), 558-561.

21. Blöchl, P.E., *Projector augmented-wave method*. Physical Review B, 1994. **50**(24), 17953-17979.

22. Kresse, G. and D. Joubert, *From ultrasoft pseudopotentials to the projector augmented-wave method.* Physical Review B, 1999. **59**(3), 1758-1775.

23. Perdew, J.P., J.A. Chevary, S.H. Vosko, K.A. Jackson, M.R. Pederson, D.J. Singh, and C. Fiolhais, *Atoms, molecules, solids, and surfaces: Applications of the generalized gradient approximation for exchange and correlation.* Physical Review B, 1992. **46**(Copyright (C) 2009 The American Physical Society), 6671-6687.

24. Monkhorst, H.J. and J.D. Pack, *Special points for Brillouin-zone integrations.* Physical Review B, 1976. **13**(12), 5188-5192.

25. Tank, R.J., O.; Burkhardt, A.; Andersen, O. K., *LMTO. 2000.*

26. Miller, L.L., X.L. Wang, S.X. Wang, C. Stassis, D.C. Johnston, J. Faber, and C.K. Loong, *Synthesis, Structure, and Properties of* $Sr_2CuO_2Cl_2$. Physical Review B, 1990. **41**(4), 1921-1925.

27. Shannon, R.D., *Revised Effective Ionic-Radii and Systematic Studies of Interatomic Distances in Halides and Chalcogenides.* Acta Crystallographica Section A, 1976. **32**(Sep1), 751-767.

28. Momma, K. and F. Izumi, *VESTA 3 for three-dimensional visualization of crystal, volumetric and morphology data.* Journal of Applied Crystallography, 2011. **44**, 1272-1276.

29. Zhang, D. and M. Johnsson, $Zn_2TeO_3Br_2$. Acta Crystallographica Section E-Structure Reports Online, 2008. **64**, I26-U16.

30. Semenova, T.F., I.V. Rozhdestvenskaya, S.K. Filatov, and L.P. Vergasova, *Crystal-Structure and Physical-Properties of Sophiite,* $Zn_2(SeO_3)Cl_2$*, a New Mineral.* Mineralogical Magazine, 1992. **56**(383), 241-245.

31. Campa-Molina, J., S. Ulloa-Godinez, A. Barrera, L. Bucio, and J. Mata, *Nano and Micro Reoriented Domains and Their Relation with the Crystal Structure in the New Ferroelectric Boracite* $Zn_3B_7O_{13}Br$. Journal of Physics-Condensed Matter, 2006. **18**(20), 4827-4837.

32. Mao, S.Y., M.E. Mendozaalvarez, W. Depmeier, F. Kubel, H. Schmid, and K. Yvon, *Structure Refinement of Trigonal Zinc-Chlorine Boracite, $Zn_3B_7O_{13}Cl$, from Single-Crystal and Powder X-Ray-Diffraction.* Ferroelectrics, 1991. **115**(1-3), 91-96.

33. Reynaud, M., P. Barpanda, G. Rousse, J.N. Chotard, B.C. Melot, N. Recham, and J.M. Tarascon, *Synthesis and Crystal Chemistry of the $NaMSO_4F$ family (M = Mg, Fe, Co, Cu, Zn).* Solid State Sciences, 2012. **14**(1), 15-20.

34. Mattheiss, L.F., *Electronic-Properties of $Ca_2CuO_2Cl_2$ and $Ca_2CuO_2Br_2$.* Physical Review B, 1990. **42**(1), 354-358.

35. Novikov, D.L., A.J. Freeman, and J.D. Jorgensen, *Electronic-Structure of Superconductors without Apical Oxygen - $Sr_2CuO_2F_2$, $Sr_2CuO_2Cl_2$, and Ca_2CuO_2Cl2.* Physical Review B, 1995. **51**(10), 6675-6679.

36. Wei, S.H. and A. Zunger, *Role of Metal D-States in Ii-Vi Semiconductors.* Physical Review B, 1988. **37**(15), 8958-8981.

37. Jaffe, J.E., R. Pandey, and A.B. Kunz, *Electronic-Structure of the Rock-Salt-Structure Semiconductors ZnO and CdO.* Physical Review B, 1991. **43**(17), 14030-14034.

38. Schleife, A., F. Fuchs, J. Furthmuller, and F. Bechstedt, *First-principles Study of Ground- and Excited-state Properties of MgO, ZnO, and CdO Polymorphs.* Physical Review B, 2006. **73**(24).

39. Segura, A., J.A. Sans, F.J. Manjon, A. Munoz, and M.J. Herrera-Cabrera, *Optical Properties and Electronic Structure of Rock-salt ZnO under Pressure.* Applied Physics Letters, 2003. **83**(2), 278-280.

40. Recio, J.M., M.A. Blanco, V. Luana, R. Pandey, L. Gerward, and J.S. Olsen, *Compressibility of the High-Pressure Rocksalt Phase of ZnO.* Physical Review B, 1998. **58**(14), 8949-8954.

Chapter 5 Crystal structure and magnetic properties of layered oxychloride $Sr_2MnO_2Cl_2$: a possible ideal two-dimensional antiferromagnet

5.1 Introduction

According to Mermin–Wagner theorem[1], there is no long-range order in one- or two dimensional isotropic antiferromagnetic systems at finite temperatures. Most of real compounds, however, give rise to a long-range magnetic order at low temperature because of non-negligible interchain/interlayer interactions, dipole–dipole interactions, single-ion anisotropy, and exchange interaction anisotropy[2]. For RP-type layered perovskite compounds, K_2NiF_4 and K_2MnF_4 with nearly isotropic AFM interactions were investigated as the best candidates of 2D AFM systems, but they undergo an antiferromagnetic ordering (3D ordering) at 97 K and 38 K, respectively due to the mechanism described above[3-8].

Recently, mixed anion systems such as oxyhalides have been extensively studied, especially since the discovery of superconductivity in Na-doped $Ca_2CuO_2Cl_2$. Accommodation of more than one anion with different bonding natures in one structure can allow us to design new anion lattices and unusual coordination environments around the metal center. In the case of $Sr_2CuO_2Cl_2$, chlorine substitution for oxide ions at the apical sites changes the coordination from octahedron to square plane. As a result, the two dimensionality of CuO_2 magnetic layers is enhanced. Based on inelastic neutron scattering experiment, $Sr_2CuO_2Cl_2$ can be described best as an ideal 2D square-lattice Heisenberg AFM system[9]. However, the copper oxychloride also exhibit a long-range magnetic ordering at $T_N = 250$ K.[9-11] The ordered copper spin moment was determined to be 0.34(4) μ_B at 10 K from the neutron study[12-14]. Isostructural $Sr_2CoO_2Cl_2$ was also reported to be synthesized by C. S. Knee and M. T. Weller in 2002. The neutron diffraction study on this cobalt oxychloride revealed an antiferromagnetic ordering at 215 K with complex magnetic structures. The ordered spin moment of Co^{2+} was determined to be 3.22 μ_B at 20 K, suggesting the presence of a significant orbital contribution in Co ions.

Recently, Tsujimoto *et al.* successfully extended the oxychloride family to $Sr_2NiO_2Cl_2$, $Sr_2MnO_2Cl_2$, and $Ba_2PdO_2Cl_2$ by high-pressure technique[15]. In particular, the discovery of the nickel and manganese oxychlorides is of importance because Jahn-Teller inactive Ni^{2+} and Mn^{2+} with a high spin state, which do not prefer a square planar geometry, could be stabilized by chlorine substitution. In the previous work, $Sr_2NiO_2Cl_2$ was found to undergo a long-range magnetic ordering at T_N =210 K while the Mn counterpart did not show an anomaly associated with a magnetic phase transition but a spin-glass behavior below 16 K (**Figure 5.4**). Tsujimoto *et al.* claimed that the spin-glass behavior may not be derived from the intrinsic magnetic state in the following reason. Firstly, the Curie constant was estimated to be 3.24 (emu K)/mol which is smaller/larger than that expected from the high spin (S = 5/2) /intermediate spin state (S = 3/2). Secondly, the Weiss temperature was 1.5 K, suggesting that the magnetic interactions between Mn ions are unusually small. Thirdly, the magnetic susceptibility curve did not show a broad maximum typical of low-dimensional Heisenberg antiferromagnets. Finally, the SXRD patterns detected minor impurity phases including uncharacterized peaks, which possibly mask the intrinsic susceptibility. Therefore, reexamination of the magnetic properties of $Sr_2MnO_2Cl_2$ should be made with a high-quality sample.

5.2 Experimental details

In the previous report, $Sr_2MnO_2Cl_2$ was synthesized from a stoichiometric amount of SrO_2, Mn, and $SrCl_2$ at 1500 °C and 6 GPa. In my study, MnO was used as the manganese source: SrO (in-house synthesized), MnO (99.9%), and $SrCl_2$ (99.9%) in a stoichiometric ratio were reacted under high temperature, high pressure conditions. The mixture enclosed in a Pt capsule was heated for 2 h in a belt-type high-pressure apparatus at 6 GPa and 1600 °C. After the treatment, the sample was quickly quenched to room temperature, and then the pressure was slowly released. The sample colour was black.

5.3 Results and Discussion

5.3.1 Crystal Structure

Figure 5.1 shows the neutron powder diffraction pattern for $Sr_2MnO_2Cl_2$ at 150 K, which could be readily indexed to a simple body-centered tetragonal cell. No site deficiencies were observed for each element. Compared with the previous reported sample which contained a lot of impurity phases, the sample quality got much improved. Only a small amount (2.42%) of tiny additional peaks could be assigned as MnO impurity phases. The lattice parameters of the product are a = 4.09239(6) Å, c = 14.9380(2) Å. Based on a model of $Sr_2CuO_2Cl_2$ (space group *I*4/*mmm*), structural refinements converged very well. The refined crystallographic data including the atomic coordinates and isotropic atomic displacement parameters are presented in **Table 5.1**.

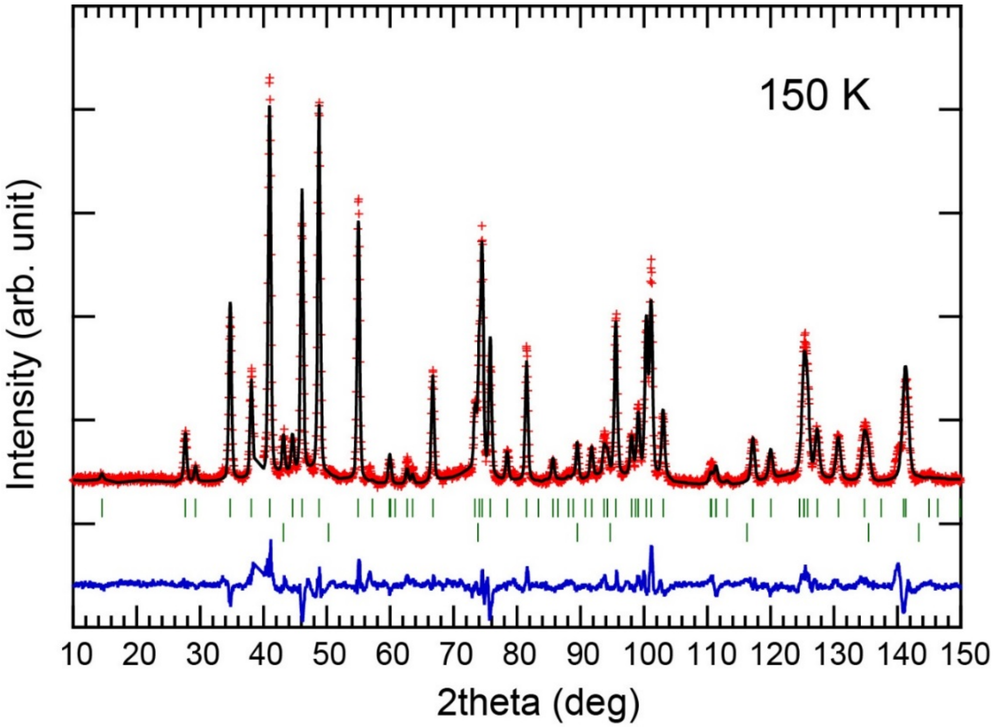

Figure 5.1 NPD patterns for $Sr_2MnO_2Cl_2$ measured at 150 K. Obtained, calculated and difference are presented with cross marks, upper and bottom solid lines, respectively. The vertical lines mark represent the Bragg peak positions.

Table 5.1 Crystallographic Parameters Refined from NPD Data Collected from $Sr_2MnO_2Cl_2$ at 150 K.

Atom	Site	*x*	*y*	*z*	U_{so}(Å^2)
Sr	4*e*	0	0	0.38883(19)	0.0319(7)
Mn	2*a*	0	0	0	0.0270(17)
O	4*c*	0	0.5	0	0.0112(7)
Cl	4*e*	0	0	0.18219(11)	0.0172(5)

The space group is *I*4/*mmm* (no. 139), a = 4.09239(6) Å, c = 14.9380(2) Å. *R* indices are R_B = 10.4%, and R_F = 6.83%.

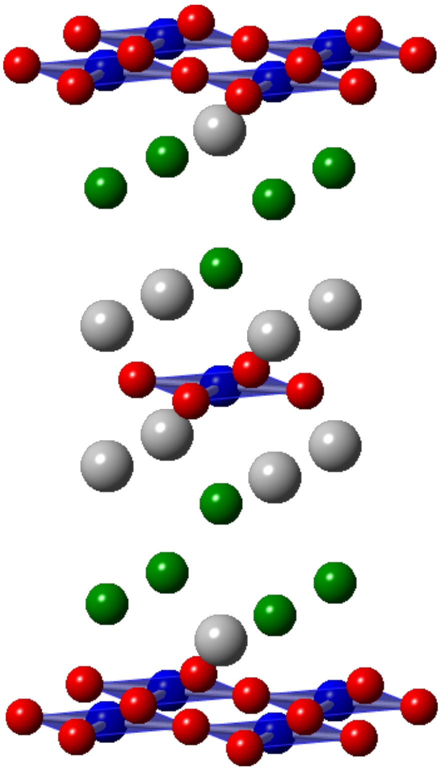

Figure 5.2 Crystal structures of $Sr_2MnO_2Cl_2$. Gray, blue, red, and green spheres represent Sr, Mn, O, and Cl atoms, respectively.

Common to the previous sample reported by Tsujimoto *et al.*[15], the Mn center is surrounded by four oxide ions at the equatorial sites and two chloride ions at the apical sites, as shown in **Figure 5.2**. However, the 1st coordination sphere could be regarded as a square planar coordination. The in-plane Mn–O bond length (2.05 Å) agrees well with the sum of the ionic radii of O^{2-} (r = 1.4 Å) and Mn^{2+} in four-fold coordination (r = 0.66 Å)[16], rather than in six-fold coordination (r = 0.83 Å). The Mn–Cl bonds (2.7216 Å) along the c axis are much longer than those expected from the sum of Mn^{2+} and Cl^- (r = 0.181 Å) in the simple ionic model. The Mn–Cl/Mn–O bond ratio is 1.33, comparable to the corresponding value of 1.35 for $Sr_2CoO_2Cl_2$[17], but smaller than 1.44 for $Sr_2CuO_2Cl_2$ with a strong J–T active Cu^{2+} center[18]. Bond valence sums (BVS) for manganese site is calculated to be 2.25, which is consistent with the nominal oxidation state of Mn(II). Contribution of the Mn–Cl bonds to the total BVS is only 18%. Therefore, we can conclude that the manganese coordination is effectively square planar.

5.3.2 Physical Properties

Temperature dependence of χ for $Sr_2MnO_2Cl_2$ is shown in **Figure 5.3(a)**. A broad maximum occurs at around 42 K, which is a typical behavior in the low dimensional antiferromagnets, in contrast with the paramagnetic behavior of the previous sample. **Figure 5.3(b)** shows the Curie-Weiss fitting which is conducted to the high temperature region (200K-400K). It was estimated that the Curie constants 4.187(9) (emu K)/mol which is consistent with the high spin state of Mn^{2+}, and the Weiss temperature (θ) is –34.9(6) K, indicating that antiferromagnetic interaction is dominant. The field dependence of the magnetization is linear at 100K which could be expected for paramagnetism, as shown in **Figure 5.5(a)**. At 10K, At 10K, a very small hysteresis loop was observed, which may be attributable to impurity phases. The field dependence of susceptibility is shown in **Figure 5.6**. The round curve becomes flat with applied magnetic field, which indicate the absence of field-induced phase transition in this compound.

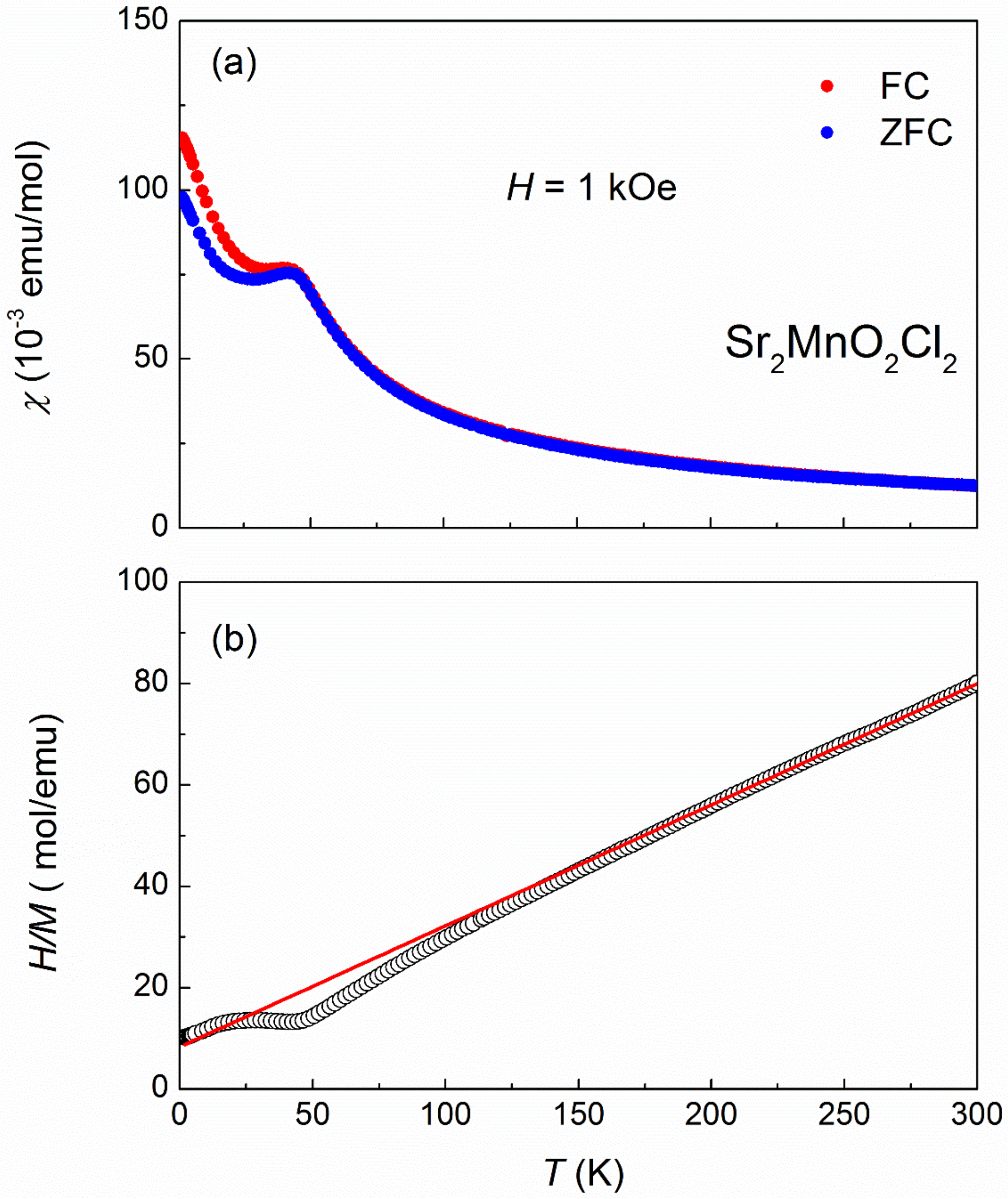

Figure 5.3 (a) Temperature dependence of magnetic susceptibility χ **(b)** Curie-Weiss fitting for the inverse of susceptibility of $Sr_2MnO_2Cl_2$.

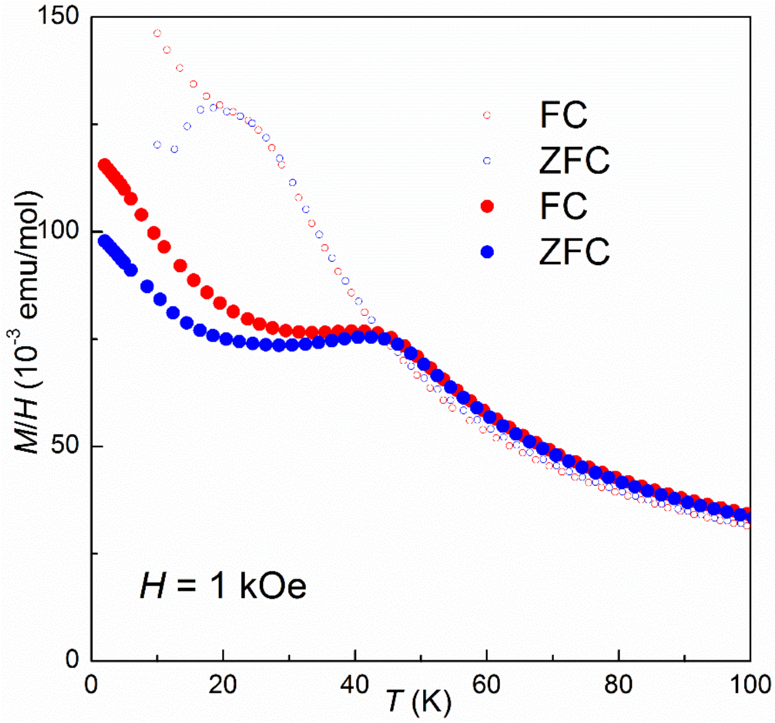

Figure 5.4 Temperature dependence of magnetic susceptibility χ of $Sr_2MnO_2Cl_2$, hollow and solid ball represent sample from previous and this study, respectively.

It is interesting to compare $Sr_2MnO_2Cl_2$ with isostructural $Sr_2NiO_2Cl_2$, whose T_N = 210K, T_{max} ~400K. The large values indicate very strong superexchange interactions between the nearest neighbor nickel ions. It may be due to the shorter Ni-O in-plane distance exhibited by $Sr_2NiO_2Cl_2$ that leads to the increase of the orbital overlap between nickel and ligands. In $Sr_2MnO_2Cl_2$, the relatively small T_{max} suggests the much smaller magnetic interactions between Mn ions, but no sign of a magnetic phase transition appears down to 2 K.

It should be noted that divergence of the ZFC and FC curves in the susceptibility χ data is discernible below T_{max}. Such a divergence is commonly observed in spin glass materials. To investigate if the magnetic ground state of $Sr_2MnO_2Cl_2$ is spin glass, the frequency dependence of the ac susceptibility was measured in the range of 1-100Hz. The real part of the magnetic susceptibility shown in **Figure 5.7** is consistent with the dc magnetic susceptibility and does not show any dispersion over the frequency range. This behavior is different from that expected from spin glass states, indicating that the magnetic ground sate of the manganese oxychloride is not a simple spin glass material. However, the imaginary part of the susceptibility χ’’ exhibits a clear peak at 30 K, although χ’’ is frequency independent, too. Therefore, the possibility of spin glass is excluded, but some magnetic state likely exists at low temperatures.

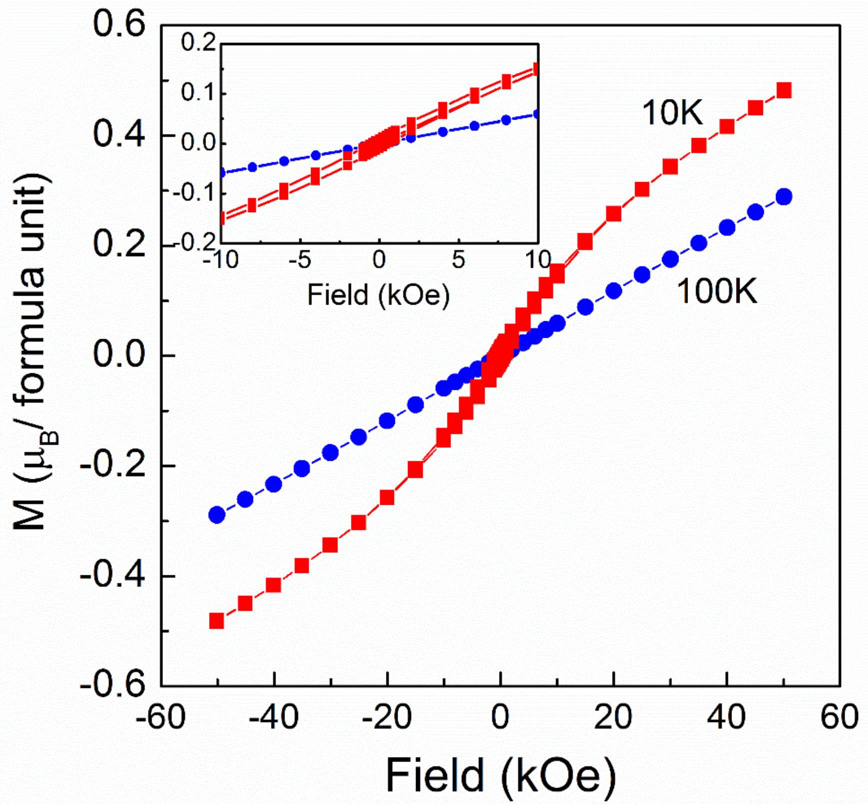

Figure 5.5 The field dependence of the magnetization, inset is the magnified susceptibility of the magnetization in the range of *H* -1T to 1T.

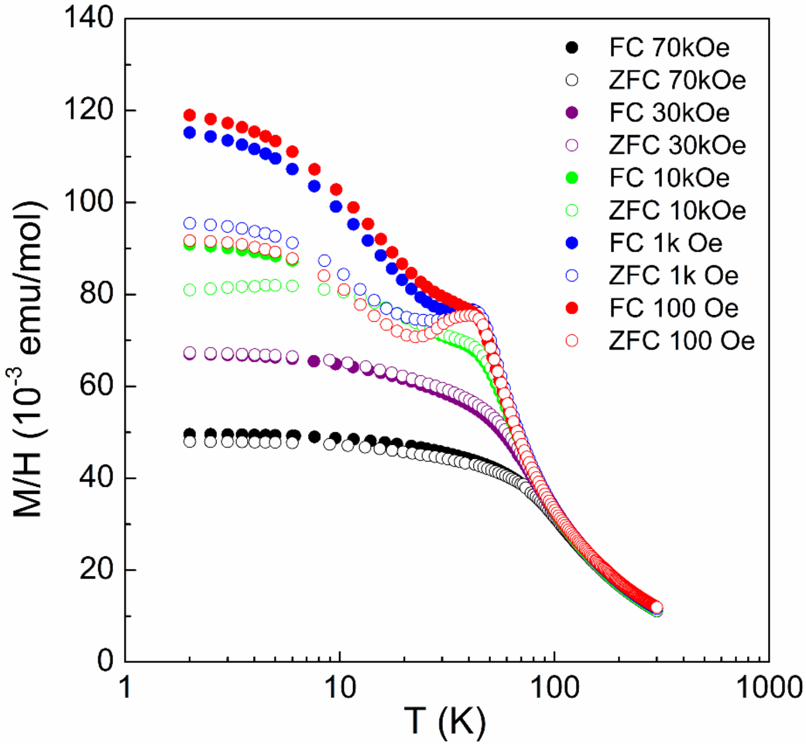

Figure 5.6 The magnetic susceptibility at different magnetic field.

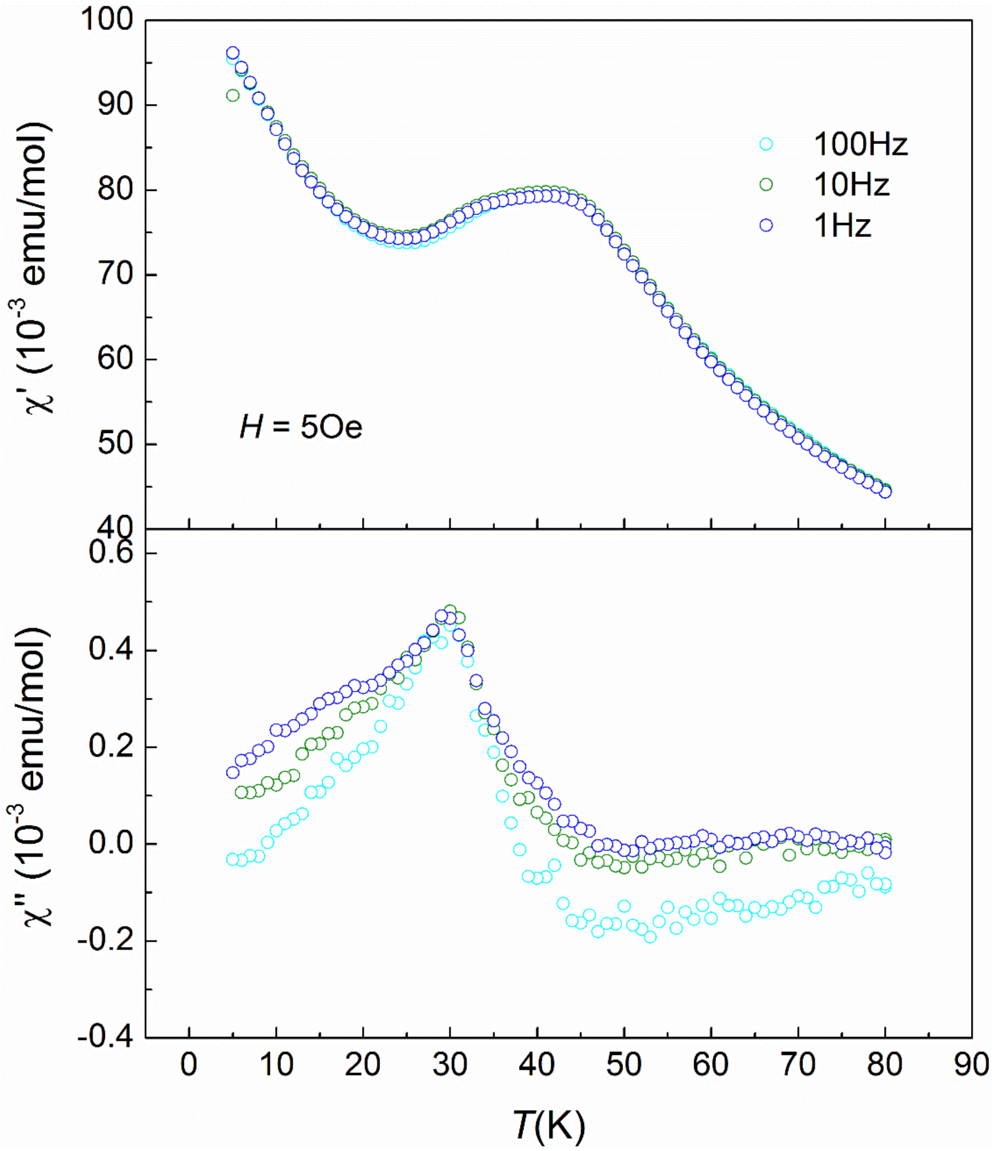

Figure 5.7 Upper frame shows the temperature dependence of the real part of the ac magnetic susceptibility at different frequencies from 1 Hz to 100 Hz . Lower frame shows the imaginary part of the ac magnetic susceptibility at the same frequencies as real part.

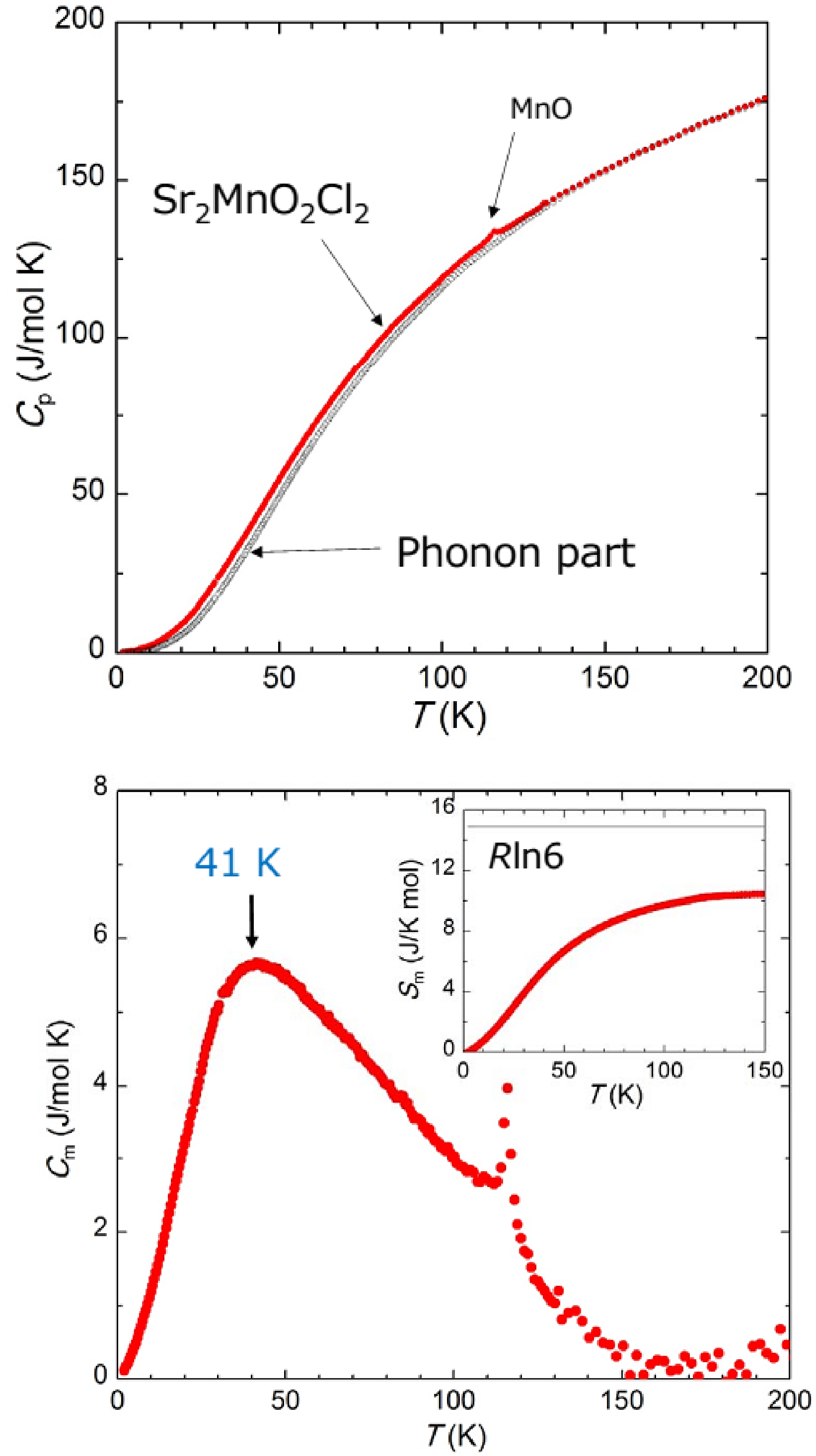

Figure 5.8(a) Temperature dependence of the specific heat and **(b)** magnetic specific heat versus temperature, the inset shows the temperature dependence of the magnetic entropy for $Sr_2MnO_2Cl_2$.

To further characterize the anomaly observed below 40 K, the heat capacity C_p was measured as shown in **Figure 5.8**. The C_p vs T plot exhibited a Schottky anomaly centered at 40 K, corresponding to T_{max} in the magnetic susceptibility. No magnetic phase transition was detected down to 2K. A small peak at about 115 K was due to the antiferromagnetic ordering of MnO impurity[19]. To estimate the magnetic entropy (ΔS), the lattice contribution (C_{phonon}) was roughly subtracted from C_p using the data of isostructural compound $Sr_2ZnO_2Cl_2$ prepared in Chapter 4. By the subtraction and integration of $(C_p–C_{phonon})/T$, ΔS was estimated to be approximately 10.53 J/mole-K. Rise of ΔS with temperature increasing is associated with a transition from ordered state to a disordered state. The associated entropy change is expected to be $R\ln(2S+1) = 14.897$ J/mole-K, where R is the universal gas constant 8.314 J/mole-K and S is the spin of the magnetic ions. The ΔS is somewhat smaller than the expected value, which is consistent with the absence of a long-range magnetic order. It is noteworthy that the short-range magnetic correlations start to develop at 150 K, which is also consistent with the result of the magnetic susceptibility measurements.

5.3.3 Neutron Study

Figure 5.9 depicts the temperature dependence of the NPD patterns below 150 K. From the expanded figure, it is found that a sharp peak at about 21.5° appears below 125K, which can be attributed to the onset of long range antiferromagnetic order of MnO impurity[20] On further cooling, only a broad peak at 19° appears a 100 K and the intensity gradually increases with lowering temperature. This peak could be assigned to $(100)_{mag}$ on the basis of the super cell of $\sqrt{2}a \times\sqrt{2}a$, indicating that the nearest neighbor spin are aligned antiparallel. However, close inspection of the peak revealed diffuse scattering even at 2 K: the peak shape is asymmetric and extending to higher angles. This type of the peak shape, which is termed Warren type peak shape[21], occurs when the 2D spin-spin correlation is developing within only the magnetic layers. Thus, this observation gives evidence for the realization of no long-range magnetic order. As seen in **Figure 5.10**, similar magnetic Bragg peak associated with $(100)_{\mathrm{mag}}$ was observed in K_2NiF_4, $Sr_2CuO_2Cl_2$, and related layered compounds above T_N, but the diffuse scattering disappeared at T_N, followed by the appearance of additional sharp magnetic Bragg peaks such as $(011)_{\mathrm{mag}}$ and $(102)_{\mathrm{mag}}$, corresponding to a long-range magnetic order including the spin arrangement between interlayers[4, 22]. The correlation length ξ at 2 K calculated for $Sr_2MnO_2Cl_2$ using the Warren function was approximately 88 Å, corresponding to 22 chemical unit cells (**Figure 5.11**). The ξ value is even smaller than that for $Sr_2CuO_2Cl_2$ just above T_N (ξ ~ 200 Å)[23]. The difference of ξ can be taken into account by considering the stronger quantum fluctuations in Cu^{2+} ion with $S = 1/2$.

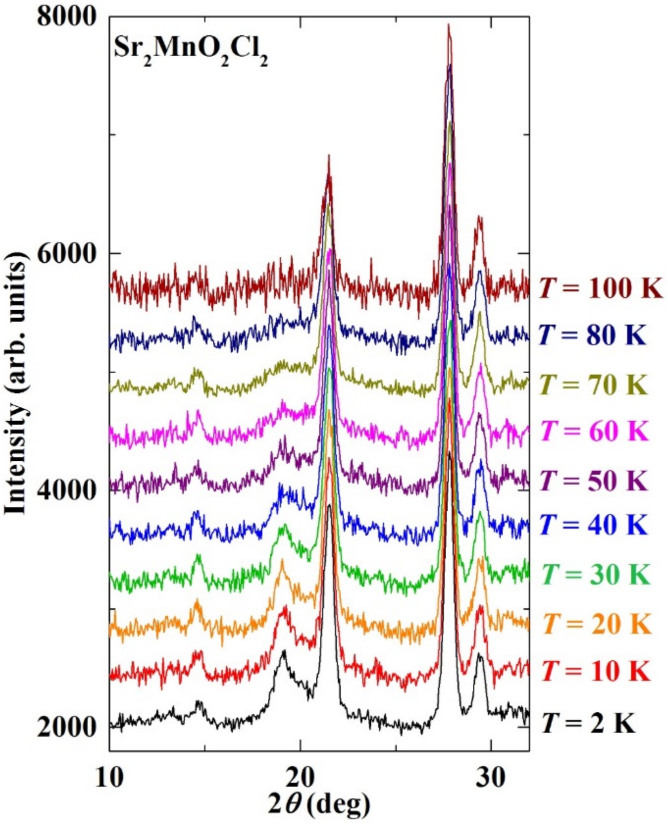

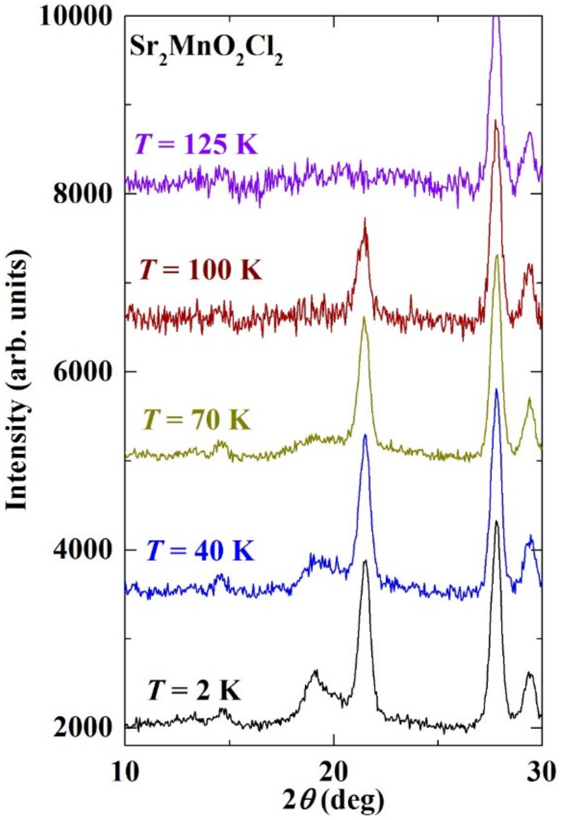

Figure 5.9 NPD patterns and expanded figure of range 10°- 30°. At 70 K, magnetic diffuse scattering at 19°, corresponding to (100)m reflection.

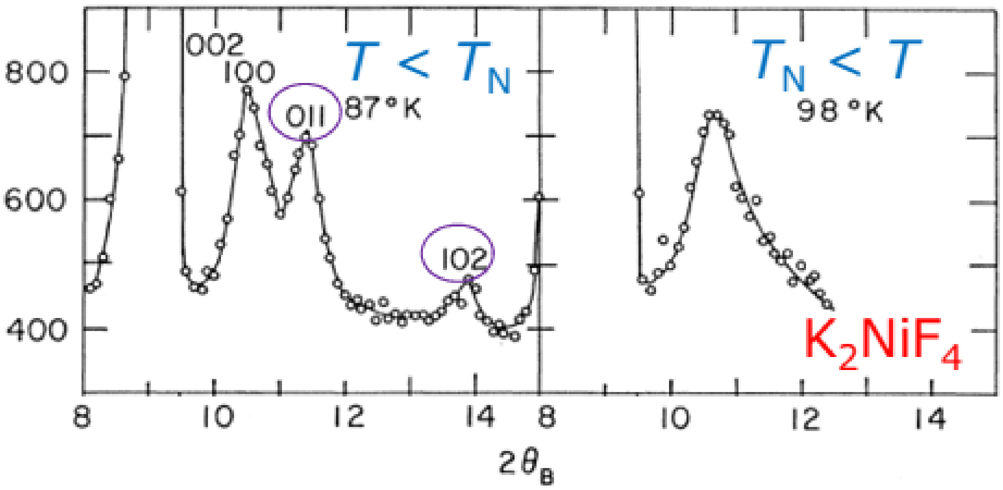

Figure 5.10 Temperature evolution of K2NiF4 powder neutron diffraction pattern.

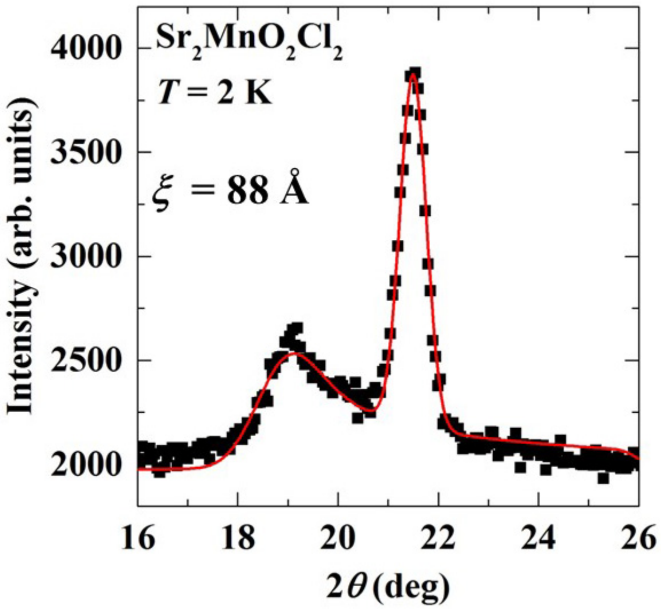

Figure 5.11 Fit of diffuse scattering of $Sr_2MnO_2Cl_2$ to the Warren function. The sharp peak at 21.5° is a magnetic Bragg peak from MnO.

5.3 Summary of chapter 5

In this chapter, high-quality $Sr_2MnO_2Cl_2$ was successfully synthesized by high pressure method. The sample quality was improved compared with the previous study, which allowed us to investigate the intrinsic magnetic properties. It was found that $Sr_2MnO_2Cl_2$ has a high-spin state of Mn^{2+} with $S = 5/2$. The magnetic susceptibility and heat capacity measurements exhibited a short-range magnetic order below 150 K. Furthermore, the neutron diffraction study revealed a Warren-type magnetic peak at 19° corresponding to $(100)_{mag}$ on the basis of $\sqrt{2}a \times \sqrt{2}a$. Surprisingly, the short-range magnetic ordered state did not develop to the 3D magnetic ordered state down to 2 K. This is the first square-lattice antiferromagnet without a long-range magnetic order. At present, the mechanism of the absence of a long-range magnetic order is unclear. Understanding the spin dynamics of the compound will shed light on the mechanism.

References in chapter 5

1. Mermin, N.D. and H. Wagner, *Absence of Ferromagnetism or Antiferromagnetism in One- or 2-Dimensional Isotropic Heisenberg Models.* Physical Review Letters, 1966. **17**(22), 1133-&.

2. Pich, C. and F. Schwabl, *Order of two-dimensional isotropic dipolar antiferromagnets.* Physical Review B, 1993. **47**, 7957.

3. Hu, A.Y. and Q. Wang, *The magnetic order of two-dimensional anisotropic antiferromagnets.* Solid State Communications, 2011. **151**(2), 102-106.

4. Birgeneau, R.J., H.J. Guggenheim, and G. Shirane, *Neutron Scattering Investigation of Phase Transitions and Magnetic Correlations in 2-Dimensional Antiferromagnets* K_2NiF_4*,* Rb_2MnF_4*,* Rb_2FeF_4*.* Physical Review B-Solid State, 1970. **1**(5), 2211-+.

5. Breed, D.J., *Antiferromagnetism of K2mnf4.* Physics Letters, 1966. **23**(3), 181-&.

6. Ikeda, H. and K. Hirakawa, *Critical Magnetic Scattering in* K_2MnF_4*.* Journal of the Physical Society of Japan, 1973. **35**(2), 617-617.

7. Lines, M.E., *Comparative studies of magnetism in* $KNiIF_3$ *and* K_2NiF_4*.* Physical Review, 1967. **164**(2), 736-&.

8. Srivastava, J.P. and V. Gerhardt, *Intrinsic emission in quadratic-layer antiferromagnets -* K_2MnF_4 *and* Rb_2MnCl_4*.* Journal of Physics C-Solid State Physics, 1977. **10**(1), L13-L15.

9. Greven, M., R.J. Birgeneau, Y. Endoh, M.A. Kastner, B. Keimer, M. Matsuda, G. Shirane, and T.R. Thurston, *Spin Correlations in* $Sr_2CuO_2Cl_2$*.* Physica B, 1994. **199**, 642-643.

10. Greven, M., R.J. Birgeneau, Y. Endoh, M.A. Kastner, B. Keimer, M. Matsuda, G. Shirane, and T.R. Thurston, *Spin Correlations in the 2d Heisenberg-Antiferromagnet* $Sr_2CuO_2Cl_2$ *- Neutron-Scattering, Monte-Carlo Simulation, and Theory.* Physical Review Letters, 1994. **72**(7), 1096-1099.

11. Wang, X.L., L.L. Miller, J. Ye, C. Stassis, B.N. Harmon, D.C. Johnston, A.J. Schultz, and C.K. Loong, *Antiferromagnetic Form-Factor of* $Sr_2CuO_2Cl_2$. Journal of Applied Physics, 1990. **67**(9), 4524-4526.

12. Kohsaka, Y., C. Taylor, K. Fujita, A. Schmidt, C. Lupien, T. Hanaguri, M. Azuma, M. Takano, H. Eisaki, H. Takagi, S. Uchida, and J.C. Davis, *An intrinsic bond-centered electronic glass with unidirectional domains in underdoped cuprates.* Science, 2007. **315**(5817), 1380-1385.

13. Vaknin, D., S.K. Sinha, C. Stassis, L.L. Miller, and D.C. Johnston, *Antiferromagnetism in* $Sr_2CuO_2Cl_2$. Physical Review B, 1990. **41**(4), 1926-1933.

14. Kohsaka, Y., T. Hanaguri, M. Azuma, M. Takano, J.C. Davis, and H. Takagi, *Visualization of the emergence of the pseudogap state and the evolution to superconductivity in a lightly hole-doped Mott insulator.* Nature Physics, 2012. **8**(7), 534-538.

15. Tsujimoto, Y., C.I. Sathish, Y. Matsushita, K. Yamaura, and T. Uchikoshi, *New members of layered oxychloride perovskites with square planar coordination:* $Sr_2MO_2Cl_2$ *(M = Mn, Ni) and* $Ba_2PdO_2Cl_2$. Chemical Communications, 2014. **50**(44), 5915-5918.

16. Shannon, R.D., *Revised Effective Ionic-Radii and Systematic Studies of Interatomic Distances in Halides and Chalcogenides.* Acta Crystallographica Section A, 1976. **32**(Sep1), 751-767.

17. Gui, H., X. Li, W.X. Lv, Z.J. Zhao, and W.H. Xie, *Structural and Electronic Properties of* $Sr_2CoO_2Cl_2$. Journal of Electronic Materials, 2016. **45**(10), 4843-4846.

18. Miller, L.L., X.L. Wang, S.X. Wang, C. Stassis, D.C. Johnston, J. Faber, and C.K. Loong, *Synthesis, Structure, and Properties of* $Sr_2CuO_2Cl_2$. Physical Review B, 1990. **41**(4), 1921-1925.

19. Wang, C.H., S.N. Baker, M.D. Lumsden, S.E. Nagler, W.T. Heller, G.A. Baker, P.D. Deen, L.M.D. Cranswick, Y. Su, and A.D. Christianson, *Antiferromagnetic order in MnO spherical nanoparticles.* Physical Review B, 2011. **83**(21).

20. Goodwin, A.L., M.G. Tucker, M.T. Dove, and D.A. Keen, *Magnetic structure of MnO at 10 k from total neutron scattering data.* Physical Review Letters, 2006. **96**(4).

21. Warren, B.E., *X-Ray Diffraction in Random Layer Lattices.* Physical Review, 1941. **59**(9), 693-698.

22. Birgeneau, R.J., H.J. Guggenheim, and G. Shirane, *Neutron Scattering from* K_2NiF_4 *- a 2-Dimensional Heisenberg Antiferromagnet.* Physical Review Letters, 1969. **22**(14), 720-+.

23. Greven, M., R.J. Birgeneau, Y. Endoh, M.A. Kastner, M. Matsuda, and G. Shirane, *Neutron scattering study of the two-dimensional spin S=1/2 square-lattice Heisenberg antiferromagnet* $Sr_2CuO_2Cl_2$*.* Zeitschrift für Physik B Condensed Matter, 1995. **96**(4), 465-477.

Chapter 6 General Conclusions and Future Prospects

6.1 General Conclusions

The topic of this dissertation is the manipulation of layered perovskites by anion substitution. Much effort has been made to control the synthesis of new compounds by high pressure techniques. Anion substitution can effectively affect the coordination geometry or environment around the metal centers, which are closely correlated with the electronic structures of the compounds. Anion lattice modification also provides good advantage of understanding the role played by each anion in the structural, physical and chemical properties as a result of accessibility to anion-site ordered states. The structural variety obtained within RP type structure compounds through anion lattice manipulation makes these compounds so important. In turn, the additional promise of new intriguing properties, is also an important consideration.

Perovskite-based manganese oxides expressed as $A\mathrm{MnO_3}$ (A = alkaline earth or lanthanide metals) have been extensively studied because of their interesting physical properties. In comparison with a great deal of studies on cation substitution, the effects of anion substitution on physical properties of manganese perovskite compounds have been investigated to a lesser extent. High-pressure method was proved to be a very useful approach toward mixed anion compounds. Another member of layered oxyfluoride family $\mathrm{Sr_2MnO_3F}$ with a $n = 1$ Ruddlesden –Popper type structure, was successfully synthesized by the high-pressure method at 6 GPa and 1800 °C. Structural refinements against synchrotron X-ray diffraction data collected from manganese oxyfluoride demonstrated that it crystallizes in a tetragonal cell with the space group I4/mmm, in which the Mn cation is located at the octahedral center position. This is in stark contrast to the related oxyhalides that have square pyramidal coordination such as $\mathrm{Sr_2}M\mathrm{O_3}X$ (M = Fe, Co, Ni; X = F, Cl) and $\mathrm{Sr_2MnO_3Cl}$. There was no evidence of O/F site order, but close inspection of the anion environment centered at the Mn cation on the basis of bond-valence-sum calculation suggested preferential occupation of the apical sites by the F ion with one oxide ion in a random manner. Magnetic susceptibility and heat capacity measurements revealed an antiferromagnetic ordering at 133 K ($=T_N$), which is much higher than that of the chloride analogue with corrugated MnO_2 planes (T_N = 80 K).

In condensed matter science, there has been great interest in the study of square planar coordination since high-T_C superconductivity and ideal two-dimensional magnetism arise from CuO_4 square units. The square planar coordination, however, is generally limited to Jahn-Teller active ions (e.g. Cu^{2+} and Ti^{3+}) and 4d/5d metals with a large crystal field energy (e.g. Pd^{2+} and Pt^{2+})[1-6]. From the viewpoint of local coordination, the Zn^{2+} center exclusively takes a tetrahedral or octahedral coordination and it is rather rare to have a square planar coordination. In this study, a new layered perovskite zinc oxychloride, $Sr_2ZnO_2Cl_2$, with an infinite ZnO_2 square planar sheet has been successfully synthesized by high pressure method. The oxychloride possesses an indirect band gap of E_g = 3.66 eV, corresponding to a transition between O 2*p* and Zn 4*s* energy bands. These results result from the electronic nature of the square planar geometry for zinc, which is distinct from tetrahedrally coordinated ZnO.

Two dimensional antiferromagnets, such as K_2NiF_4, K_2MnF_4, Rb_2MnF_4 and Rb_2MnCl_4, have attracted great attention both in experimental and theoretical studies[7-11]. According to Mermin–Wagner theorem[12], there is no long-range order in one- or two dimensional isotropic antiferromagnetic systems at finite temperatures. Most of real compounds, however, give rise to a long-range magnetic order at low temperature because of certain reasons. $Sr_2MnO_2Cl_2$, analogy with $Sr_2CuO_2Cl_2$ and $Sr_2NiO_2Cl_2$, was expected to show two dimensionality, but previous study haven't access to a good sample[13]. Herein, we synthesized $Sr_2MnO_2Cl_2$ sample with high pressure method which showed a broad maximum of the 2D antiferromagnetic interaction. The sample quality was improved. It takes a high-spin state with S = 5/2. Neutron studies showed that short range order develops at 80K, no long-range magnetic order down to

2 K, which is different with the K_2NiF_4 series. $Sr_2MnO_2Cl_2$ may be viewed as an ideal 2D antiferromagnet.

6.2 Future Prospects

There are still some work to do to supplement my thesis, for example, for $Sr_2ZnO_2Cl_2$ compound, since it is a semiconductor, doping could be carried out to study the influence to the conductivity. And for $Sr_2MnO_2Cl_2$ compound, other measurements should be conducted to investigate the magnetic ground state. In addition, for related oxychlorides, doping induced some novel properties, thus we can imagine that doped $Sr_2MnO_2Cl_2$ may also show some interesting properties. These works are remained to be completed. My ongoing studies will be focused on synthesizing new mixed anion compounds with RP type structure and searching for new exotic physical properties.

Substitution of anions with different bonding nature, valence state or ionic radius from oxygen in a metal oxide can enhance the original physical properties or induce new exotic phenomena. The structure and properties of Sr_2BO_3F and $A_2BO_2X_2$ families have already been studied. Some interesting phenomenon were reported due to the anion substitution. Further work about the cationic substitution to these series will be conducted to explore interesting phenomenon. In addition, I will try to synthesize other new oxyhalides with different physical properties or with different methods. These oxyhalides, besides the intriguing properties, some are promising candidates for spintronics, memory devices and sensors, etc. In a word, this area still remains mysterious and provides a lot of possibilities.

References in chapter 6

1. Tsujimoto, Y., S. Nakano, N. Ishimatsu, M. Mizumaki, N. Kawamura, T. Kawakami, Y. Matsushita, and K. Yamaura, *Pressure-Driven Spin Crossover Involving Polyhedral*

Transformation in Layered Perovskite Cobalt Oxyfluoride. Scientific Reports, 2016. **6**.

2. Tsujimoto, Y., C.I. Sathish, Y. Matsushita, K. Yamaura, and T. Uchikoshi, *New Members of Layered Oxychloride Perovskites with Square Planar Coordination:* $Sr_2MO_2Cl_2$ *(M = Mn, Ni) and* $Ba_2PdO_2Cl_2$*.* Chemical Communications, 2014. **50**(44), 5915-5918.

3. Fujito, H., H. Kunioku, D. Kato, H. Suzuki, M. Higashi, H. Kageyama, and R. Abe, *Layered Perovskite Oxychloride* Bi_4NbO_8Cl*: A Stable Visible Light Responsive Photocatalyst for Water Splitting.* Journal of the American Chemical Society, 2016. **138**(7), 2082-2085.

4. Batuk, M., D. Batuk, A.A. Tsirlin, D.S. Filimonov, D.V. Sheptyakov, M. Frontzek, J. Hadermann, and A.M. Abakumov, *Layered Oxychlorides [PbBiO2]A(n+1)B(n)O(3n-1)Cl(2) (A = Pb/Bi, B = Fe/Ti): Intergrowth of the Hematophanite and Sillen Phases.* Chemistry of Materials, 2015. **27**(8), 2946-2956.

5. Clemens, O., R. Kruk, E.A. Patterson, C. Loho, C. Reitz, A.J. Wright, K.S. Knight, H. Hahn, and P.R. Slater, *Introducing a Large Polar Tetragonal Distortion into Ba-Doped* $BiFeO_3$ *by Low-Temperature Fluorination.* Inorganic Chemistry, 2014. **53**(23), 12572-12583.

6. Kodenkandath, T.A., J.N. Lalena, W.L.L. Zhou, E.E. Carpenter, C. Sangregorio, A.U. Falster, W.B. Simmons, C.J. O'Connor, and J.B. Wiley, *Assembly of Metal-Anion Arrays Within a Perovskite Host. Low-temperature Synthesis of New Layered Copper-Oxyhalides,* $(CuX)LaNb_2O_7$*, X = Cl, Br.* Journal of the American Chemical Society, 1999. **121**(46), 10743-10746.

7. Hu, A.Y. and Q. Wang, *The magnetic order of two-dimensional anisotropic antiferromagnets.* Solid State Communications, 2011. **151**(2), 102-106.

8. Breed, D.J., *Antiferromagnetism of K2mnf4.* Physics Letters, 1966. **23**(3), 181-&.

9. Ikeda, H. and K. Hirakawa, *Critical Magnetic Scattering in* K_2MnF_4*.* Journal of the Physical Society of Japan, 1973. **35**(2), 617-617.

10. Lines, M.E., *Comparative studies of magnetism in* $KNiIF_3$ *and* K_2NiF_4*.* Physical Review, 1967. **164**(2), 736-&.

11. Srivastava, J.P. and V. Gerhardt, *Intrinsic emission in quadratic-layer antiferromagnets - K_2MnF_4 and Rb_2MnCl_4.* Journal of Physics C-Solid State Physics, 1977. **10**(1), L13-L15.

12. Mermin, N.D. and H. Wagner, *Absence of Ferromagnetism or Antiferromagnetism in One- or 2-Dimensional Isotropic Heisenberg Models*. Physical Review Letters, 1966. **17**(22), 1133-&.

13. Greven, M., R.J. Birgeneau, Y. Endoh, M.A. Kastner, B. Keimer, M. Matsuda, G. Shirane, and T.R. Thurston, *Spin Correlations in $Sr_2CuO_2Cl_2$.* Physica B, 1994. **199**, 642-643.

List of appended publications

This thesis is based on the following publications.

1. Scientific papers

[1] Y. Su, Y. Tsujimoto, A. Miura, S. Asai, M.Avdeev, H. Ogino, M. Ako, A.A. Belik, T. Masuda, T. Uchikoshi, and K. Yamaura, A layered wide-gap oxyhalide semiconductor with an infinite ZnO_2 square planaer sheet: $Sr_2ZnO_2Cl_2$. Chemical Communications, 2017. 53(27), 3826-3829.

DOI:10.1039/C7CC01011G

[2] Y. Su, Y. Tsujimoto, Y. Matsushita, Y. YUAN, J. He, K. Yamaura : "High-Pressure Synthesis Crystal Structure and Magnetic Properties of Sr_2MnO_3F: A New Member of Layered Perovskite Oxyfluorides" Inorg. Chem. **55**[5] (2016) 2627-2633.

DOI:10.1021/acs.inorgchem.5b02984

2. Presentation

[1] Y. SU, *et al.*, "Synthesis and Crystal Structure of Layered Perovskite Oxychloride with Zinc Square-Planar Coordination: $Sr_2ZnO_2Cl_2$" The 26th annual meeting of MRS-J, Dec. 19-22, 2016, Yokohama, Tokyo.

[2] Y. SU, *et al.*, "High-Pressure Synthesis, Crystal Structure and Magnetic Properties of the New Layered Oxyfluoride Perovskite Sr_2MnO_3F", The Ceramic Society of Japan Annual Meeting 2016, Mar. 14-16, 2016, Tokyo, Japan.

[3] Y.SU, et al., "High-Pressure Synthesis of the New Layered Oxyfluoride Perovskite Sr_2MnO_3F", the 25th annual meeting of MRS-J, Dec. 8-10, 2015, Yokohama, Japan.

[4] Y.SU, et al., "High-Pressure Synthesis of the New Layered Oxyfluoride Perovskite Sr_2MnO_3F", STAC-9, Oct. 19-21, 2015, Tsukuba, Japan.

[5] Y.SU, et al., “High-Pressure Synthesis of the New Layered Oxyfluoride Perovskite Sr_2MnO_3F” The Ceramic Society of Japan Annual Meeting 2015, Sep. 16-18, 2015, Toyama, Japan.

Acknowledgement

I would like to gratefully and sincerely thank my supervisors Prof. Kazunari Yamaura and Prof. Yoshihiro Tsujimoto for their instruction, understanding and patience during my studies, and also for the help they gave me for my dissertation work. I am grateful to have this opportunity to purse for my PhD in this group. During the past three years, Prof. Yamaura not only gave me suggestions for scientific researches but also offered a lot of help about my living in Japan. Prof. Tsujimoto gave me important instructions in the research and taught me how to be an experimentalist but also as an independent thinker. Their enthusiasm in science, diligence, and personality will inspire me in my future journey in science.

I would like to thank Dr Maxim Avdeev, Dr. Vladimir Pomjakushi, Dr. Shinichiro Asai, and Prof. Takatsugu Masuda for help in neutron studies. I sincerely thank Dr. Yoshitaka Matsushita for help in XRD measurement. I would like to say thanks to Dr. Akira Miura for theoretical calculation for $Sr_2ZnO_2Cl_2$. I would like to give my gratitude to Dr. Yahua Yuan, Dr. Shan Yu and Mr. Jianfeng He for that they taught me how to use lab facilities. I would like to extend my gratitude to previous and present members in my research group: Dr. Masashi Miyakawa, Ms. Ryoko Hayakawa, Dr. Alexei Belik, Mr Lei Zhang, and Ms Jie Chen for their help and supports. Finally, I would like to give my gratitude to my parents, my husband and my sister for their love, encouragement and support.